PB-230 086

UTILIZATION OF A HIGH INTENSITY ARC FOR THE CONTROLLED GENERATION OF ULTRA-FINE MONODISPERSE AEROSOLS

C. V. Boffa, et al

Minnesota University

Prepared for:

Environmental Protection Agency

May 1972

DISTRIBUTED BY:

NTIS

National Technical Information Service
U. S. DEPARTMENT OF COMMERCE
5285 Port Royal Road, Springfield Va. 22151

PB 230 086

HTL TR No. 106

UTILIZATION OF A HIGH INTENSITY ARC FOR THE CONTROLLED GENERATION OF ULTRAFINE, MONODISPERSE AEROSOLS

By

C. V. Boffa* and E. Pfender

Final Report
Prepared for the

Environmental Protection Agency
National Environmental Research Center
Research Triangle Park, North Carolina 27711

May, 1972

Heat Transfer Laboratory
Mechanical Engineering Department
University of Minnesota
Minneapolis, Minnesota 55455

---

* Prof. Inc., Istituto di Fisica Tecnica, Politecnico di Torino, Italy

Reproduced by
NATIONAL TECHNICAL
INFORMATION SERVICE
U S Department of Commerce
Springfield VA 22151

TABLE OF CONTENTS

		Page
	ACKNOWLEDGMENTS	i
	LIST OF FIGURES	ii
	NOMENCLATURE	vi
	ABSTRACT	ix
I.	INTRODUCTION	1
II.	AEROSOL GENERATOR: EXPERIMENTAL APPARATUS	4
	A. Plasma Torch	4
	B. Particle Collection Chamber	8
	C. Control Panel	8
	D. Auxiliary Equipment	12
III.	TRANSPIRATION COOLED ANODE IN HIGH INTENSITY ARC: EVALUATION OF GOVERNING PARAMETERS	13
	A. Cold Flow Tests and Preliminary Observations	13
	B. Arc Characteristics	16
	C. Segmented Porous Anode: Transpiring Flow Characteristics During Arc Operation	21
	D. Temperature Distribution in the Porous Anode Sectors	27
	E. Estimate of the Arc Attachment Size	42
IV.	SIZE MEASUREMENTS OF ABLATED CARBON AEROSOL	46
	A. Aerosol Sampling Technique	46
	B. Experimental Procedure and Results	49
	C. Conclusions	59
V.	SUMMARY	72
	APPENDIX: EXPERIMENTAL INVESTIGATION OF GAS FLOW CHARACTERISTICS IN TRANSPIRATION COOLED POROUS MATRICES	76

		Page
A.I.	INTRODUCTION	76
A.II.	INVESTIGATION OF THE UNIFORMITY OF THE GAS FLOW DOWNSTREAM OF THE POROUS SLAB	78
	A. Experimental Procedure and Results	79
	B. Conclusions	92
A.III.	DETERMINATION OF GAS FLOW CHARACTERISTICS IN HIGH TEMPERATURE POROUS CARBON	97
	A. Background	97
	B. Experimental Apparatus	101
	C. Experimental Procedure and Results	104
	D. Conclusions	110
	REFERENCES	119

ACKNOWLEDGMENTS

This work has been supported by the United States Public Health Service Research Grant Numbers AP 01161-01 and -02.

The assistance of the Particle Technology Laboratory of this Department in the form of analyzing equipment is gratefully acknowledged.

LIST OF FIGURES

Figure	Title	Page
1	Schematic of the Plasma Torch	5
2	Schematic of the Particle Collection Chamber	9
3	Argon Flow Control Circuits	11
4	Porous Anode Sectors: Cold Flow Characteristics	14
5	Arc Characteristics	18
6	Arc Characteristics	20
7	Porous Anode Sectors: Flow Characteristics During Arc Operation	22
8	Porous Anode Sectors: Flow Characteristics During Arc Operation	23
9	Pressure Drop Across Porous Anode Sectors Versus Arc Current	25
10	Pressure Drop Across Porous Anode Sectors Versus Arc Current	26
11	Influence of Pressure Drop Variation on the Temperature Distribution Inside Porous Anode Sectors	31
12	Influence of Transpiring Mass Flowrate Variations on the Temperature Distribution Inside Porous Anode Sectors	32
13	Temperature of Porous Sectors Outside Surface as a Function of Transpiring Mass Flowrate Per Unit Area and Pressure Drop Across the Sector	34
14	Temperature of Porous Sectors Inside Surface as a Function of Transpiring Mass Flowrate Per Unit Area and Pressure Drop Across the Sector	35

Figure	Title	Page
15	Comparison of Theoretical and Experimental Temperature Values of Porous Anode Sectors Outside Surface	36
16	Comparison of Theoretical and Experimental Temperature Values of Porous Anode Sectors	38
17	Comparison of Theoretical and Experimental Temperature Values of Porous Anode Sectors	39
18	Comparison of Theoretical and Experimental Temperature Values of Porous Anode Sectors	40
19	Arc Attachment Size Versus Mass Flowrate Per Unit Area	45
20	Schematic of the Electrostatic Particle Counter	47
21	Ablation Tests: Porous Segment Characteristic Parameters	50
22	Ablation Tests: Comparison of Flow Characteristics Through Porous Anode Segment	52
23	Ablation Tests: Comparison of Porous Anode Segment Outside Surface Temperature	53
24	Ablating Surface Temperature Versus Transpiring Mass Flowrate Per Unit Area	55
25	Cumulative Size Distributions of Ablated Particles	56
26	Cumulative Size Distributions of Ablated Particles	57
27	Mean Particle Diameter as a Function of Transpiring Mass Flowrate Per Unit Area	60
28	Mean Particle Diameter as a Function of Ablating Surface Temperature	61
29	Logarithmic Standard Deviation Versus Transpiring Mass Flowrate Per Unit Area	64

Figure	Title	Page
30	Logarithmic Standard Deviation Versus Ablating Surface Temperature	65
31	Logarithmic Standard Deviation Versus Mean Particle Diameter	68
32	Ablated Aerosol Size Distribution	69
33	Ablated Aerosol Size Distribution	70
34	Particle Number Density as a Function of the Inverse of the Ablating Surface Temperature	71
35	Schematic of the Apparatus for Porous Matrices Cold Flow Tests	80
36	Schematic of the Control Circuits	82
37	Coordinate System	84
38	Typical Impact Pressure Recordings in ±y Direction at a Given x and z Value	86
39	Typical Impact Pressure Recordings in y Direction at a Given x Value	87
40	Comparison of Transpiring Gas Mass Flow Rate Values per Unit Area Obtained by Integration of Velocity Profiles and from Flowmeter Readings as a Function of x for a Given z Value	89
41	Comparison of Transpiring Gas Mass Flow Rate Values Obtained by Integration of Velocity Profiles over the Entire Test Section and from Flowmeter Readings as a Function of z Location	90
42	Example of the Evaluation of the Parameter R	91
43	Average Value of R as a Function of the Distance from the Sample Surface	93
44	Average Value of R as a Function of the Sample Thickness	94

Figure	Title	Page
45	Schematic of the Apparatus for Porous Carbon High Temperature Flow Tests	102
46	Porous Carbon Cold Flow Characteristics	105
47	Porous Carbon Sample: Temperature Distribution	107
48	Porous Carbon Sample: Temperature Distribution	108
49	Porous Carbon Sample: Temperature Distribution	109
50	Pressure Drop as a Function of Average Temperature Through Porous Carbon Sample	111
51	Porous Carbon High Temperature Flow Characteristics	112
52	Porous Carbon Flow Parameters as a Function of Temperature	114
53	Comparison of Theoretical and Experimental Values of Mass Flow Rate Through Porous Carbon Sample	117
54	Comparison of Theoretical and Experimental Values of Mass Flow Rate Through Porous Carbon Sample	118

NOMENCLATURE

Symbol	Definition
a, b, c, c_w, c_1, c_2	Flow coefficients
A	Area
A_c	Area of high temperature central region of porous segments outside surface
A_s	Area of peripheral region of porous segments outside surface
A_{ATT}	Arc attachment area
A_1, A_2	Constants
C_1, C_2, C_3	Constants
c_p	Specific heat
$\bar{D}_p$	Mean particle diameter
I	Arc current
K	Permeability
Kg	Gas thermal conductivity
Kw	Porous matrix thermal conductivity
l	Porous segment thickness
L	Fundamental unit of length
M	Fundamental unit of mass
$\dot{m}$	Mass flowrate
$(\dot{m}/A)_{T_{wc}}$	Mass flowrate per unit area through the high temperature central region of porous segments
$(\dot{m}/A)_{T_{ws}}$	Mass flowrate per unit area through the peripheral region of porous segments

Symbol	Definition
n	Particle number density
N_{Re}	Reynolds number
p	Pressure
$\overline{p}$	Average pressure
$\dot{q}_R$	Radiative heat flux per unit area
R^*	Gas constant
T^*	Fundamental unit of time
T	Temperature
T_{ATT}	Temperature of arc attachment area on porous anode inside surface
T_g	Gas temperature
T_i	Uniform temperature of porous segment inside surface
T_w	Uniform temperature of porous segment outside surface
T_{wc}	Temperature of the central region of porous segment outside surface
T_{ws}	Temperature of the peripheral region of porous segment inside surface
T_∞	Transpiring gas temperature upstream porous segment
u	Velocity
V	Arc voltage
x, y, z	Space coordinates
x_w	Space coordinate of porous segment outside surface
W, X, Y, Z	Dimensionless numbers

Symbol	Definition
Δp	Total pressure drop across porous segment
Δp_6	Pressure drop across anode nozzle
ε	Total emissivity
η	Viscosity
ρ	Density
σ_B	Stephan-Boltzmann constant
σ_g	Logarithmic standard deviation

ABSTRACT

In this work a new approach is described for the generation of monodisperse aerosols which are presently of interest for all kinds of medical and air pollution research, including evaluating aerosol sampling and measuring equipment, air cleaner evaluation, and for interrelated studies.

Although numerous research-type aerosol generators have been developed or proposed for generating monodisperse aerosols in the submicron range, there is at present no reliable method available for generating ultrafine monodisperse aerosols for a wide spectrum of materials.

The method presented here, which has been explored during the past two years, makes use of a transpiration-cooled anode in a high intensity arc. In this situation the aerosol is generated continuously by ablation of the anode material at the steady arc attachment spot, which is the hottest part of the anode surface. The transpiring gas passing through the anode provides quenching of the vapor and immediate dilution of the generated particles in the vicinity of the anode surface, in this way avoiding coagulation and formation of agglomerations. The results show that the aerosol generator described in this report is suitable for generating aerosol particles whose mean diameter can be controlled in the range from 50 Å to about 1 μ, with a logarithmic standard deviation

mainly in the range of $\sigma_g = 1.1 \div 1.2$; in other words, the transpiration cooled plasma torch particle generator can provide practically monodisperse aerosols of controlled size anywhere in the submicron range.

I. INTRODUCTION

The recent years' problems associated with air pollution due to atmospheric particulates and the health hazards caused by the inhalation of fumes have attracted increasing interest. Vast research efforts have been made or are under way to provide a scientific base for the solution of these problems. As a consequence, the demand has been increasing for monodisperse aerosol particles of controlled size and shape, which are necessary for laboratory experiments on motion, charging, coagulation, and precipitation of particles, for evaluating aerosol sampling and measuring equipment, for air cleaner evaluation, and for biomedical and inhalation studies. For systematic experimental studies on these phenomena, aerosol particles must be available which have, ideally, all the same size (monodisperse aerosols) and shape. Their size should range from a few Angstroms to several microns, in order to cover all the needs encountered in the above-mentioned investigations. The generation of particles of controlled size in the range beyond 1 μ does not pose a problem, and such particles are already commercially available.

The generation of submicron particles is much more complex [1-16] and the need for such aerosols is becoming more and more pressing. Although numerous research-type aerosol generators have been proposed, at the present time no reliable methods are available to generate monodisperse

aerosols of controlled size in the submicron range (ultrafine aerosol) for a wide spectrum of materials. It is the goal of this work to close this gap.

In the first part of the report, the high intensity arc apparatus with the multiple-plenum chamber transpiration-cooled porous anode and the auxiliary equipment are described. In the second part, parameters are evaluated and experimental results are given which determine the performance of the arc itself and of the porous anode and the advantages of the multiple plenum chamber system are demonstrated. In the third part, the ultrafine carbon aerosol particles, generated by ablation from the anode material, are examined. The aerosol sampling technique, based on the use of an Electrostatic Particle Counting Mobility Analyzer System is described. The experimentally determined size distributions of the aerosol particles are given, and the parameters which characterize the aerosol (i.e., mean particle diameter, logarithmic standard deviation, and concentration) are evaluated.

Finally, a relation between the arc parameters, the anode cooling gas flow rate, and the above-mentioned aerosol size distribution characteristic parameters is found.

Since there are no data available in the literature on the flow of gases through porous materials at high temperature levels, it was mandatory to devote considerable effort to this problem. The characteristics of gas flow through porous

carbon matrices are experimentally determined over a temperature range from 300 °K to 2000 °K, and a theoretical model is derived to correlate the experimental results. These results, which are reported in the Appendix, are indispensable for the interpretation of the performances of the transpiration-cooled plasma torch; and they are frequently referred to in this work.

II. AEROSOL GENERATOR: EXPERIMENTAL APPARATUS

A. Plasma Torch

The plasma torch consists essentially of a water-cooled thoriated tungsten cathode with a conical tip and a nozzle-shaped porous carbon anode supported by a copper and brass structure. In this supporting structure, five plenum chambers are located, which regulate the argon mass flowrate transpiring through five different sectors of the porous anode.

A schematic drawing of the plasma torch is represented in Figure 1.

The conical thoriated tungsten cathode tip (1) is imbedded in a copper holder (2), which in turn is supported by a brass structure (3). The cooling is provided by a water jet impinging on the base of the cathode tip and emerging from a stainless steel tube (4), located inside the hollow cathode holder and coaxial with it. A fine thread on the outer surface of the brass holder allows for a vertical positioning of the cathode tip within an accuracy of 0.1 mm by rotating the bell-shaped brass piece (5). This piece can slide into a groove formed by the ring (6) and the supporting brass plate (7), its vertical position remaining fixed with respect to the anode.

The entire cathode assembly, so far described, can be moved on a horizontal plane in two mutually perpendicular directions. For this purpose, two rectangular systems of

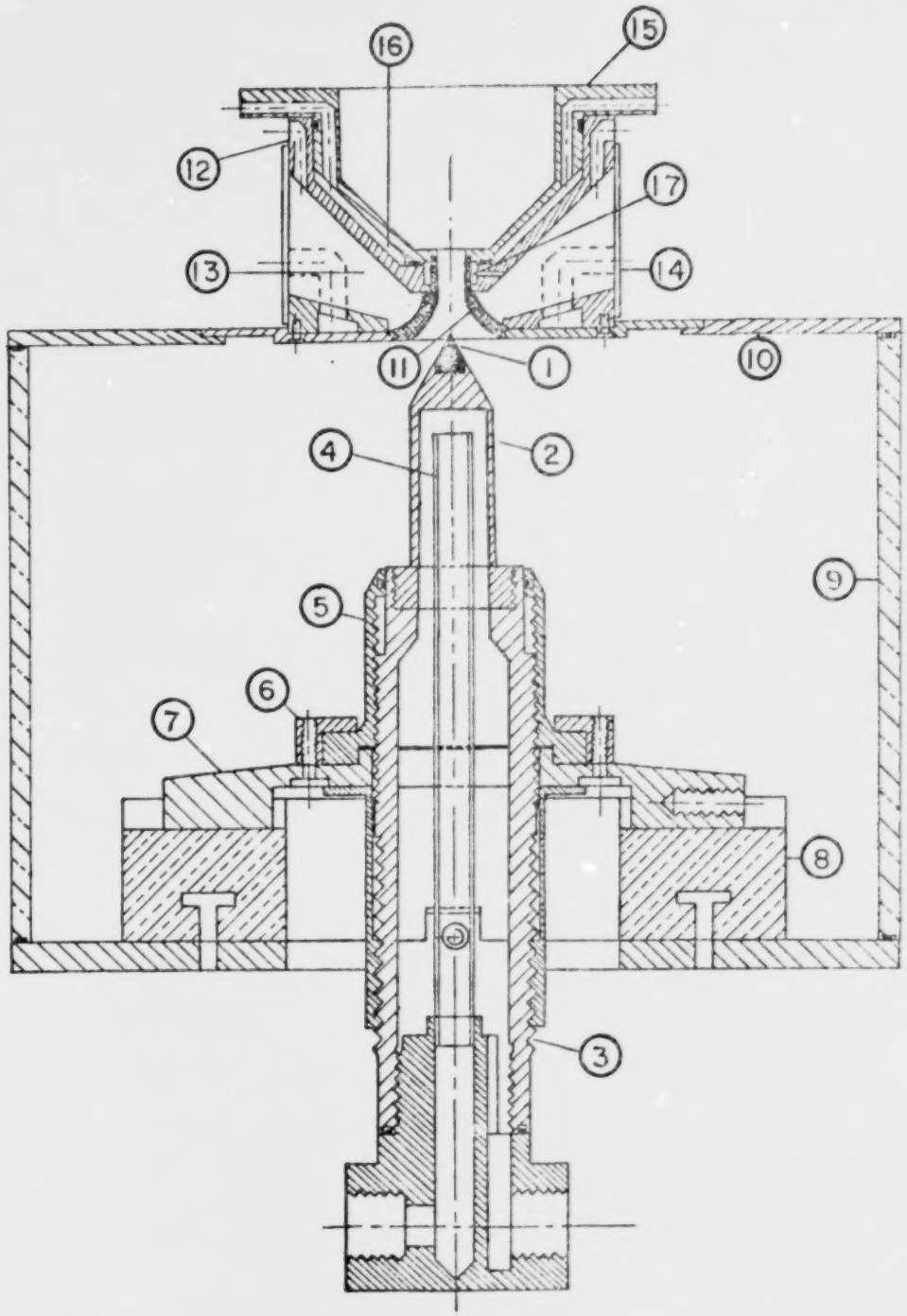

FIG. 1 SCHEMATIC OF THE PLASMA TORCH

grooves, normal to each other, are machined on the upper and lower surface of the teflon ring (8), which electrically insulates the cathode from the rest of the apparatus. Micrometric screws drive the cathode holder in these grooves, permitting an accurate setting (within 0.1 mm) in a horizontal plane.

A plexiglas cylindrical structure (9), fixed at the anode lower copper plate (10) seals the arc from the atmosphere. A small amount of argon is blown tangentially along the inside surface of the plexiglas cylindrical wall, thus providing a swirl flow around the cathode tip which stabilizes the arc [17].

A system of "O" rings seals the cathode and the plexiglas chamber from the outside atmosphere, allowing, at the same time, vertical movements of the cathode with respect to the anode.

The nozzle-shaped porous carbon anode (11), coaxial with the cathode, is supported by a copper and brass holder. In the copper part of this support (12), there are four identical plenum chambers (13), each feeding cooling gas to an anode sector of about 88°. A cylindrical plexiglas window (14) simultaneously seals, by means of "O" rings, each plenum chamber from the outer atmosphere. Through it, pyrometric readings of the outer surface temperature of each of the four segments of the porous anode are possible. Each plenum

chamber is equipped with an inlet for the cooling gas and with a pressure tap.

Since every plenum chamber is perfectly sealed from its neighbor, the pressure can be varied independently. Consequently, the argon mass flowrate transpiring through the corresponding sector of the anode may be varied without altering the mass flow through the other sectors.

The brass portion of the supporting structure (15), mounted on top of the copper support, generates a water passage (16) used for additional water cooling of the anode holder. This water cooling is not necessary for normal torch operation, but it has been introduced as an additional precaution in consideration of the efforts devoted to the construction of this anode holder.

The brass piece also provides the upper sealing of a fifth small cylindrical plenum chamber (17) which surrounds the upper portion of the anode nozzle. Since in this region the heat flux to the nozzle walls is relatively small and uniform, this plenum chamber is not divided in independent sectors.

It should be pointed out that the porous anode is not subdivided into five sectors; it consists of one single piece of porous carbon and, therefore, does not present on the inner surface any nonuniformities which would result in preferred attachment spots for the arc.

B. Particle Collection Chamber

The plasma jet, containing the particles ablated from the porous carbon anode, emerges from the anode nozzle and enters a particle collection chamber schematically represented in Figure 2. A brass cylinder 80 cm long, 20 cm in diameter is located vertically on top of the anode holder and coaxial with it. A copper tube wrapped around its external surface and sodered to it provides water cooling. Ten plexiglas windows are located along the cylinder allowing an almost unobstructed viewing of the plasma jet and of the plasma inside the chamber. An argon inlet is provided near the base of the cylinder as a provision for further particle dilution.

From the collection chamber, the particles enter the analyzing system in which the size distribution of the suspended particles is determined.

C. Control Panel

The instruments mounted on the control panel allow for controlling and measuring the argon mass flowrate and the pressure in each of the six plenum chambers, as well as the cathode and anode holder cooling water mass flowrate.

The distilled water closed circuit, which provides the cooling for the anode holder, consists of a commercial water pump with an incorporated heat exchanger, pressure gauges, calibrated Fisher and Porter flowrators, and needle valves for flowrate control.

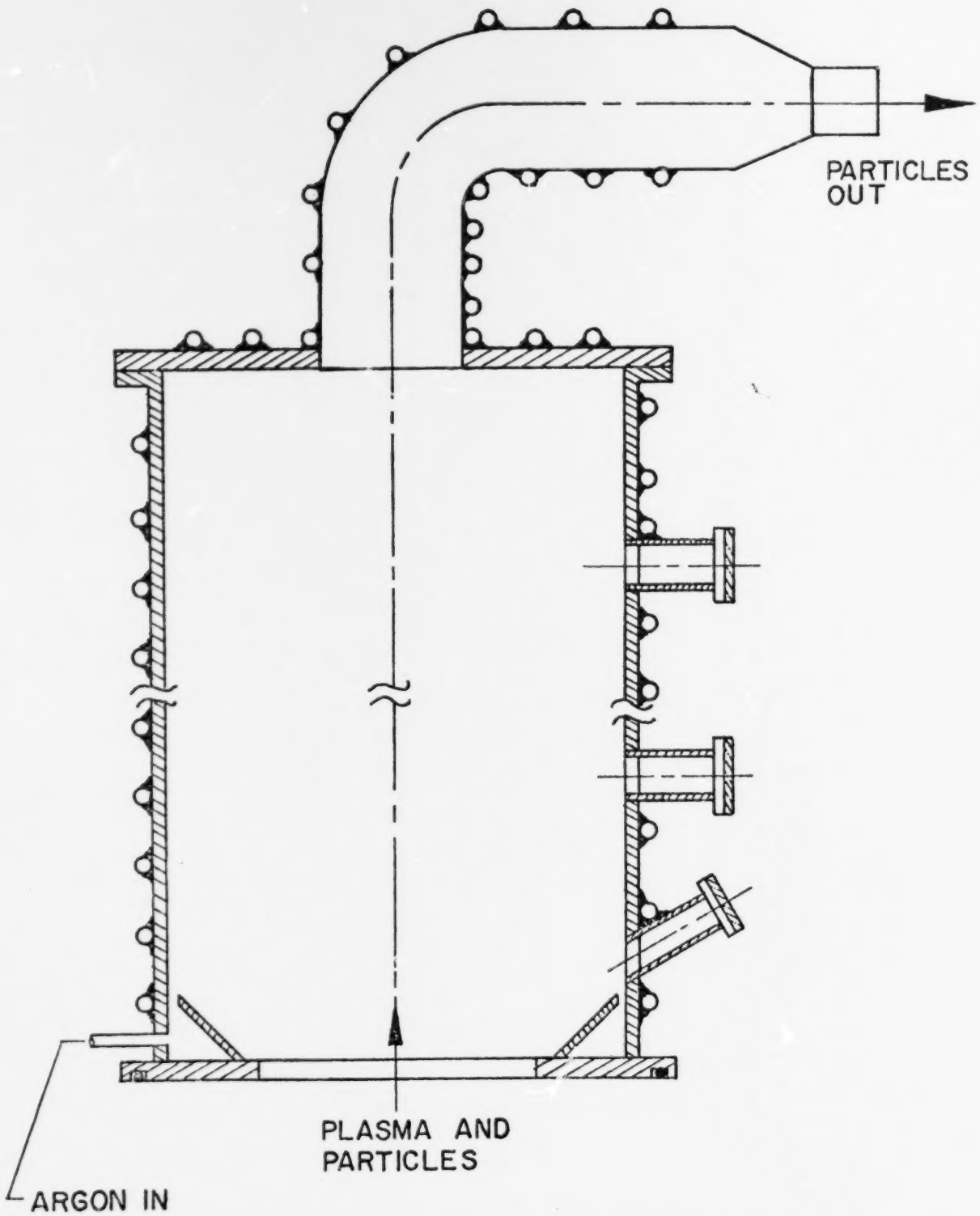

FIG. 2 SCHEMATIC OF THE PARTICLE COLLECTION CHAMBER

A sufficient cooling water flowrate is provided by a pressure of 10^6 Kg/msec^2 at the pump outlet. An analogous circuit provides the cathode cooling water.

The transpiring gas circuits are represented in Figure 3. The plenum chambers are indicated by the six symbols in squares numbered from 1 to 6. The first four represent the plenum chambers which feed transpirant gas through the four main sections of the anode. The fifth represents the plenum chamber connected to the downstream portion of the anode, and the sixth indicates the cathode plenum chamber.

When the valves designated by V_2 are closed and the valves denoted by V_1 are open, the V valve regulates the flow in all the first four plenum chambers simultaneously and yields the same pressure and, therefore, the same argon mass flowrate in all four of them without the arc in operation. By partially closing one of the valves V_1, which were initially open, the mass flowrate through the corresponding plenum chamber can be reduced. By partially opening one of the valves V_2, which are initially closed, the mass flowrate through the corresponding plenum chamber can be increased.

This system permits a reliable and quick control of the flow and the associated temperature of the four anode sections which operate under the most critical conditions because the arc may attach to any one of them.

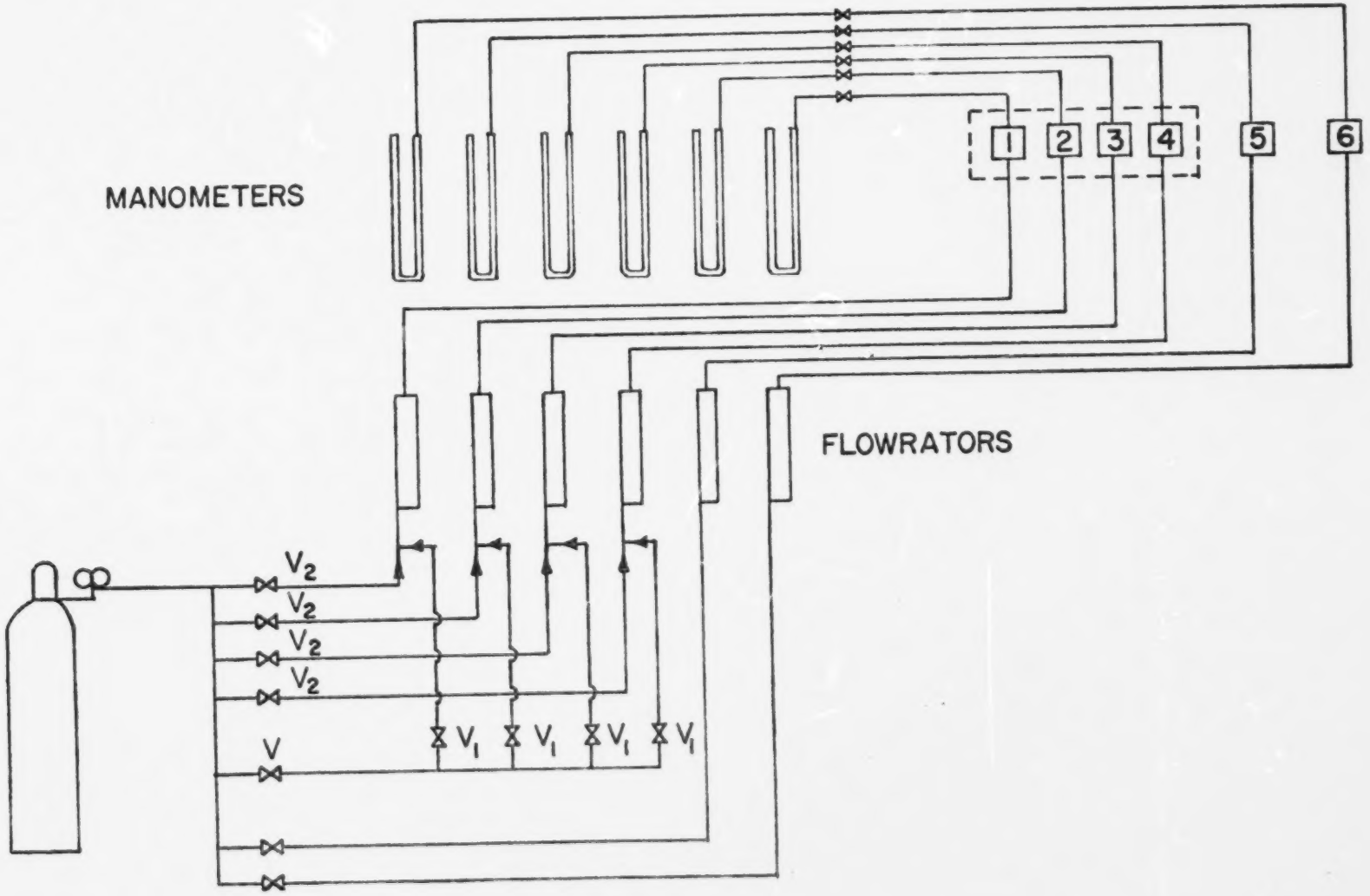

FIG. 3 ARGON FLOW CONTROL CIRCUITS

The operating procedure used during the experimental runs will be described later.

The gas circuits for the two plenum chambers, 5 and 6, are standard and will not be discussed here.

D. Auxiliary Equipment

The electrical power for the arc is supplied by a Miller 40 Kw rectifier [17]. Its associated current regulating rheostat, on-off switch, and high frequency starter are incorporated into a commercial control console, separated from the main control panel described above.

Stability during arc operation and extension of the current range is provided by placing an adjustable water-cooled resistor of approximately 1.2 Ω maximum resistance in series with the electrical circuit. The resistor is made from twelve 1/4" diameter stainless steel tubes 90 cm long. Continuous variation of the resistance is accomplished by means of copper sliding contacts which connect the tube in pairs and step variations by means of copper plugs located at the end section of each tube by which the tubes can be connected in series or grouped in parallel according to need.

Provisions are taken in the design to allow for thermal expansion of the Joule heated resistor tubes; therefore, a power dissipation in the order of 40 Kw is possible.

All the cooling water is provided by a distilled water commercial pump and reservoir with built-in heat exchanger.

III. TRANSPIRATION COOLED ANODE IN HIGH INTENSITY ARC: EVALUATION OF GOVERNING PARAMETERS

A. Cold Flow Tests and Preliminary Observations

In preliminary cold flow tests, the total pressure drop across each of the four main anode sectors is measured as a function of the transpiring argon mass flowrate. The results are shown in Figure 4.

The pressure drop is then calculated from the measured values of the mass flowrate using Equation (A.11) of the Appendix. The room temperature values for the flow constants A* and B* are derived from Figure 52. For the area of the sector, an average value between the area of the inner and outer surface is assumed which is justified because the wall thickness is constant over the entire sector and small compared to the other dimensions. The results of the calculations are represented by the asterisks in Figure 4.

The data for all four sectors can be correlated by the curve and the theoretical values are in good agreement with the experimental data. Moreover, the readings pertaining to one plenum chamber are not affected at all by the value of the pressure in the adjacent chamber leading to the following conclusions: the four sectors are indeed identical, as far as the flow of argon is concerned, avoiding in this way undesirable nonuniformities and asymmetries of the anode nozzle flow; each plenum chamber is perfectly sealed from

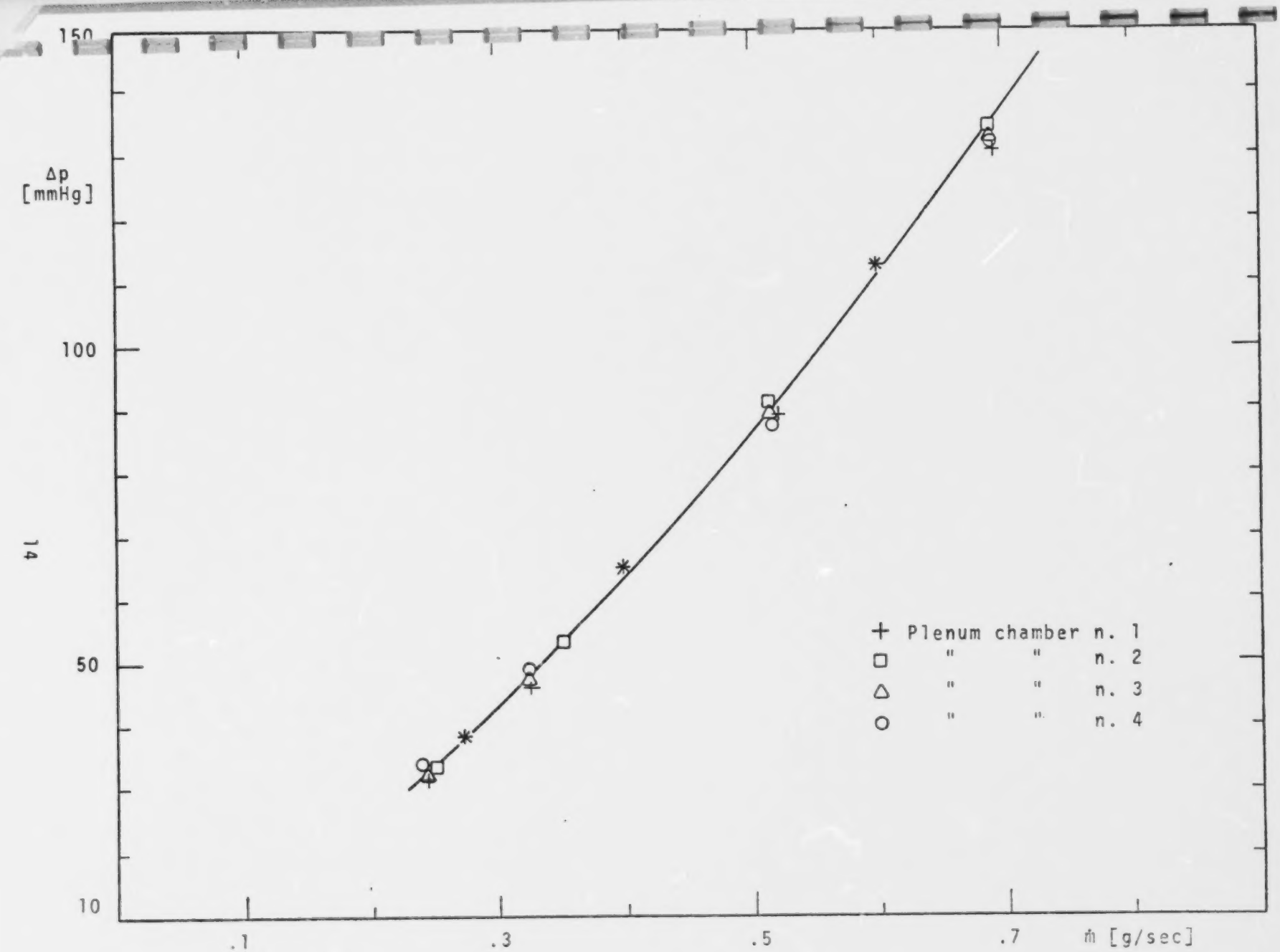

FIG. 4 POROUS ANODE SECTORS: COLD FLOW CHARACTERISTICS

its neighbors, as well as from the outside atmosphere; the values of the flow constants A* and B*, experimentally determined as described in the Appendix, and the average value for the anode sectors area are consistent and can be used in Equation (A.11) of the Appendix to predict the values of the pressure drop or of the mass flowrate within a few percent.

The cold flow tests are repeated after each arc run to check for possible damages of the porous anode or of the seals of the plenum chambers. The data can always be correlated by the curve of Figure 4 which proves that no deterioration of the anode during operation occurred.

Trial arc runs are then performed in order to establish an operating procedure suitable for the new multiple plenum chamber system and to qualitatively assess its effects on the arc and arc attachment spot behavior. It is found that the arc can be operated steadily in a current range from 60 to 120 Amp over a wide range of argon mass flowrates without any tendencies to form preferred attachment spots on the anode surface. The arc attaches in the region of the anode where the transpiring argon mass flowrate is controlled by the four plenum chambers. The size of the arc attachment on the anode surface is of the same order of magnitude as the area of one sector connected to one single plenum chamber. The arc attaches to that sector through which the transpiring argon

flowrate is a minimum; however, once the arc attaches to this particular segment, it tends to remain there and moves to a new segment only when the difference in the transpiring gas flowrate becomes very large.

The operating procedure described here is adopted for the tests performed in this work. Once the sector on which the arc should attach is chosen, the corresponding valve V_1 is closed; and valve V_2 controls the argon mass flowrate through the segment in a range around 1 Kg/m^2sec. The valves V_2 controlling the mass flowrate to the other three segments are closed, and the V_1 valves are opened completely. Then, by means of valve V, the value of the flow through the remaining three segments is set to approximately 3 Kg/m^2sec. After initiation of the arc, the attachment occurs on the preselected sector, which becomes hot and starts to glow. Its temperature level is controlled by means of valve V_2 which controls the mass flowrate passing through the segment. By means of valve V, the mass flowrate in the other three segments is adjusted simultaneously to the desired value. In this way, the generation of undesirable asymmetries in the anode nozzle flow may be prevented.

B. Arc Characteristics

Arc voltages are measured as a function of the arc current, for different values of the argon mass flowrate passing through the five anode sectors, and of the flowrate providing the cathode swirl.

Preliminary tests showed that the value of the mass flowrate transpiring through the fifth cylindrical sector in the downstream portion of the anode has no influence on the arc characteristics. This is so because the arc attaches upstream from this segment so that only the noncurrent-carrying emerging plasma jet is affected. The experimental results show that the arc characteristics are only a function of the total mass flowrate, $\dot{m}_t$, passing through the four main anode sectors and that they are independent of the mass flow through individual sectors.

In Figure 5 the measured arc voltages are plotted versus the arc current for four different total mass flowrates. The cathode swirl mass flowrate is an order of magnitude smaller than that through the four main sectors. Therefore, its variation has a negligible effect on the arc characteristics even when changed by more than 100 percent, as shown in Figure 5 by the triangular symbols (▼▽).

For currents below 55 Amp, the arc becomes unstable and its attachment spot moves erratically along the lower edge of the anode nozzle. This instability increases with increasing transpiring mass flowrate, probably because the relatively "weak" arc is strongly affected by fluidynamic forces of the gas flow. At currents beyond 120 Amp, the arc attachment tends to move downstream toward the end of the anode nozzle in the region of the single cylindrical plenum chamber which

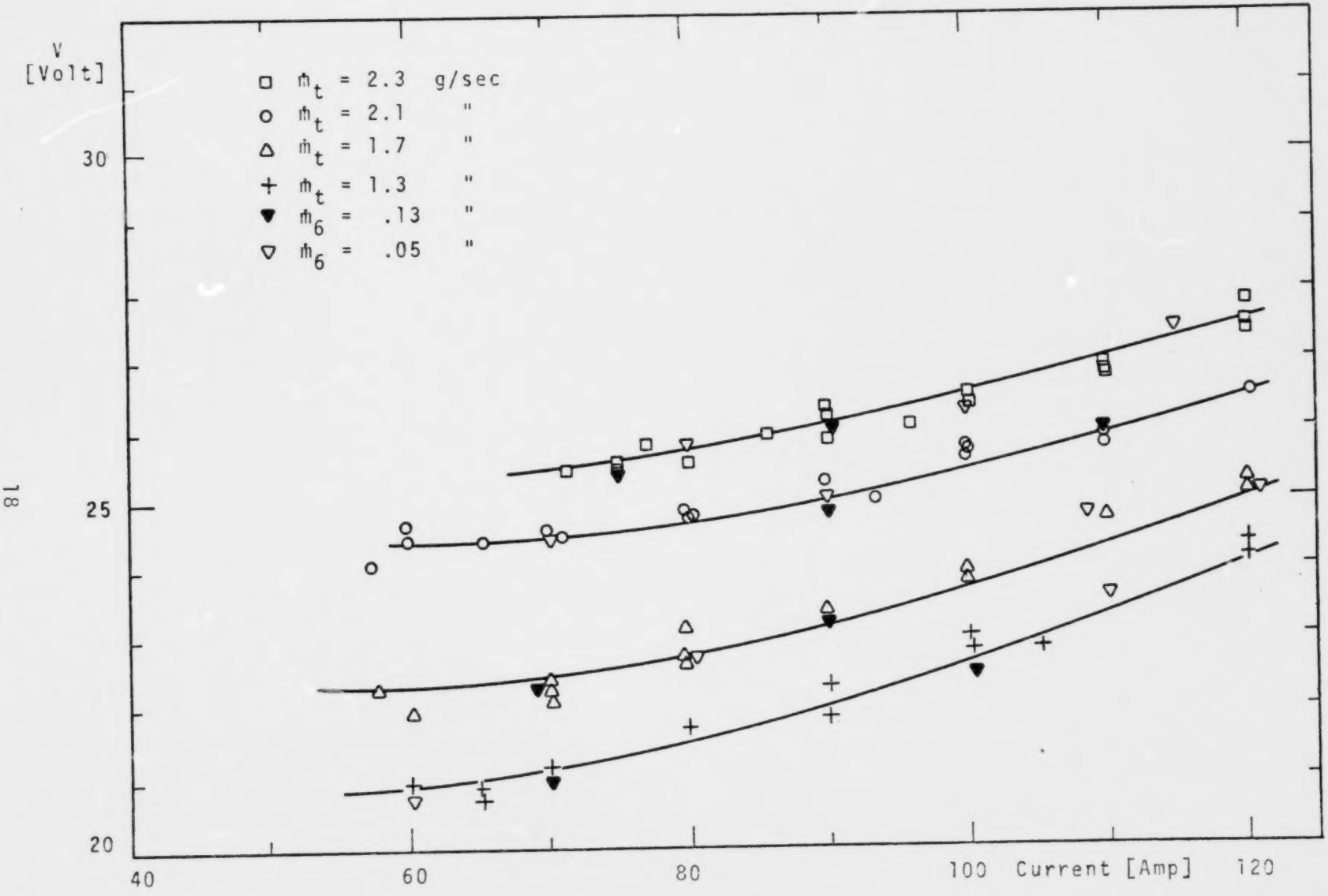

FIG. 5 ARC CHARACTERISTICS

controls the gas flow over the entire nozzle circumference. Therefore, a current of 120 Amp is considered as the upper limit for the experimental runs. The tendency of the arc to move downstream at high currents is enhanced with increasing mass flowrate.

From Figure 5, by crossplotting, the curves of Figure 6 are obtained representing the arc voltage as a function of the mass flowrate for four different currents ranging from 60 to 120 Amp. The voltage increase with current and mass flowrate has been described in the literature [18-21] for the case of an arc with axial flow and a plane, water-cooled anode. In principle, the same arguments hold for the case of the transpiration cooled, nozzle-shaped anode used in the present work. By increasing the argon mass flowrate, i.e., the flow velocity, the arc length increases due to fluidynamic interactions of the gas flow with the arc which behaves in this situation essentially as a body impermeable to the external gas flow. A second effect is the increase in energy exchange between the plasma column and gas flow with increasing mass flowrate. The response of the arc column to higher energy losses is an increased field strength which compensates for these losses [18]. With increasing current the energy exchange between the arc column and the cold gas flow increases because the losses of a plasma column are a function of the plasma surface area and the diameter of the arc column grows

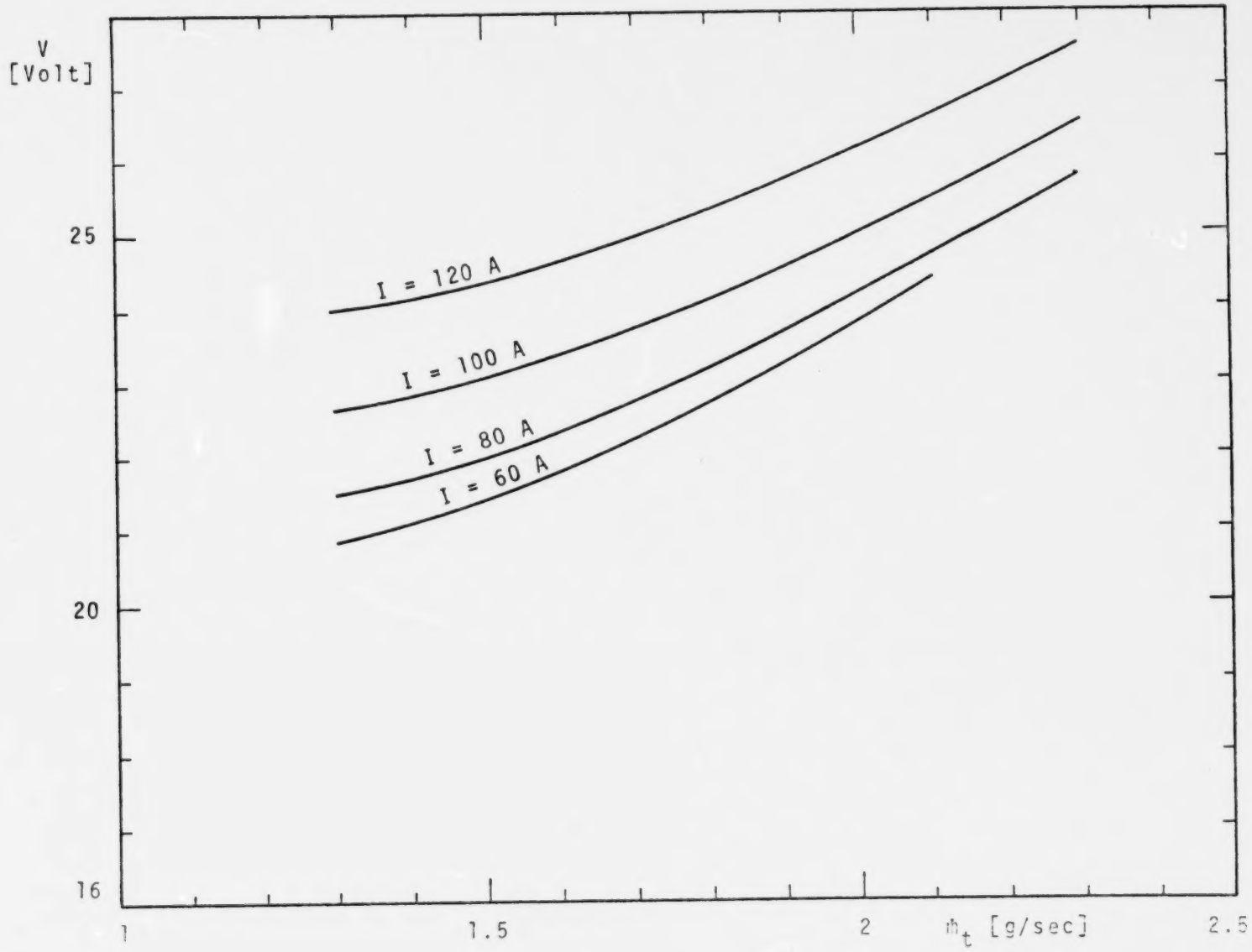

FIG. 6 ARC CHARACTERISTICS

with increasing current in the current range pertaining to the present investigation.

The results demonstrate that the influence of the mass flowrate on the voltage decreases with increasing current. This is due to the fact that the Lorentz force balancing the convective forces, exerted [22] on the arc by the cold argon mass flow, increases with current.

C. Segmented Porous Anode: Transpiring Flow Characteristics During Arc Operation

The desired control over the operating conditions and performance of the new type of plasma torch, presented in this work, is possible only when the functional relationships between porous matrix temperature and transpiring gas flowrate and pressure are known inside of the main four sectors of the porous anode. Therefore, an extensive experimental investigation is conducted on the transpiring flow characteristics through each sector of the porous anode during arc operations.

The total pressure drop across each anode sector is measured as a function of the mass flowrate passing through the sector for arc currents ranging from 60 to 120 Amp. For each current, the measurements are subsequently performed with the arc attaching to each of the four anode sectors. Part of the experimental results are represented in Figures 7 and 8. It can be observed that the pressure drop across the segment

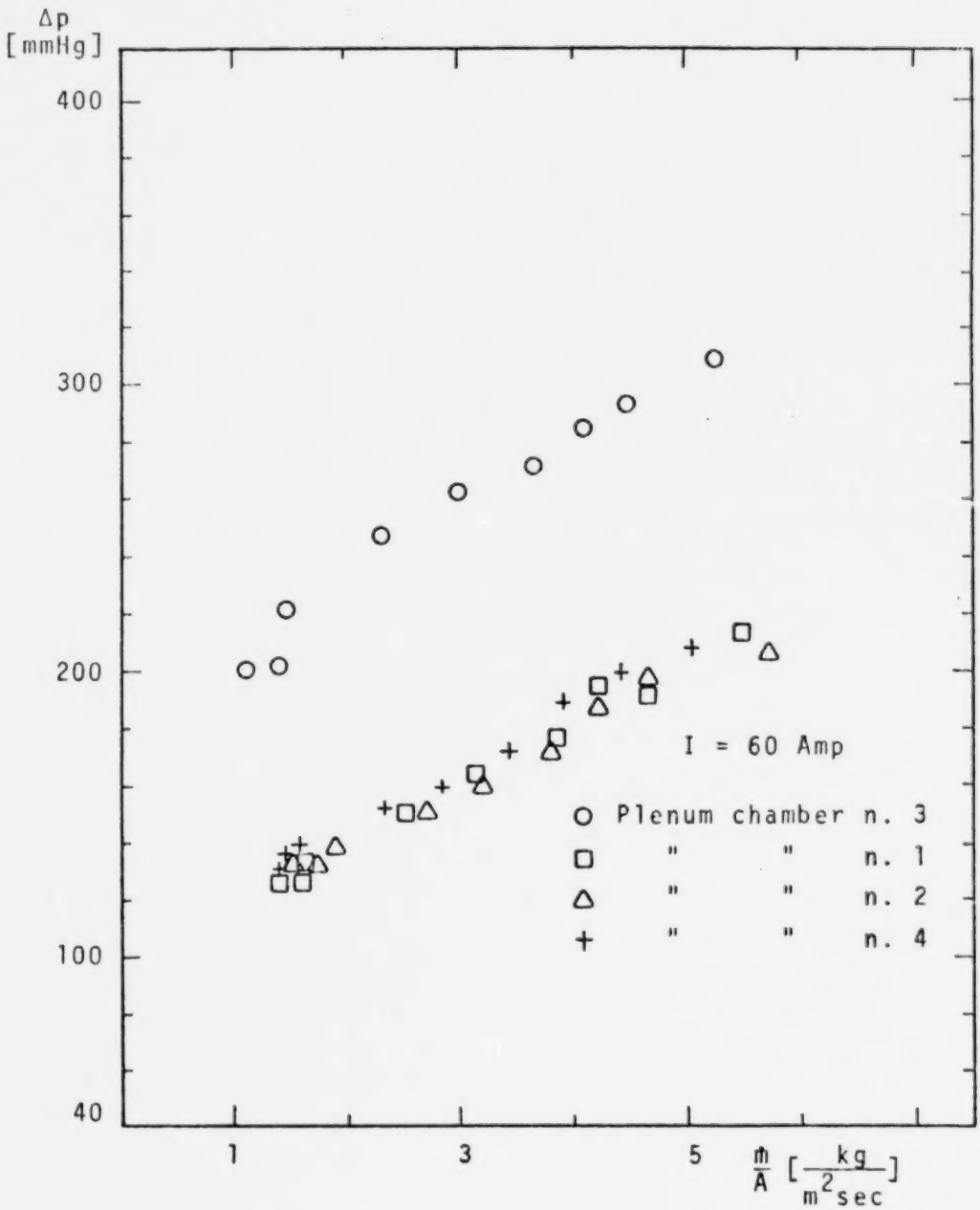

FIG. 7 POROUS ANODE SECTORS: FLOW CHARACTERISTICS DURING ARC OPERATION

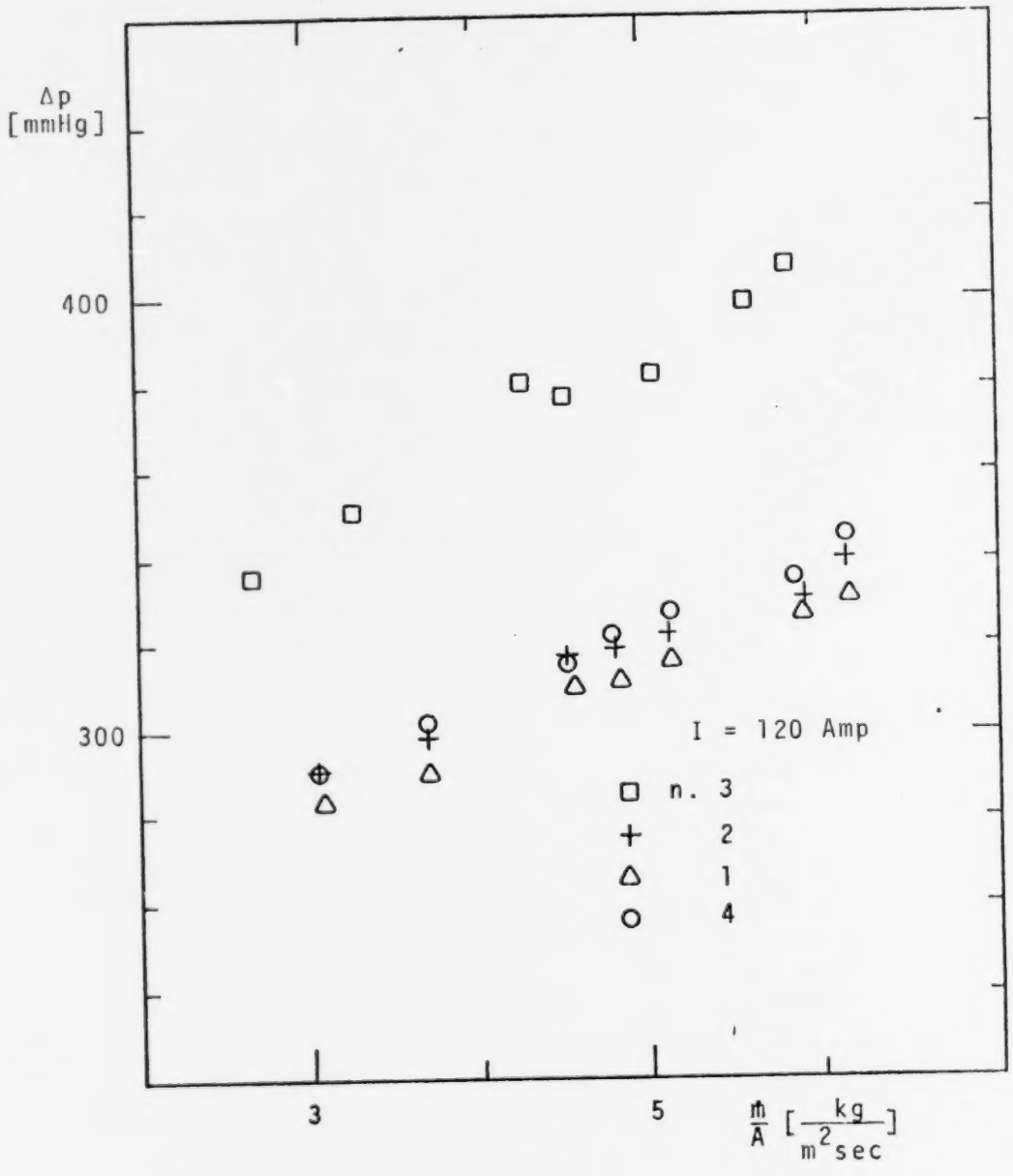

FIG. 8 POROUS ANODE SECTORS: FLOW CHARACTERISTICS DURING ARC OPERATION

where the arc is attaching is consistently higher than the one through th other segments. This indicates that the temperature of this segment is considerably higher than that of the other segments as it should be due to the high heat flux from the arc [23]. The observed pressure drops for the three segments on which the arc does not attach are very close to each other, indicating that the same temperatures can be attributed to each of these segments. This fact proves that the arc only attaches to one segment and that the size of the attachment spot is smaller than the surface area of the segment. It can be noticed, however, that the pressure drop across the segment opposite from the attachment spot tends to be slightly lower than that pertaining to the two adjacent segments. This is due to increased radiation and convection heat transfer from the arc to the two segments adjacent to the attachment spot and due to heat conduction to these segments from the high temperature arc attachment.

The pressure drop as a function of the arc current is also determined for transpiring mass flowrates per unit area varying from 2.5 to 5.8 Kg/m^2sec. Representative results are shown in Figures 9 and 10. These results are in agreement with the previously-described data, and they can be interpreted in a similar manner.

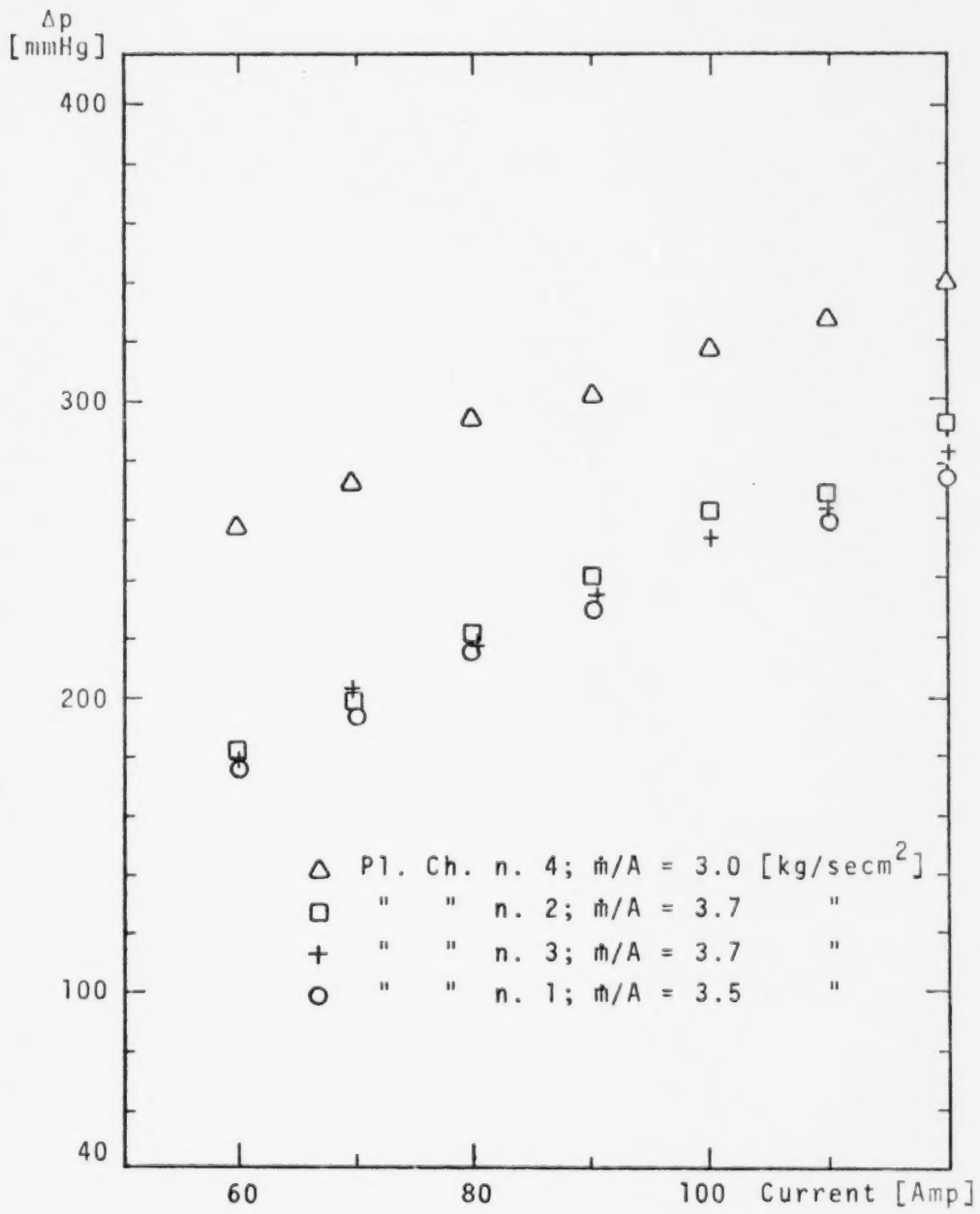

FIG. 9 PRESSURE DROP ACROSS POROUS ANODE SECTORS VERSUS ARC CURRENT

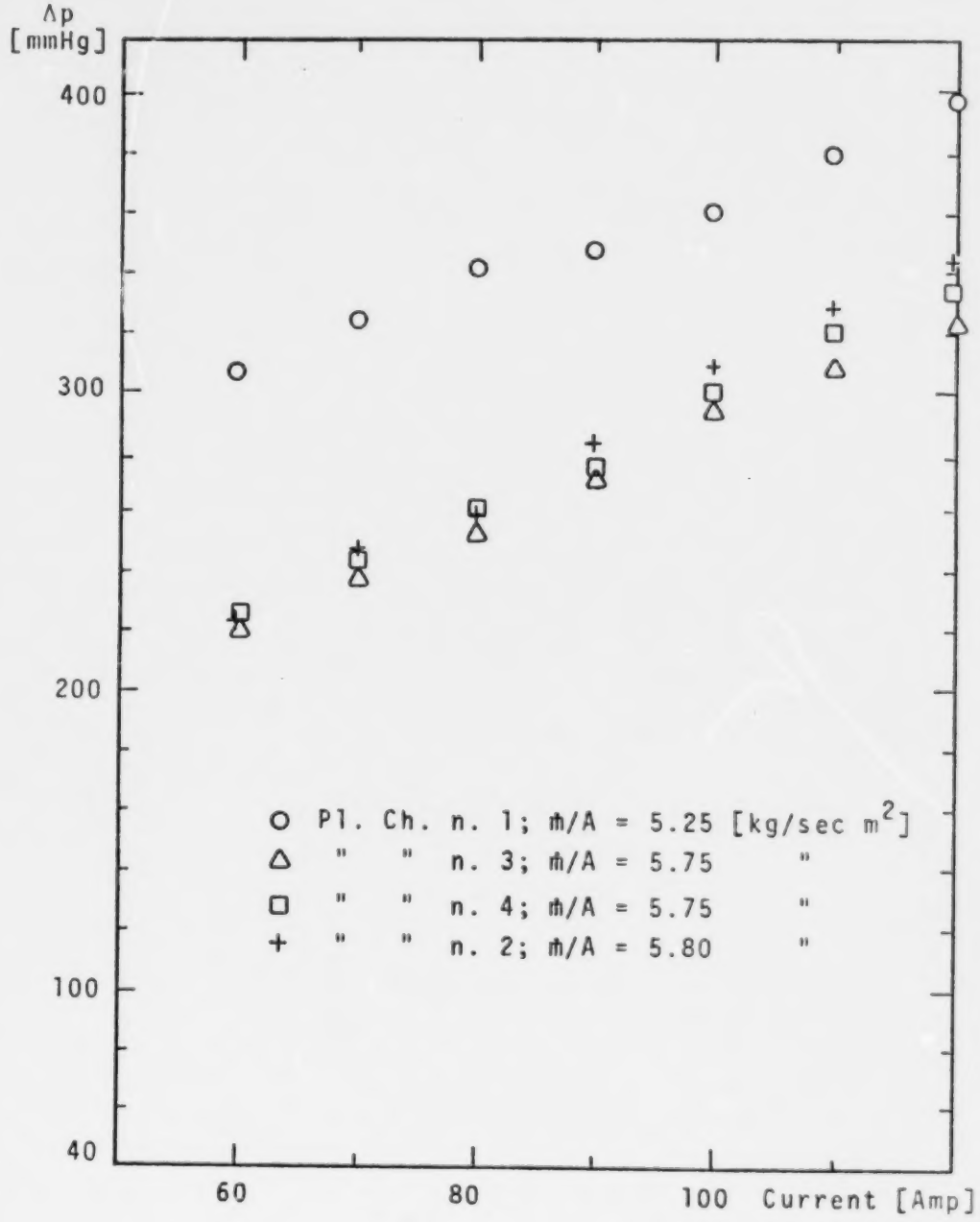

FIG. 10 PRESSURE DROP ACROSS POROUS ANODE SECTORS VERSUS ARC CURRENT

D. Temperature Distribution in the Porous Anode Sectors

1) Theoretical Analysis

For the sake of simplicity in this analysis, each sector of the porous anode is considered in a first approximation as a plane slab; and the steady flow of the gas transpiring through it is assumed to be one-dimensional. An energy balance within the porous material, per unit area normal to the flow direction, yields:

$$\frac{d}{dx}\left(K_w \frac{dT}{dx}\right) + \frac{\dot{m}}{A} \frac{d}{dx}\left(c_p T_g\right) = 0 \qquad (3.1)$$

Over the temperature range of interest, c_p may be considered constant and an average value may be taken for K_w.

The large specific surface of the porous matrix is reflected in a high value of the volumetric heat transfer coefficient for the heat transfer process between the porous wall and the transpiring gas. Hence, local values of gas and wall temperatures may be considered as equal. Equation (3.1), therefore, can be written:

$$\frac{d^2T}{dx^2} + \frac{\dot{m}}{A} \frac{c_p}{K_w} \frac{dT}{dx} = 0 \qquad (3.2)$$

With the two boundary conditions

$$T = T_w \text{ at } x = x_w \qquad (3.3)$$

and

$$- k \left(\frac{dT}{dx}\right)_{x = x_w} = \frac{\dot{m}}{A} c_p (T_w - T_\infty) + \dot{q}_R \qquad (3.4)$$

the solution of Equation (3.2) becomes

$$T = \left[(T_w - T_\infty) + \frac{A}{\dot{m}} \frac{\dot{q}_R}{c_p}\right] e^{\frac{\dot{m}}{A} \frac{c_p}{k} (x_w - x)} +$$

$$+ T_\infty - \frac{\dot{q}_R}{c_p} \frac{A}{\dot{m}} \qquad (3.5)$$

where

$$\dot{q}_R = \varepsilon \sigma_B (T_w^4 - T_\infty^4) \qquad (3.6)$$

In the above derivation, it has been assumed that all the energy conducted to the outer surface of the porous segment is either intercepted by the transpiring gas or lost by radiation. Equation (3.5) represents the temperature distribution inside the porous wall as a function of the mass flowrate per unit area and of the temperature of the outside surface. However, if the outer surface of the porous sector is not glowing, an accurate measurement of this temperature is rather difficult. Therefore, a method is proposed which does not require the knowledge of the temperature of the

outside wall, provided that this temperature is uniform over the sector surface.

If the continuity equation and the perfect gas law are introduced into Equation (A.7) of the Appendix for $\xi = 2$, one obtains

$$\frac{dp}{dx} = A^* \eta \frac{\dot{m}}{A} \frac{R^* T}{p} + B^* \left(\frac{\dot{m}}{A}\right)^2 \frac{R^* T}{p} \qquad (3.7)$$

where the values of the parameters A* and B* are represented in Figure 52 of the Appendix as a function of the temperature. The pressure in the plenum chamber can be measured easily and accurately (within 1%) and then serves as boundary condition in Equation (3.7). A value for the outside surface temperature of the porous sector is assumed, and the temperature distribution within the porous matrix can be determined from Equation (3.5). Correspondingly, a numerical solution of Equation (3.7) provides the pressure distribution across the porous matrix; and the total pressure drop may then be compared with experimental values. New values of the outside surface temperature of the porous sector are assumed until the calculated value of total pressure drop agrees with the experimental one. In this way, by iteration, the correct outside surface temperature may be found.

After the iteration process converges, the temperature distribution inside the porous sector is directly correlated

with the total pressure drop across the porous wall for the chosen mass flowrate transpiring through it. In this way, temperature distributions can be derived from pressure and mass flowrate measurements only which are much easier and more accurate than temperature measurements in this situation.

It is desirable to know the influence that errors in the pressure drop and mass flowrate measurements have on the temperature profile. In Figure 11, the temperature profile inside the anode sector is plotted for four values of the pressure drop. For each curve, the temperature profile corresponding to a pressure variation of ±3%, which may be considered as the maximum possible error of the pressure readings, is also plotted. It is obvious that the temperature error, induced by the errors in the pressure drop, never exceeds ±4%. An analogous procedure is followed for determining the influence of mass flowrate errors. In Figure 12, temperature profiles are plotted for four flowrates affected by an error of ±5%. It can be seen that the corresponding error in the temperature profiles never exceeds ±8%.

2) Results

Temperature profiles are numerically calculated as indicated above for pressure drops ranging from 60 to 460 mmHg and transpiring mass flowrates per unit area ranging from 0.5 to 5 $Kg/m^2 sec$. The temperature of the outside and inside surface of the porous sector are represented in Figures

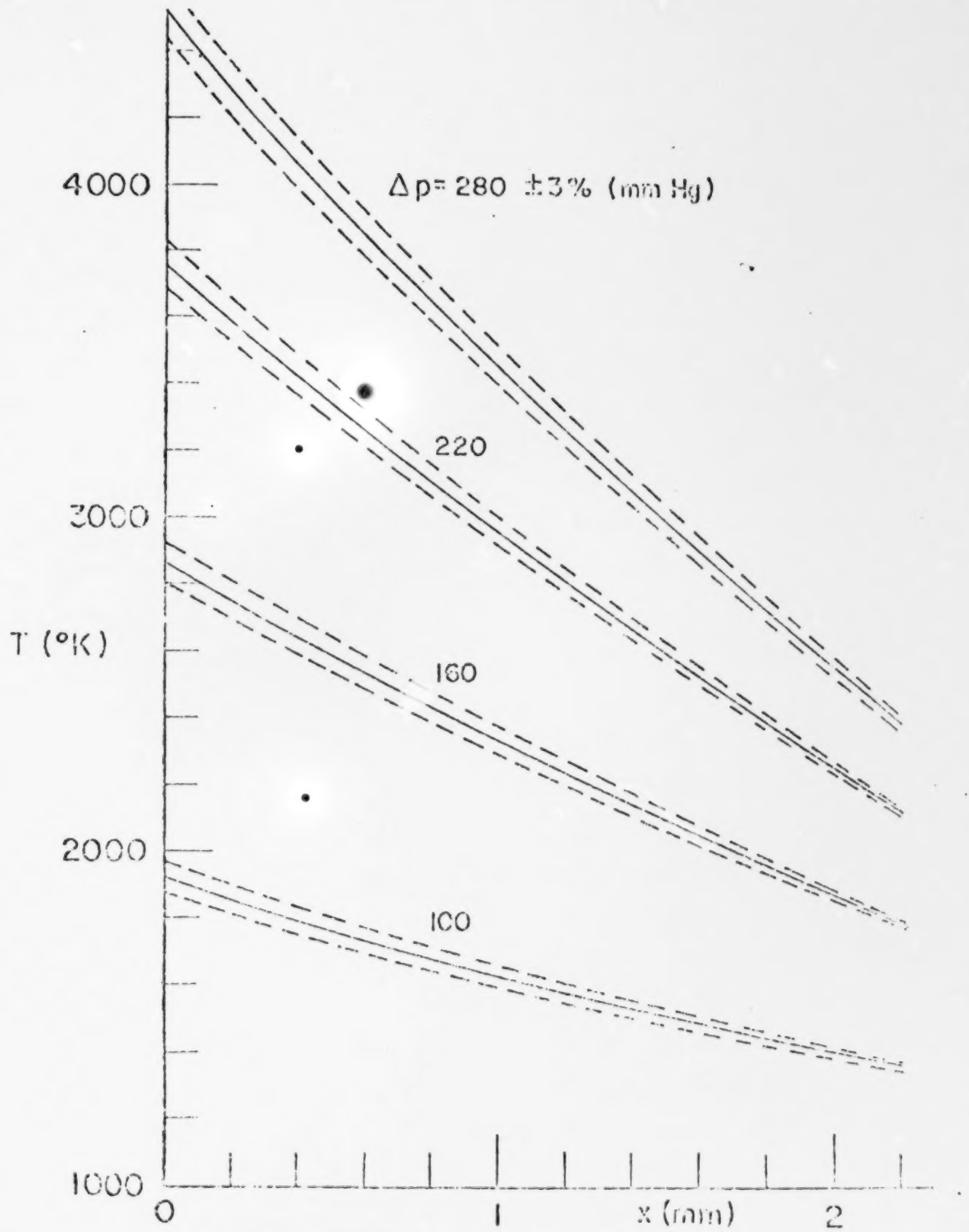

FIG. 11 INFLUENCE OF PRESSURE DROP VARIATION ON THE TEMPERATURE DISTRIBUTION INSIDE POROUS ANODE SECTORS

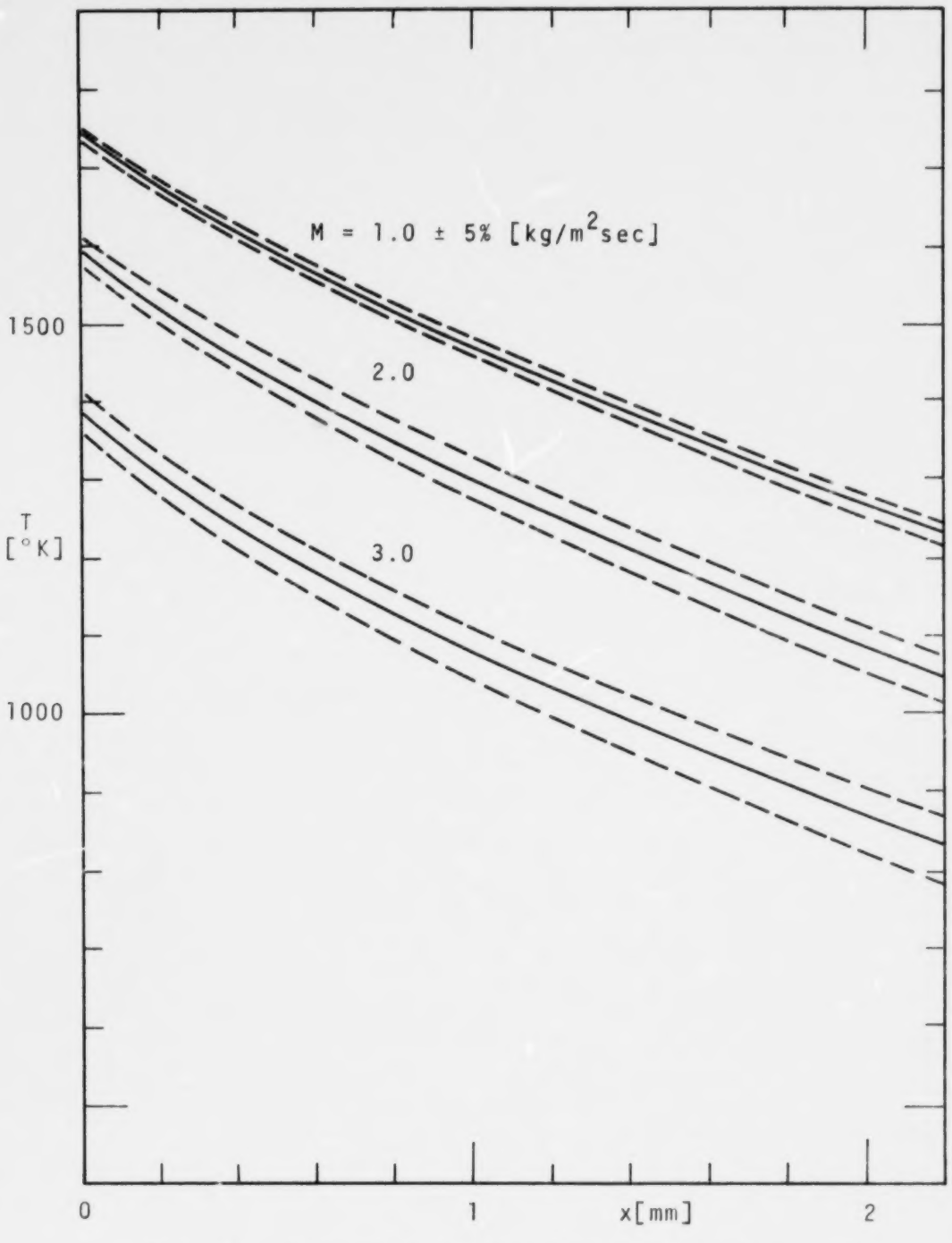

FIG. 12 INFLUENCE OF TRANSPIRING MASS FLOWRATE VARIATIONS ON THE TEMPERATURE DISTRIBUTION INSIDE POROUS ANODE SECTORS

13 and 14, respectively, as a function of pressure drop and transpiring mass flowrate. These figures permit a quick and accurate graphical determination of the inside and outside surface temperature of the porous anode, when the values of the pressure drop and the transpiring mass flowrate per unit area are known. For this reason, frequent reference to Figures 13 and 14 will be required in the following calculations.

In order to compare the theoretical predictions with experimental results, the mass flowrate passing through each sector, to which the arc does not attach, is decreased until the outside surface reaches glowing temperature. In this case, the temperature distribution appears uniform over the surface throughout the entire arc current range. The value of this temperature is then determined utilizing a calibrated optical pyrometer and compared with predictions derived from Figure 13. Figure 15 illustrates this type of comparison for currents of 60, 100, and 120 Amp. The results show that, for the sector to which the arc does not attach, a good agreement exists between theoretical and experimental values.

In Figures 16 to 18, theoretical and experimental temperature values of the outer surface of the porous sectors to which the arc attaches are represented as a function of the transpiring mass flowrate per unit area for currents of 60, 100, and 120 Amp. The experimentally determined

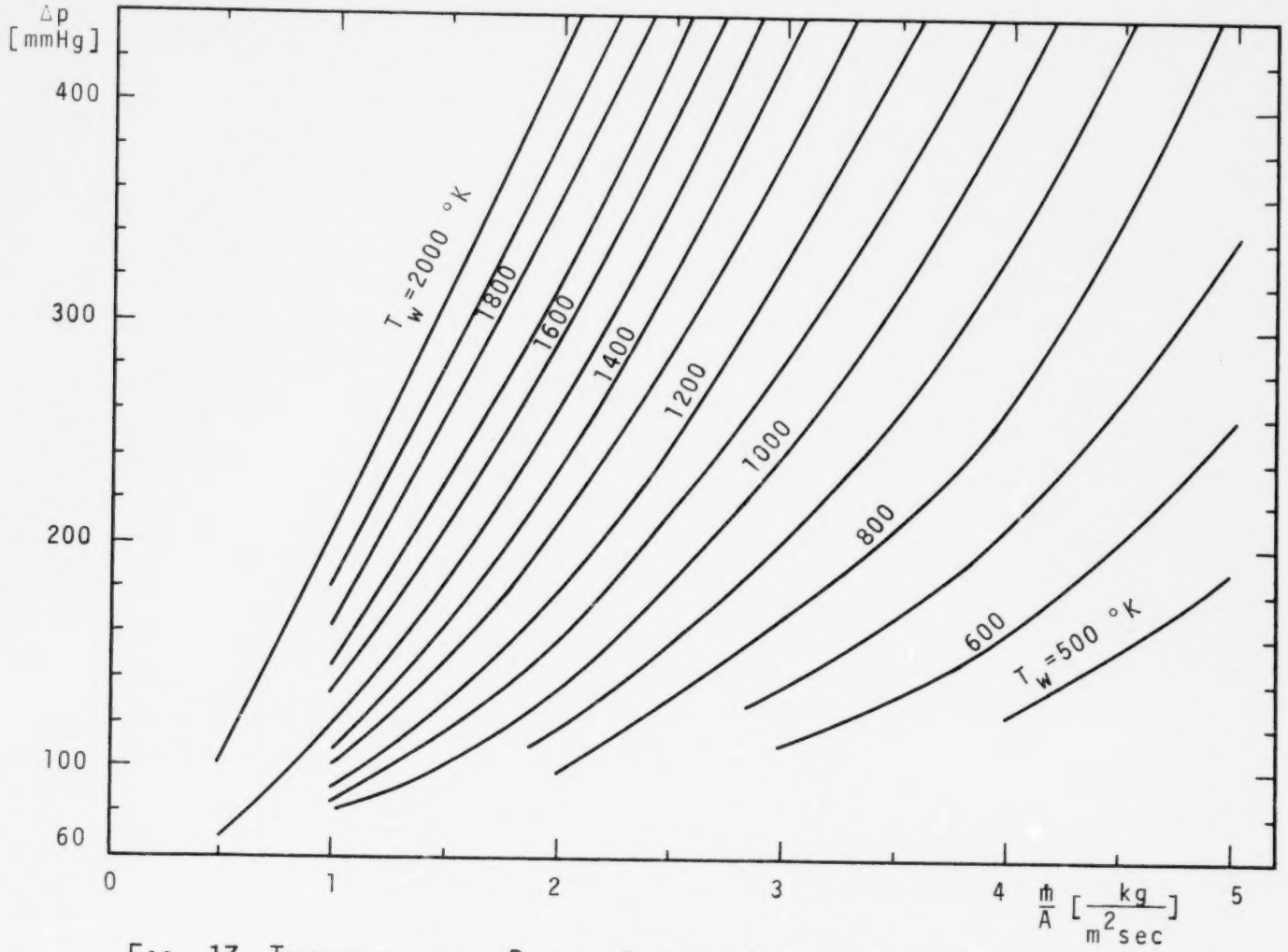

FIG. 13 TEMPERATURE OF POROUS SECTORS OUTSIDE SURFACE AS A FUNCTION OF TRANSPIRING MASS FLOWRATE PER UNIT AREA AND PRESSURE DROP ACROSS THE SECTOR

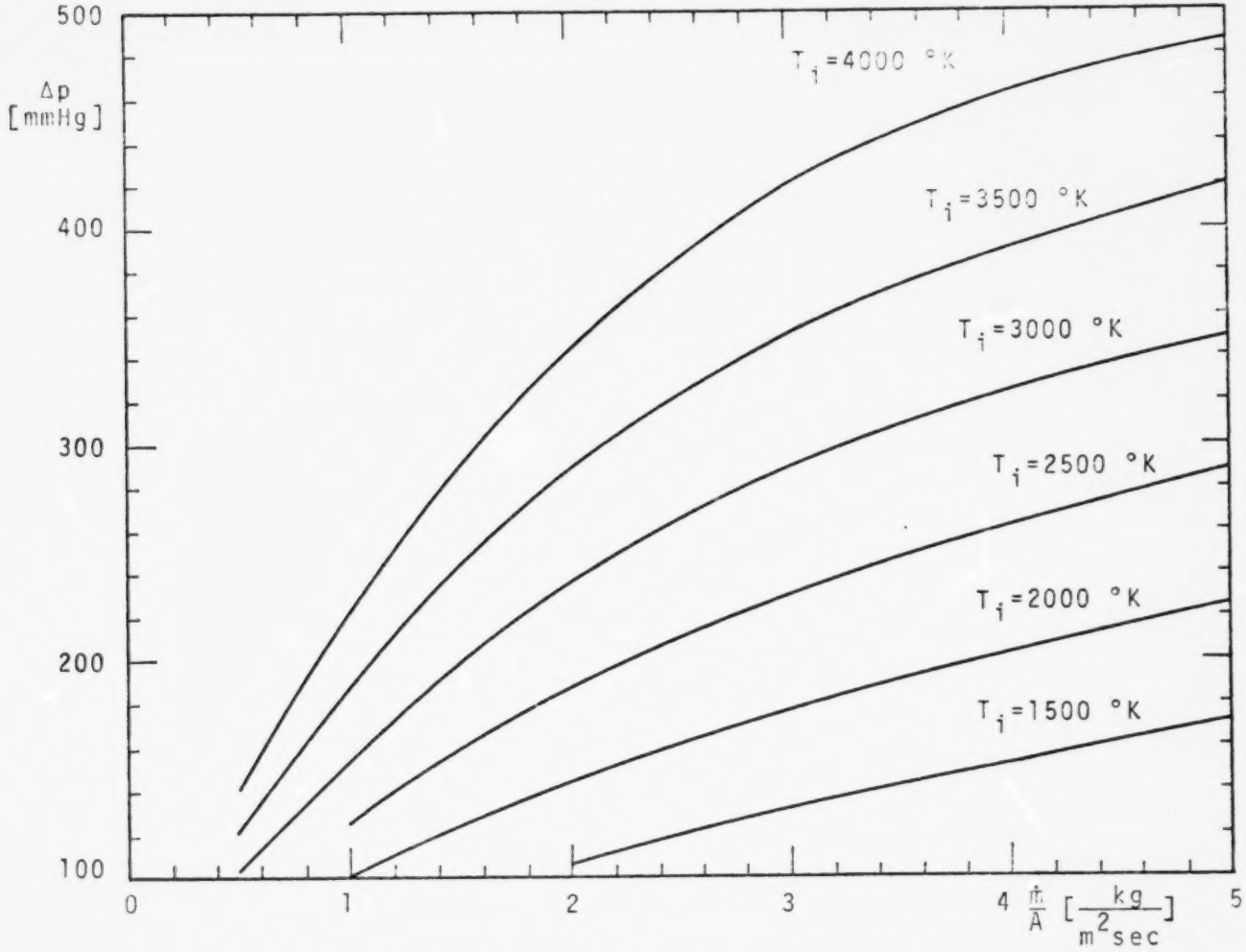

FIG. 14 TEMPERATURE OF POROUS SECTORS, INSIDE SURFACE AS A FUNCTION OF TRANSPIRING MASS FLOWRATE PER UNIT AREA AND PRESSURE DROP ACROSS THE SECTOR

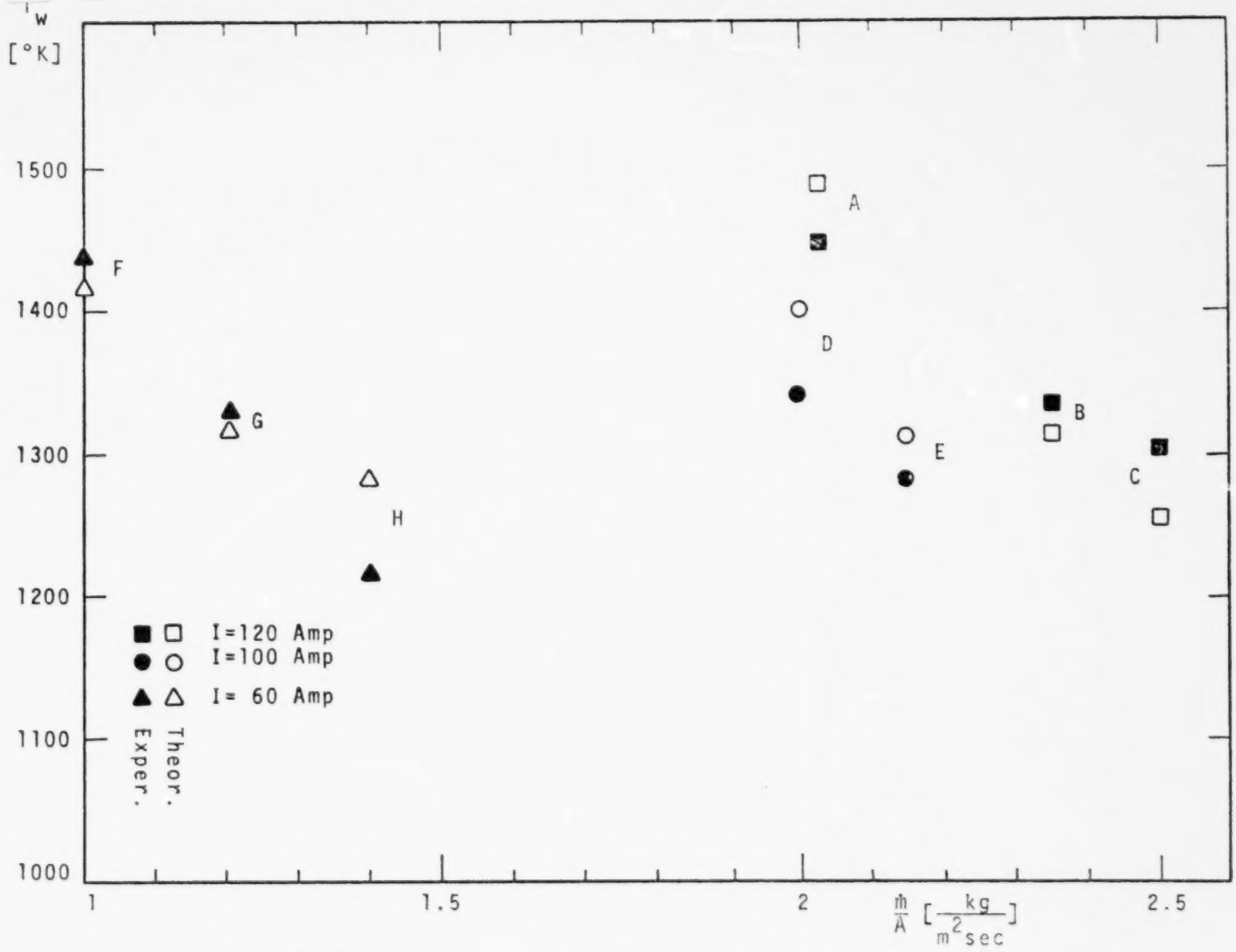

FIG. 15 COMPARISON OF THEORETICAL AND EXPERIMENTAL TEMPERATURE VALUES OF POROUS ANODE SECTORS OUTSIDE SURFACE

temperatures are higher than the theoretical predictions derived from Figure 13; and this difference between them increases with increasing mass flowrate, but as shown in Figures 16 to 18, these differences decrease with increasing current. The discrepancies between experimental and theoretical values and their trends with increasing mass flowrate and increasing arc current can be explained with the following arguments:

At low arc currents, the arc attachment area covers only a certain portion of the inside surface of a porous sector, leaving the outer regions of the surface relatively cooler. The temperature, therefore, is nonuniform over the surface and this nonuniformity persists throughout the porous material to the outer surface of the sector, due to its small thickness. The transpiring gas encounters a higher flow resistance in the high temperature region than in the cooler outer region of the porous sector. Since the plenum chamber pressure, which forces the gas through the porous sector, is uniform over the entire surface, a higher mass flowrate per unit area will flow through the outer region of the surface where the flow resistance is lower. The predicted temperatures, however, are based on the assumption of uniform temperature distribution; and, therefore, they represent the uniform temperature which would pertain to the sector in order for the mass flow and the pressure drop to assume the experimentally

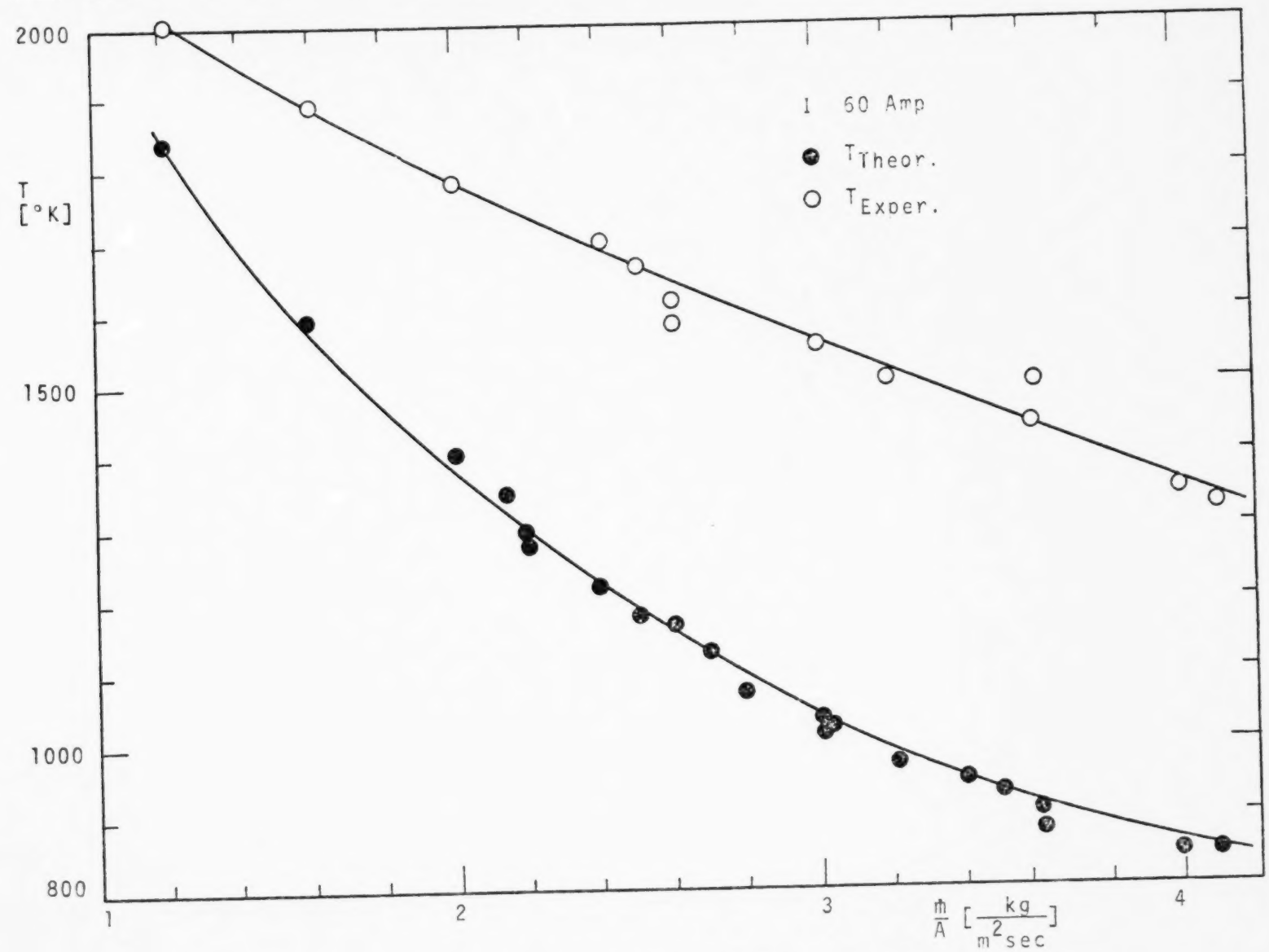

FIG. 16 COMPARISON OF THEORETICAL AND EXPERIMENTAL TEMPERATURE VALUES OF POROUS ANODE SECTORS

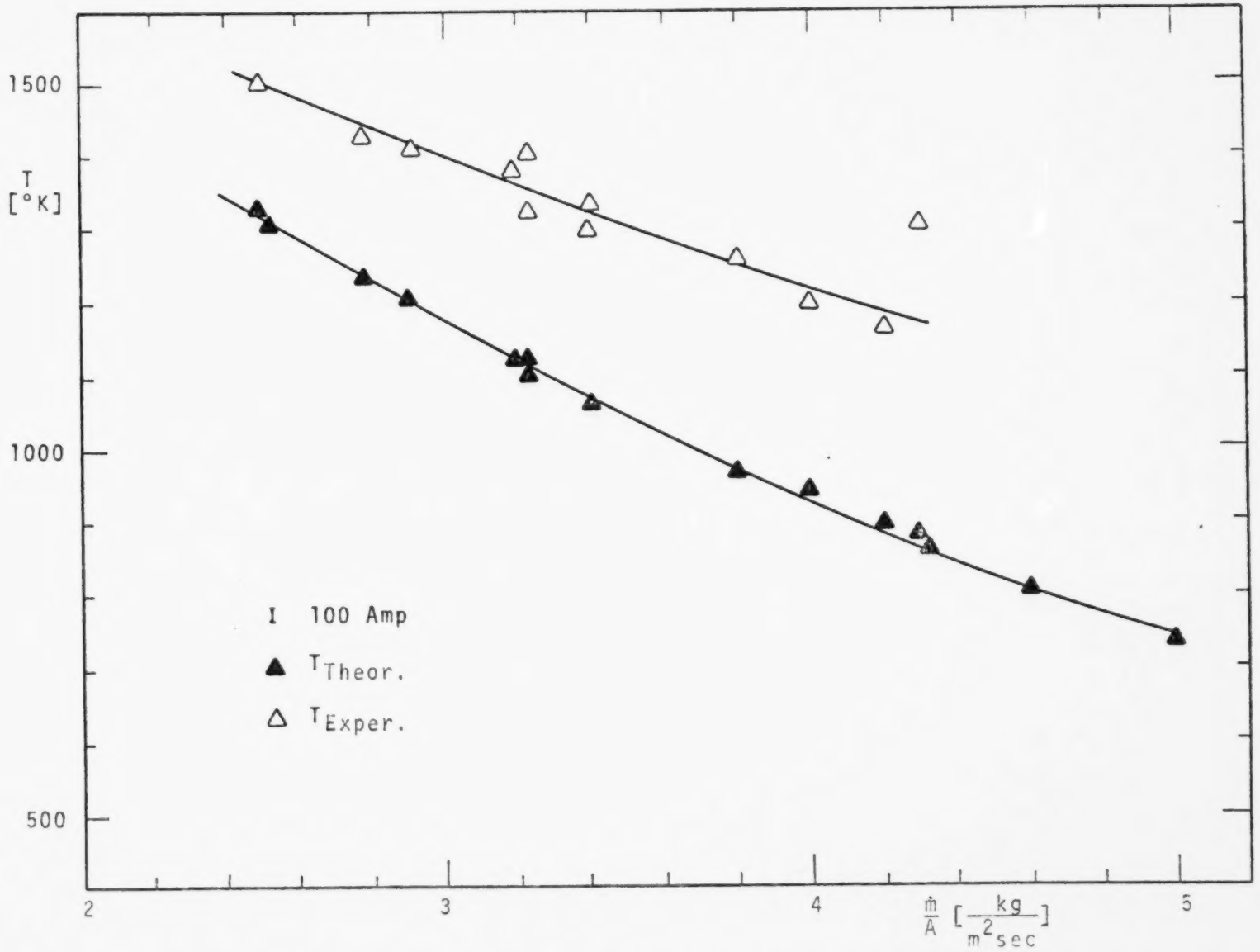

FIG. 17 COMPARISON OF THEORETICAL AND EXPERIMENTAL TEMPERATURE VALUES OF POROUS ANODE SECTORS

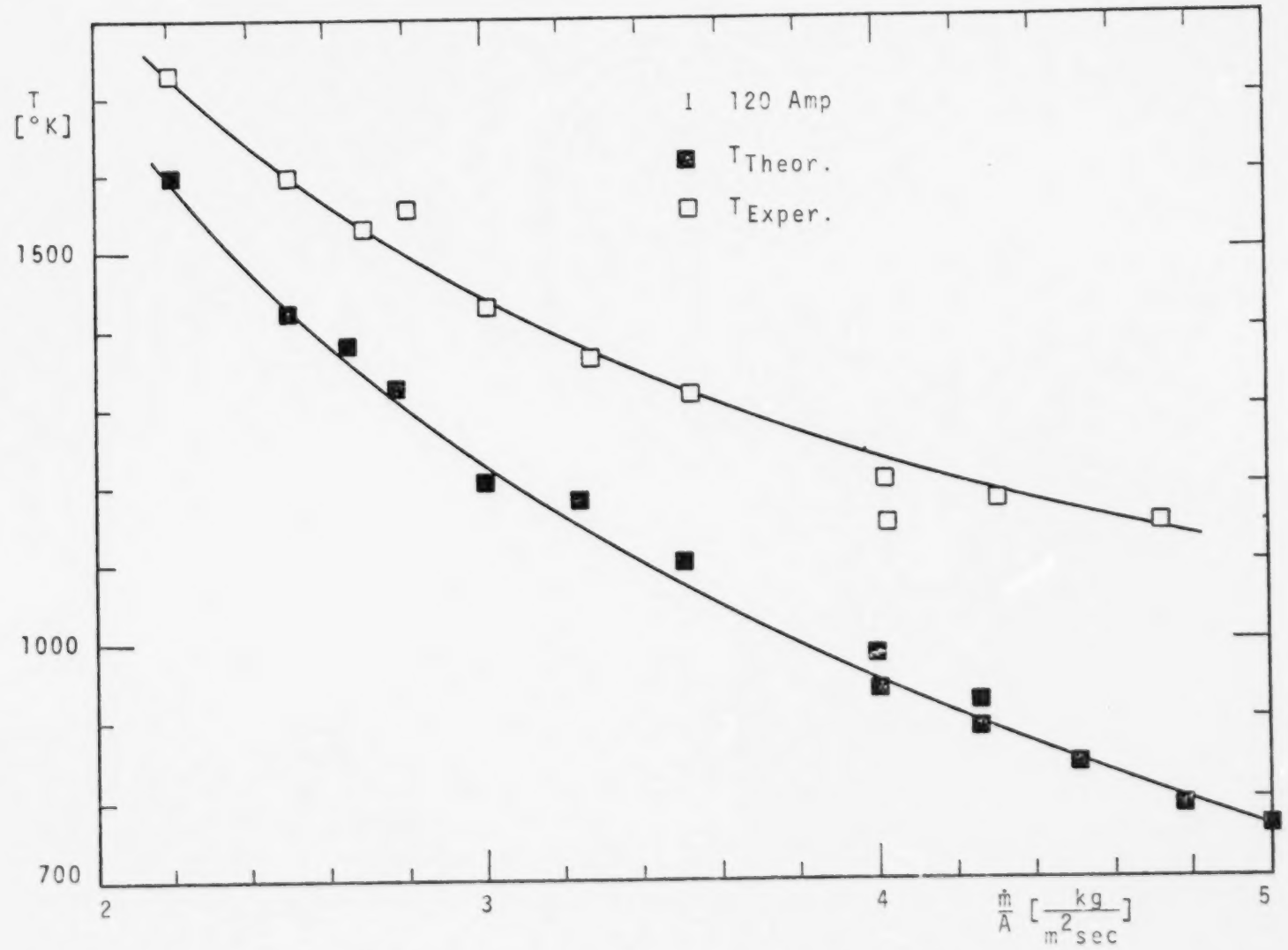

FIG. 18 COMPARISON OF THEORETICAL AND EXPERIMENTAL TEMPERATURE VALUES OF POROUS ANODE SECTORS

measured values. By means of the optical pyrometer, the temperature of the hotter glowing portion of the porous segment is measured which is obviously higher than the average temperature. When a higher transpiring argon mass flowrate is forced through the porous matrix by increasing the pressure in the corresponding plenum chamber, most of the added transpiring mass will flow through the outer cooler regions of the segment, thus enhancing the temperature difference between the central part of the segment surface and the surrounding part. On the other hand, when the current increases, the arc attachment size increases. Therefore, the high temperature region comprises a higher portion of the segment surface and the value of its "average" temperature approaches the temperature which is recorded by the pyrometer.

It should be pointed out that the above-described method, based on Figures 13 and 14 and requiring only pressure drop and mass flowrate measurements, yields incorrect surface temperature values when the temperature distribution on the outer surface is nonuniform. This is the case when the arc is attaching to the segment and the arc current values are small or the transpiring mass flowrate high. In this case, however, it is still possible to derive, from Figures 13 and 14, an accurate value of the temperature of the attachment spot on the inside surface of the porous anode, provided that the temperature of the corresponding glowing portion of the

outside surface is measured. In fact, this temperature and the measured pressure drop through the porous segment unequivocally determine the value of the argon mass flowrate per unit area, entering through the glowing zone of the outer surface and emerging through the arc attachment zone on the inner surface of the porous anode. The corresponding values can be derived graphically from Figure 13. Then, entering the diagrams of Figure 14 with this value of $\dot{m}/A$ and with the total pressure drop, the temperature of the attachment spot on the inner surface can be graphically derived. The above arguments imply that the flow through the porous matrix remains one-dimensional throughout the central regions of the sample.

E. Estimate of the Arc Attachment Size

From the difference in temperature between the central glowing portion of the outside porous surface and its average temperature pertaining to each arc run, the size of the arc attachment can be estimated.

For a given value of the pressure drop and transpiring mass flowrate through the segment where the arc attaches, the average temperature, T_w, of the outer surface of the porous segment is determined by means of Figure 13. The temperature, T_{wc}, of the central glowing region is measured by means of the optical pyrometer.

A two-step model is adopted to represent the temperature distribution on the surface. A central region of unknown area, A_c, is at a uniform high temperature, T_{wc}, surrounded by a region of unknown area, A_s, of an unknown uniform temperature, T_{ws}.

The following system of equations applies:

$$\left(\frac{\dot{m}}{A}\right)_{T_{wc}} A_c + \left(\frac{\dot{m}}{A}\right)_{T_{ws}} A_s = \dot{m} \tag{3.8}$$

$$A_c + A_s = A \tag{3.9}$$

$$T_{wc}\, A_c + T_{ws}\, A_s = T_w\, A \tag{3.10}$$

The symbol $\dot{m}$ represents the measured value of the total argon mass flow through the segment, whose total area is indicated by A; and $\left(\frac{\dot{m}}{A}\right)_{T_{wc}}$ and $\left(\frac{\dot{m}}{A}\right)_{T_{ws}}$ represent the mass flowrate per unit area in the regions at temperature T_{wc} and T_{ws}, respectively. These mass flowrates are functions of the temperature of the region and of the total pressure drop across the sample as indicated in Section III.D.1).

This system can be solved numerically by trial and error. The value of the temperature T_{wc} is measured and a value of the temperature T_{ws} is assumed; the corresponding values of $\left(\frac{\dot{m}}{A}\right)_{T_{wc}}$ and $\left(\frac{\dot{m}}{A}\right)_{T_{ws}}$ are determined from Figure 13

since the total pressure drop, Δp, is known. Then the two equations, (3.8) and (3.10), are solved for A_s and A_c: an improved value of T_{ws} is assumed and the iteration continues until the values of A_s and A_c derived from Equations (3.8) and (3.10) are in agreement. Due to the small thickness of the porous sector, it is assumed that the area, A_c, of the high temperature region remains constant throughout the sample and, therefore, represents the area of the arc attachment spot on the inner surface of the porous sector. The results are represented in Figure 19 where the estimated arc attachment area is plotted versus the mass flowrate transpiring per unit area of the porous sector and for values of the current of 60, 100, and 120 Amp.

The decrease of the arc attachment size with increasing mass flowrate is explained in [22] by the fact that the transpiring mass flowrate increases the convective heat losses from the arc. Since the arc current is kept constant, the arc shrinks according to the higher energy losses. The increase in arc attachment size with the arc current is due to the increase in arc diameter.

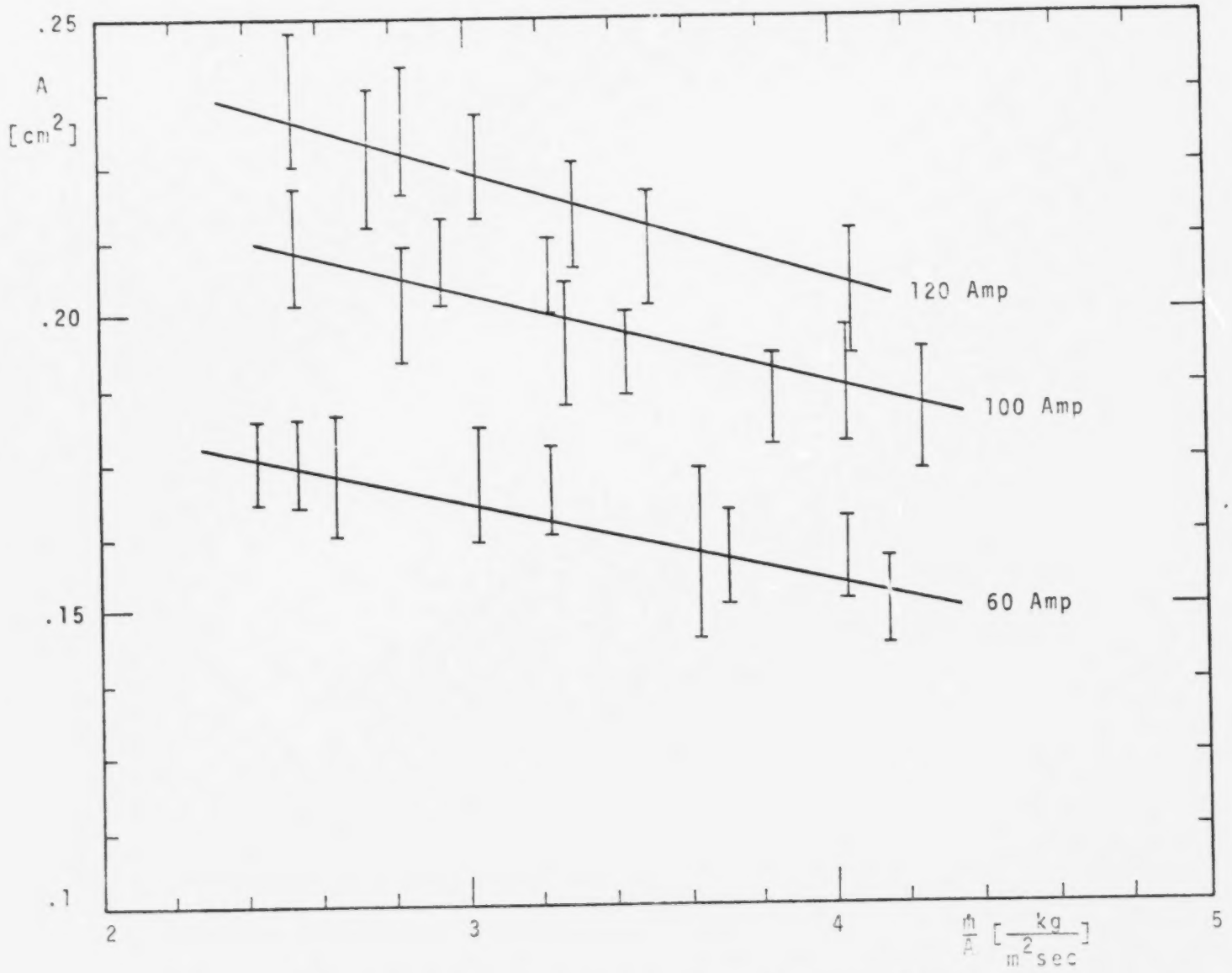

FIG. 19 ARC ATTACHMENT SIZE VERSUS MASS FLOWRATE PER UNIT AREA

IV. SIZE MEASUREMENTS OF ABLATED CARBON AEROSOL

A. Aerosol Sampling Technique

The aerosol size distribution measuring system is based on an electrical particle counter developed in the Particle Technology Lab, Mechanical Engineering Department, University of Minnesota [24-30]. The principle of its operation is based on the fact that the electrical mobility of a charged particle, i.e., the ratio of the particle velocity to the applied electric field acting on it, is a function of the particle size. In particular, for diffusion charged particles having a diameter smaller than 1 μm, the electrical mobility is a monotonically decreasing function of the particle size. Therefore, if such particles are introduced into a known flow field and electric field, i.e., into an electrostatic precipitator, their size can be determined from electrical mobility measurements.

A schematic of the electrostatic particle counter is shown in Figure 20 [29]. Entering aerosol is given a unipolar negative charge by a jet charger where the charging results from the fast mixing of uncharged particles with high concentration of negative ions generated by a corona needle. The charging mechanism is governed mainly by molecular diffusion so that the number of elementary charges on a particle leaving the charger is proportional to the particle diameter [25].

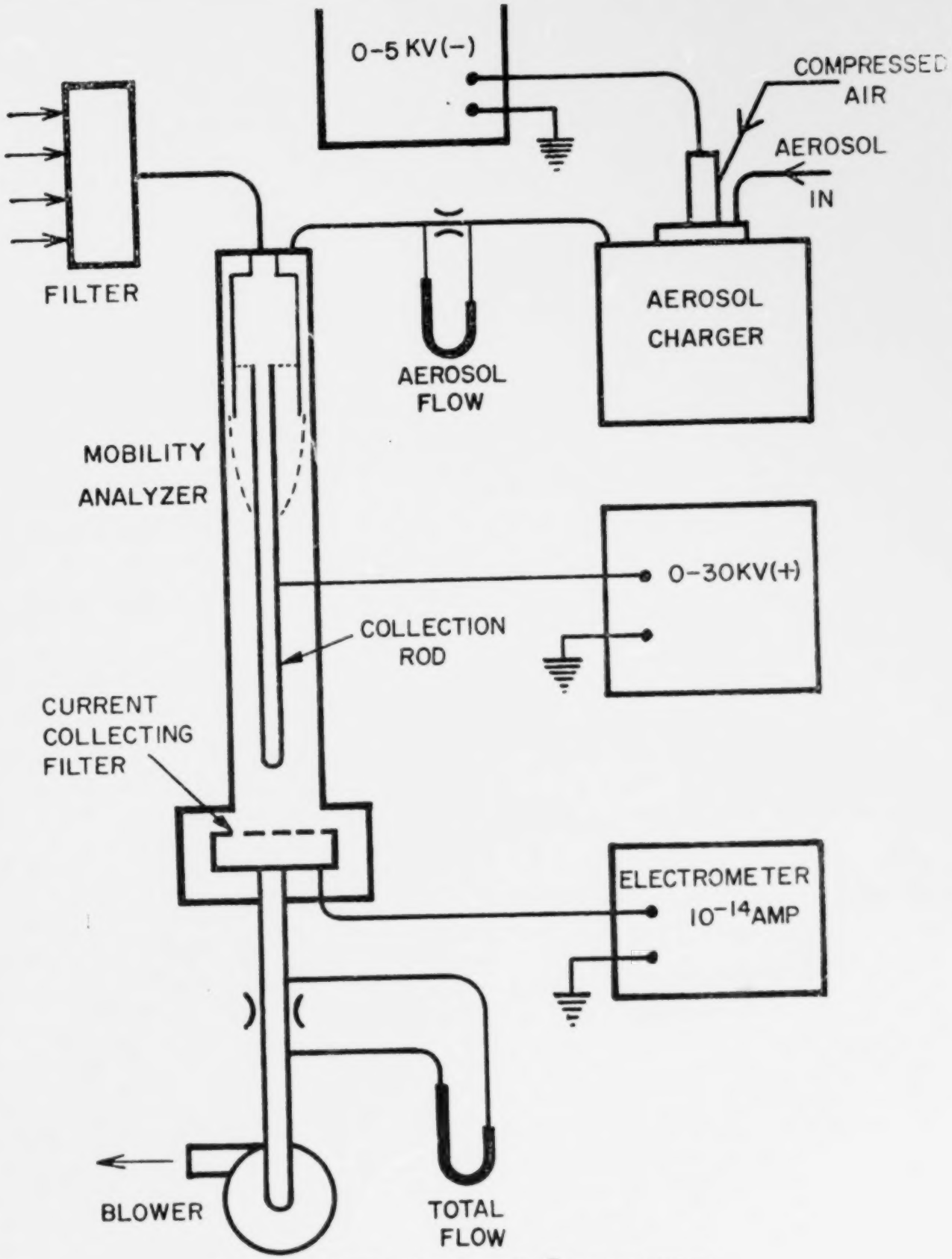

FIG. 20 SCHEMATIC OF THE ELECTROSTATIC PARTICLE COUNTER

The charged aerosol then passes through a flowmeter to the mobility analyzer. The aerosol enters the precipitating tube as a thin annular cylinder around a core of clean air. A metal rod located along the axis of the tube acts as aerosol collector. The collector voltage is systematically varied so that all the particles having a mobility less than a given value will miss the end of the collector rod and be collected by the current collecting absolute filter. The filter is electrically connected to an electrometer sensitive to 10^{-14} Amp which measures the total current due to the charges given up by the particles collected on the filter.

The values of the filter current can then be plotted as a function of the collector-rod voltage. From this curve the number particle size distribution of the aerosol may be calculated. Special calibration of the instrument has been performed [30] for particle sizes smaller than 0.03 μm, that is, for the size range of the ablated particles generated by the plasma torch.

The auxiliary equipment includes a vacuum pump, a clean air box, and a 3 m^3 volume plastic bag in which the aerosol, diluted in the box, is stored for the time necessary to perform the electrical particle counter measurements. High voltage power supplies, needed for the jet charger and for the electrostatic precipitator, are located, together with flowrators and control valves, in a mobile console independent from the particle counter.

B. Experimental Procedure and Results

Size distribution analysis is performed on the generated aerosol particles obtained from the transpiration-cooled anode plasma torch. For each arc run, the values of the parameters characterizing the plasma torch operation are determined and the corresponding aerosol particles, ablated from the anode surface, are sampled following the above-described procedure.

The experiments are performed at arc currents of 60 and 120 Amp and for transpiring mass flowrates ranging from about 1 to 5 Kg/m^2sec through the sector on which the arc is attaching. For each run, the total pressure drop and the transpiring mass flowrate are measured simultaneously with the temperature of the glowing region of the porous segment outer surface. The latter is determined by means of a calibrated optical pyrometer. In Figure 21, the experimentally determined values of the pressure drop across the porous segment versus the mass flowrate per unit area are plotted and consecutively numbered from 1 to 11. The temperatures of the glowing region of the outer surface are also indicated. Each data point represents a mean value averaged over several measurements ranging from 5 to 17. For identical operating conditions of the torch, several runs are performed in order to check the reproducibility of the data and for obtaining an estimate of the experimental error. The area enclosed in the symbols in

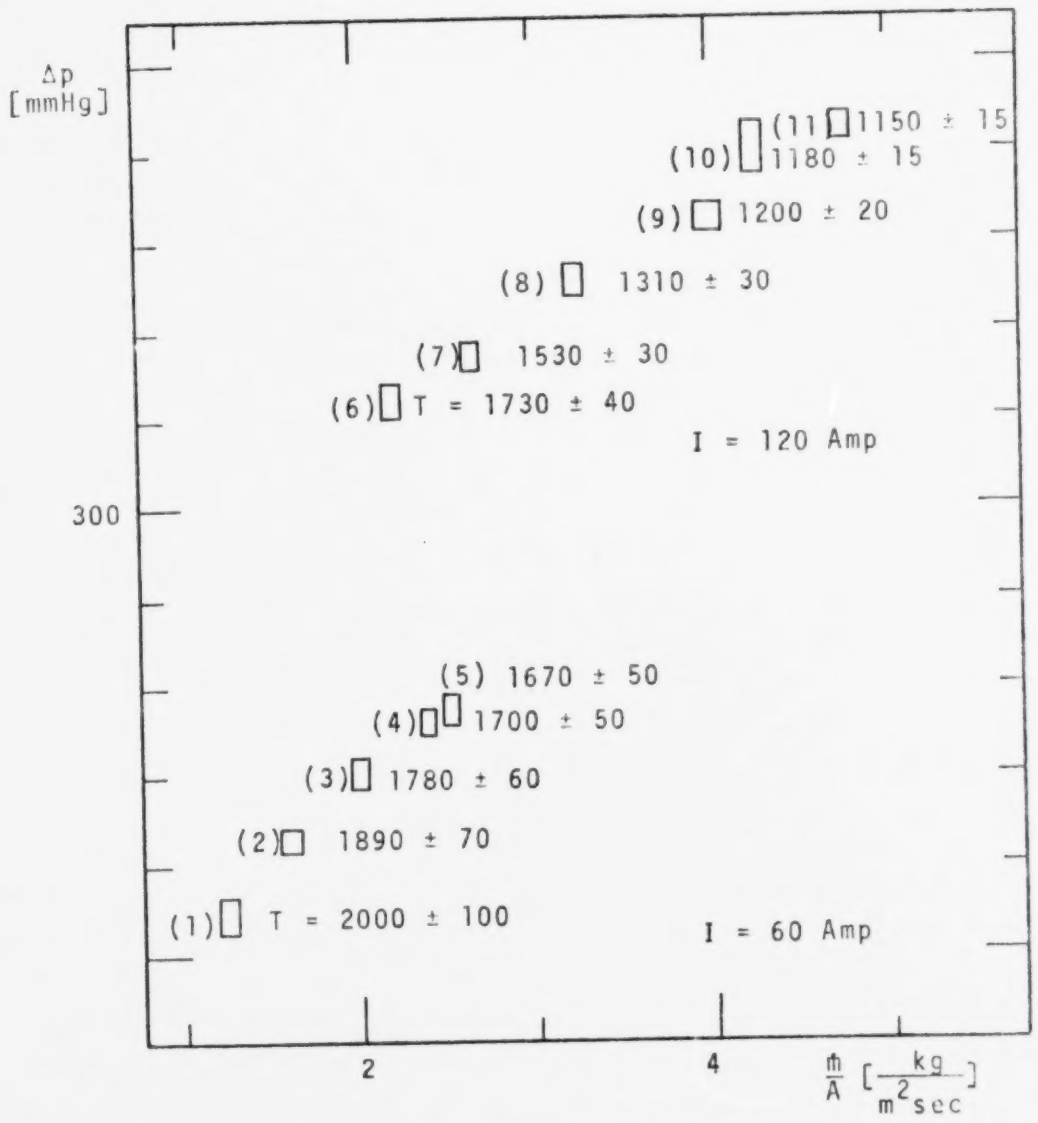

FIG. 21 ABLATION TESTS: POROUS SEGMENT CHARACTERISTIC PARAMETERS

Figure 21 indicates the scatter of the experimental data. The data scatter for the temperature indicated in the same figure is derived in a similar manner.

For a check of the consistency of the pressure and mass flowrate data, a comparison is made with corresponding data obtained in previous experiments for the same arc current and which are, in part, represented in Figures 7 to 10. The results of this comparison are shown in Figure 22: the asterisk indicates the points taken from Figure 21 and the circles the points reported, in part, in Figures 7 to 10. The points referring to the same arc current can be correlated by the same curve; and the data scatter, with respect to this curve, is in the order of a few percent.

The temperatures indicated in Figure 21 are also compared with those of previous experiments reported in Figures 16 and 18. The results are shown in Figure 23 where the asterisks denote the data from Figure 21 and the circles the data from Figures 16 and 18. Again, all the data referring to the same arc current can be correlated by the same curve; and the data scatter, with respect to this curve, is again in the order of a few percent.

The temperature of the arc attachment area on the inside surface of the porous anode where the ablated aerosol is generated is then determined for each set of data consisting of pressure drop, mass flowrate per unit area, and temperature

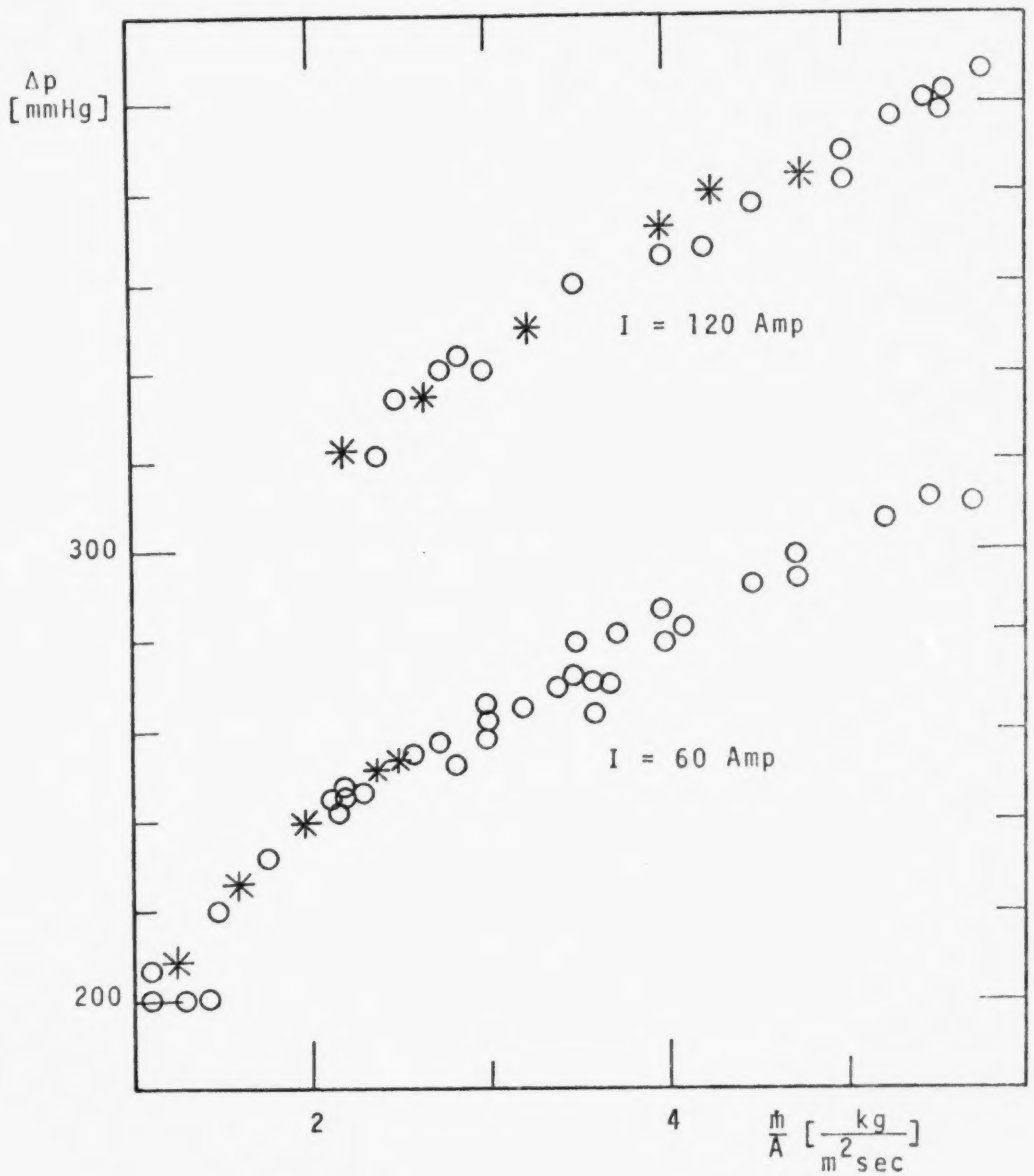

FIG. 22 ABLATION TESTS: COMPARISON OF FLOW CHARACTERISTICS THROUGH POROUS ANODE SEGMENT

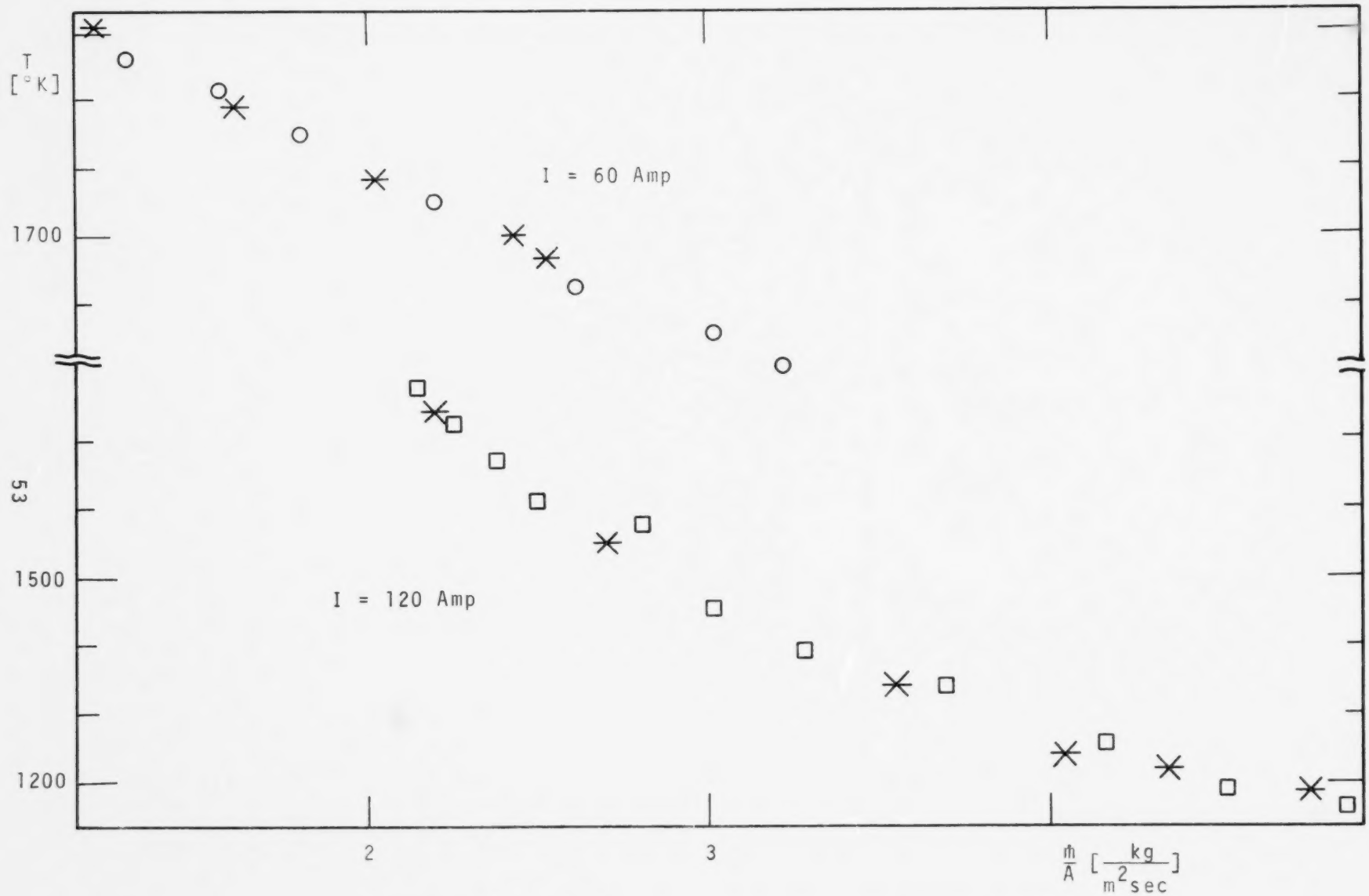

FIG. 23 ABLATION TESTS: COMPARISON OF POROUS ANODE SEGMENT OUTSIDE SURFACE TEMPERATURE

of the glowing region of the porous segments outside surface (indicated in Figure 21). Due to the nonuniform temperature distribution on the porous segment surface, the procedure as outlined in Section III.D.2) has to be followed.

From Figure 13, for each value of the pressure drop and the outside wall temperature, the mass flowrate per unit area $(\dot{m}/A)_{ATT}$ flowing through the hot region of the porous segment can be graphically determined. Entering Figure 14 with this value of $(\dot{m}/A)_{ATT}$ and with the same value of the pressure drop, the temperature of the arc attachment area on the inner surface of the porous anode may be graphically determined. The results are shown in Figure 24 where the temperature of the attachment area is plotted versus the argon mass flowrate transpiring through it per unit area. The numbers attached to the symbols serve for cross reference with Figure 21. The runs at 120 Amp and 60 Amp cover the same range of attachment area temperatures, and the corresponding ranges of argon mass flowrates per unit area nearly overlap for $(\dot{m}/A)_{ATT} \simeq 2$ Kg/m^{2}sec.

The size distribution of the aerosol generated in each run is determined and the results are shown in Figures 25 and 26. The cumulative size distribution is plotted on log probability plots for arc currents of 60 and 120 Amp, respectively. The number characterizing each plot refers to the corresponding data points, pertaining to torch operation, represented in Figures 21 and 24.

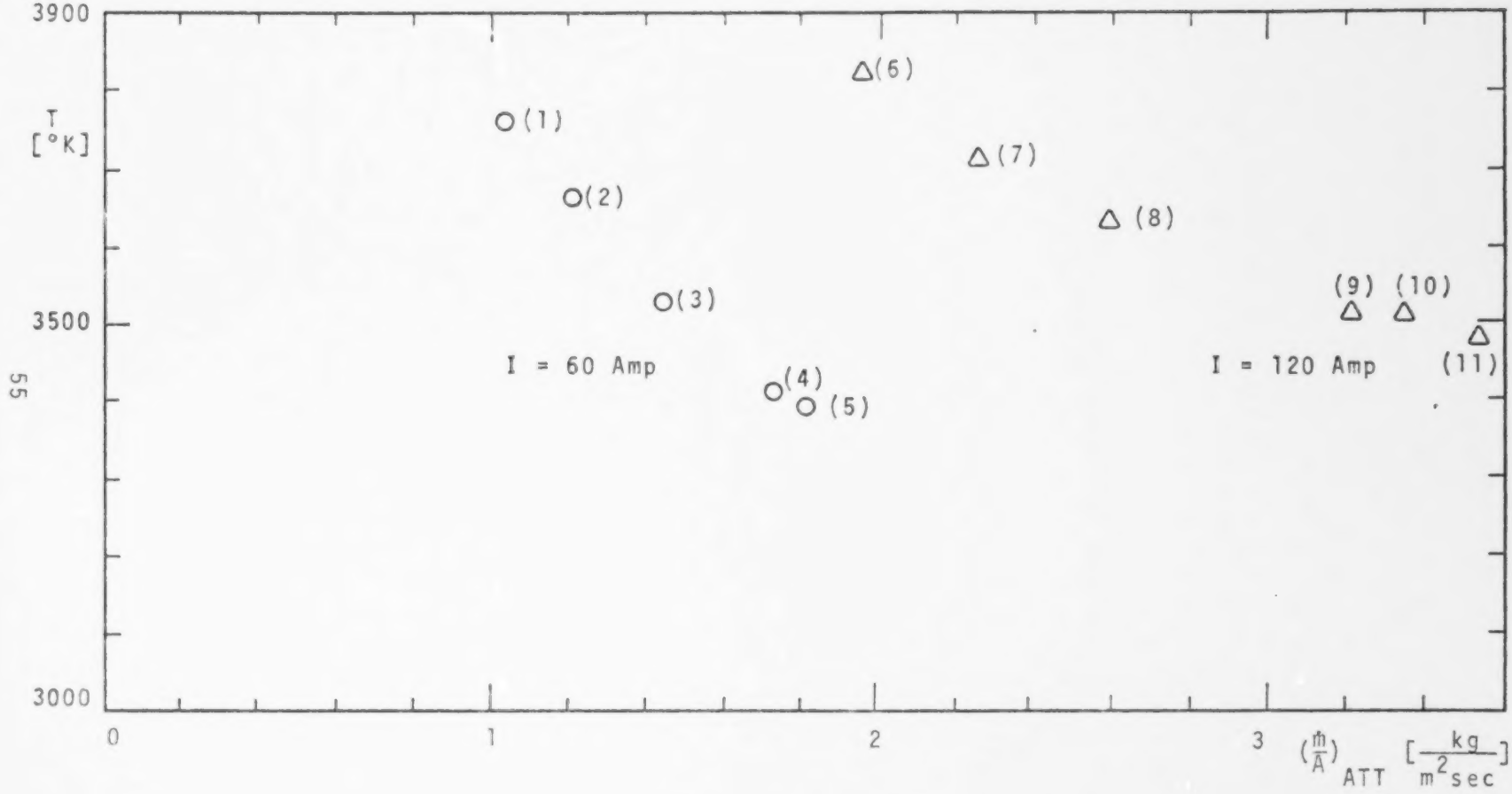

FIG. 24 ABLATING SURFACE TEMPERATURE VERSUS TRANSPIRING MASS FLOWRATE PER UNIT AREA

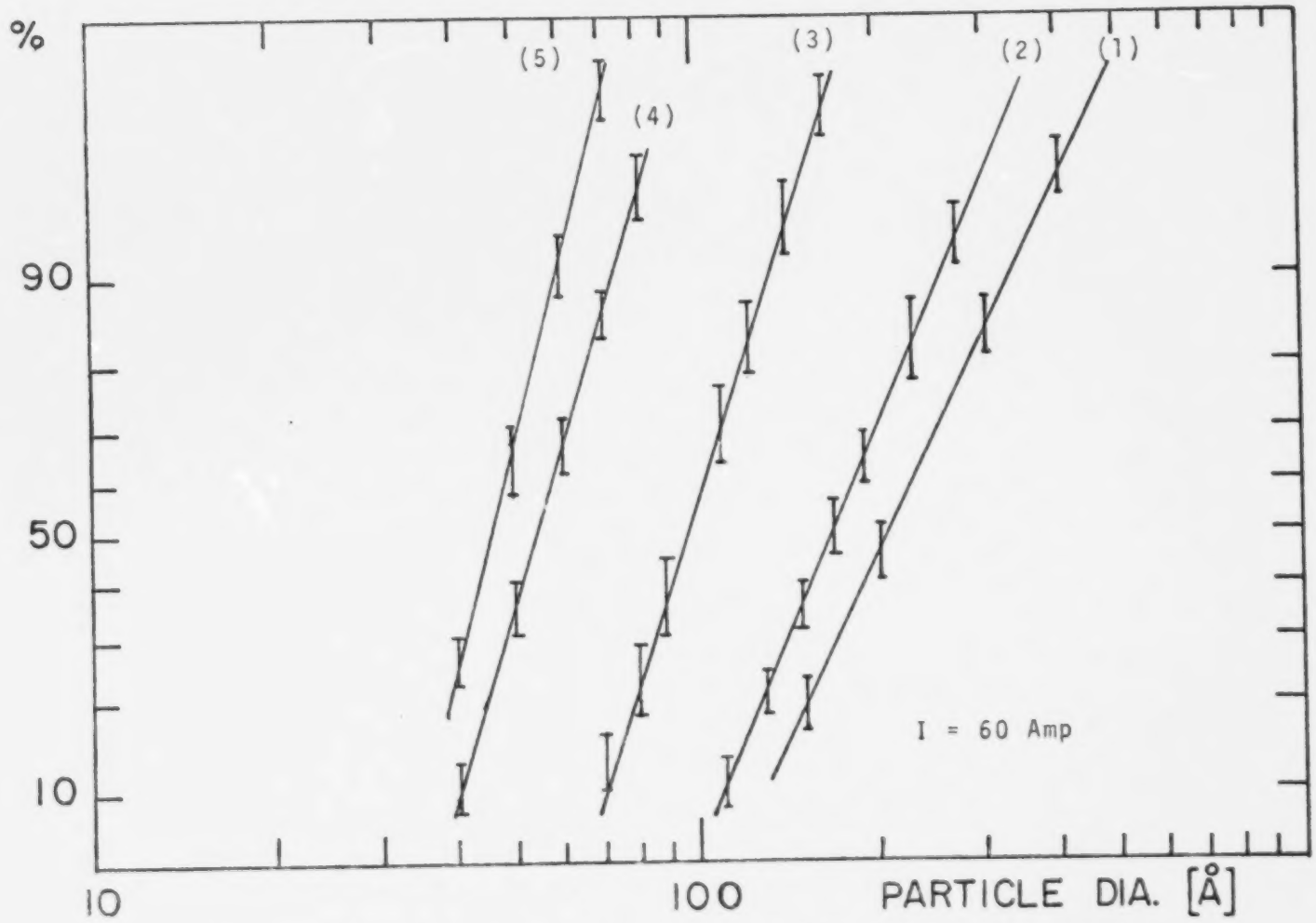

FIG. 25 CUMULATIVE SIZE DISTRIBUTIONS OF ABLATED PARTICLES

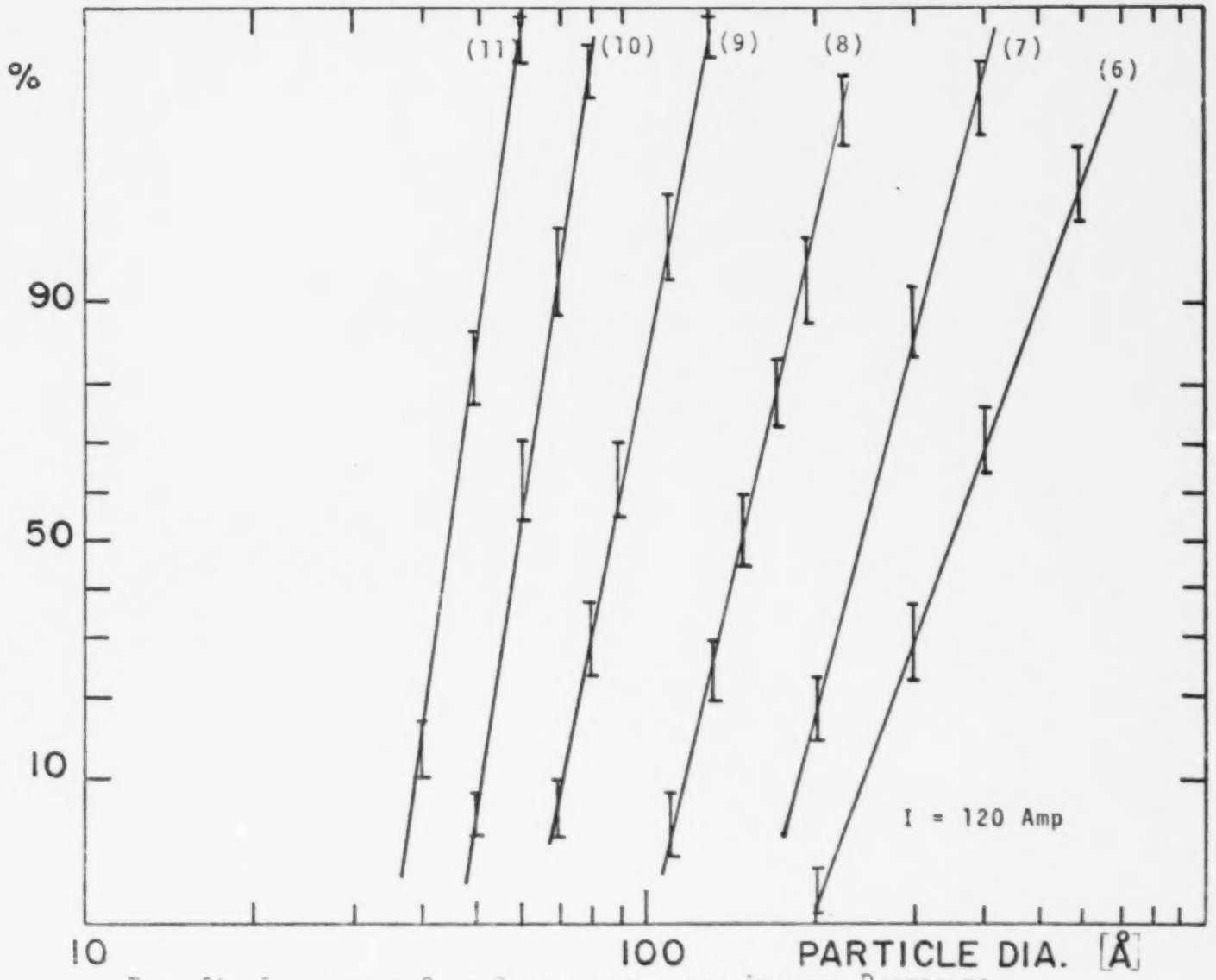

FIG. 25 CUMULATIVE SIZE DISTRIBUTIONS OF ABLATED PARTICLES

The values of the average diameter and of the logarithmic standard deviation are then derived from Figures 25 and 26 for each particle size distribution represented in these figures. In Figures 27 and 28, the average diameter of the aerosol particles is plotted versus the argon mass flowrate transpiring through the arc attachment area and versus the temperature of this area, respectively, for arc currents of 60 and 120 Amp.

In Figures 29 and 30, the logarithmic standard deviation, characterizing each aerosol size distribution, is represented as a function of the mass flowrate per unit area of the attachment spot and of the attachment spot temperature, respectively.

From Figures 27 to 30, by crossplotting, the logarithmic standard deviation can be derived as a function of the average particle diameter: the results are shown in Figure 31. The size spectra for each of the arc operating conditions is represented in Figures 32 and 33 for arc currents of 60 and 120 Amp, respectively.

For each size distribution, the maximum value within the spectral particle number density is derived from Figures 32 and 33. The particle number density is related to the ablation temperature, i.e., the attachment spot temperature by the Clausius Clapeyron equation:

$$\ln n = A_1 - A_2 \frac{1}{T_{ATT}} - \ln T_{ATT} \qquad (4.1)$$

where A_1 and A_2 are constants. This equation indicates, for small variations of T, a quasi-linear dependence of ln n on $\frac{1}{T}$. The maximum value of the spectral particle number density, derived from Figures 32 and 33, is then plotted on a semilogarithmic diagram versus $\frac{1}{T}$, where T is the corresponding temperature of the arc attachment spot. The results are shown in Figure 34.

C. Conclusions

On the basis of the above-mentioned experimental results, the relationships among the plasma torch operating parameters and the parameters characterizing the produced aerosol can be found and explained. The arc current and the cooling argon mass flowrate per unit area, flowing through the arc attachment spot, can be directly related to the mean particle diameter and the logarithmic standard deviation of the aerosol ablated from the arc attachment area.

Figures 27 and 28 show that the mean particle diameter increases with the temperature of the arc attachment and decreases with increasing transpiring mass flowrate per unit area flowing through the attachment spot.

These findings can be qualitatively explained. The ablation rate from the anode surface increases with the surface temperature. Consequently, the number density of

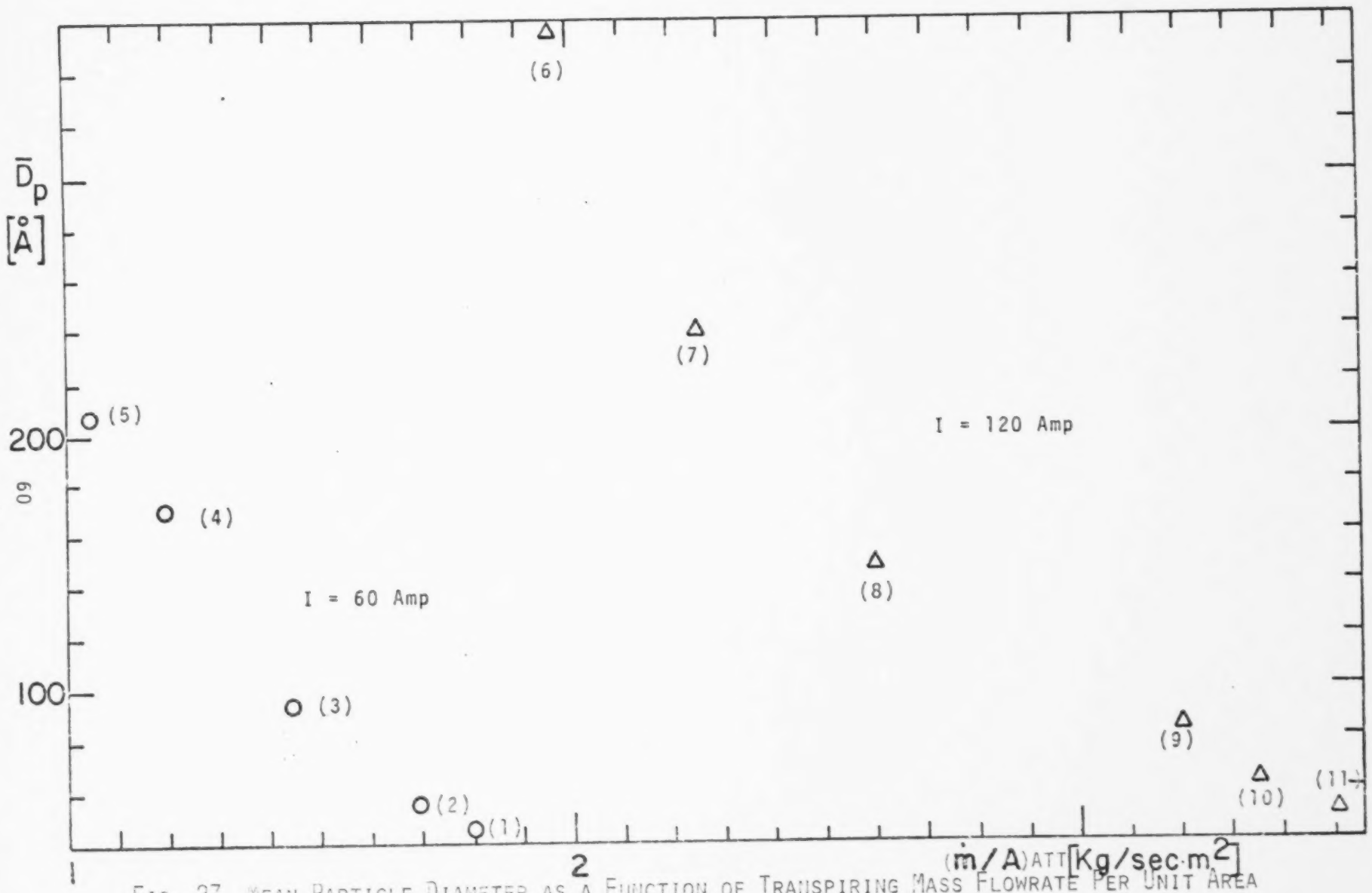

FIG. 27 MEAN PARTICLE DIAMETER AS A FUNCTION OF TRANSPIRING MASS FLOWRATE PER UNIT AREA

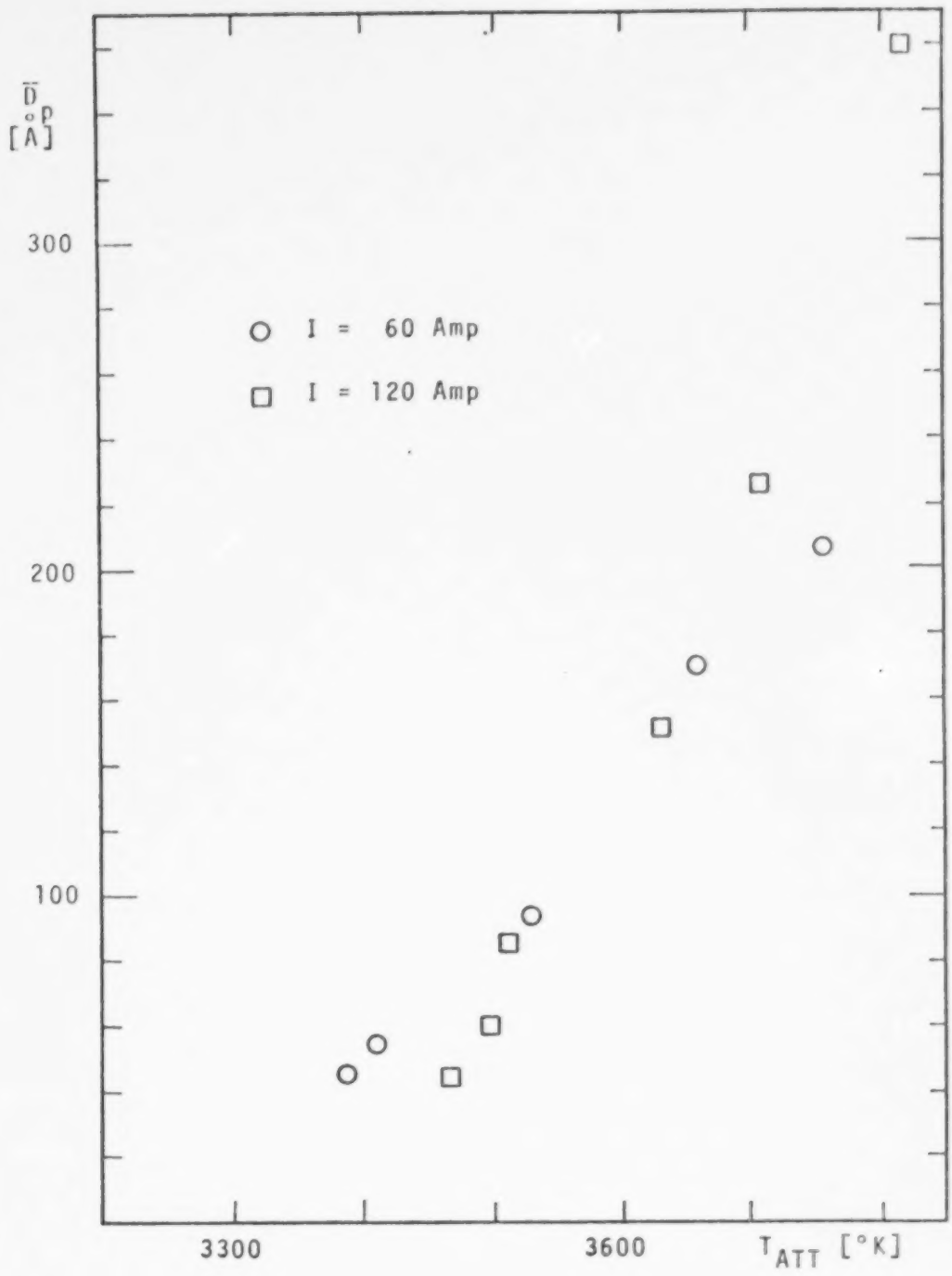

FIG. 28 MEAN PARTICLE DIAMETER AS A FUNCTION OF ABLATING SURFACE TEMPERATURE

carbon particles near the anode surface increases, yielding higher coagulation rates and, therefore, larger size particles. The decrease in particle diameter with increasing transpiring mass flowrate per unit area is due to two reasons. By increasing the transpiring mass flowrate, the temperature of the arc attachment spot and the associated rate of ablation at the anode surface decreases, yielding smaller particle diameters as explained above. At the same time, an increase in transpiring mass flowrate enhances the dilution of the ablated particles in front of the anode, thus decreasing the coagulation rate and, consequently, the particle size.

The data presented in Figure 28 show that the mean particle diameters corresponding to an arc current of 60 Amp become smaller with increasing arc attachment temperature than those corresponding to 120 Amp. At lower currents, the required transpiring mass flowrate and the associated particle dilution are smaller than at higher arc currents, postulating the same arc attachment temperature in both cases. This should yield larger particle diameters at lower currents only on account of the smaller mass flowrate. Therefore, the results of Figure 28 seem to be inconsistent; however, an explanation for this apparent inconsistency exists and will be given later.

Figure 29 shows that the logarithmic standard deviation, characterizing the ablated aerosol size distribution, is a

decreasing function of the transpiring mass flowrate per unit area flowing through the attachment spot. It is speculated that the gas transpiring through the ablating surface, besides influencing the temperature, has a quenching effect on the particles immediately after they are produced, preventing them from further coagulation. The higher the gas flowrate, the smaller the number of particles which can undergo coagulation over an extended time period and randomly increase their size, resulting in a wider size distribution.

Figure 30 shows that for a given temperature of the ablating surface, the standard deviation corresponding to an arc current of 60 Amp is larger than the one corresponding to 120 Amp. This is due to the fact that the required mass flowrate corresponding to a given temperature of the attachment area is smaller at lower arc currents, yielding larger standard deviations as explained above. Another reason for the increase of the standard deviation at lower arc currents hinges on the dependence of the size of the arc attachment area on the arc current. In Section III.E., it was shown that the size of the attachment spot is an increasing function of the arc current. The temperature over the attachment area may be assumed to be rather uniform in the central region while in the outer region it decreases because of conduction losses to the cooler zones surrounding the attachment area. Therefore, not all the particles ablate from the central

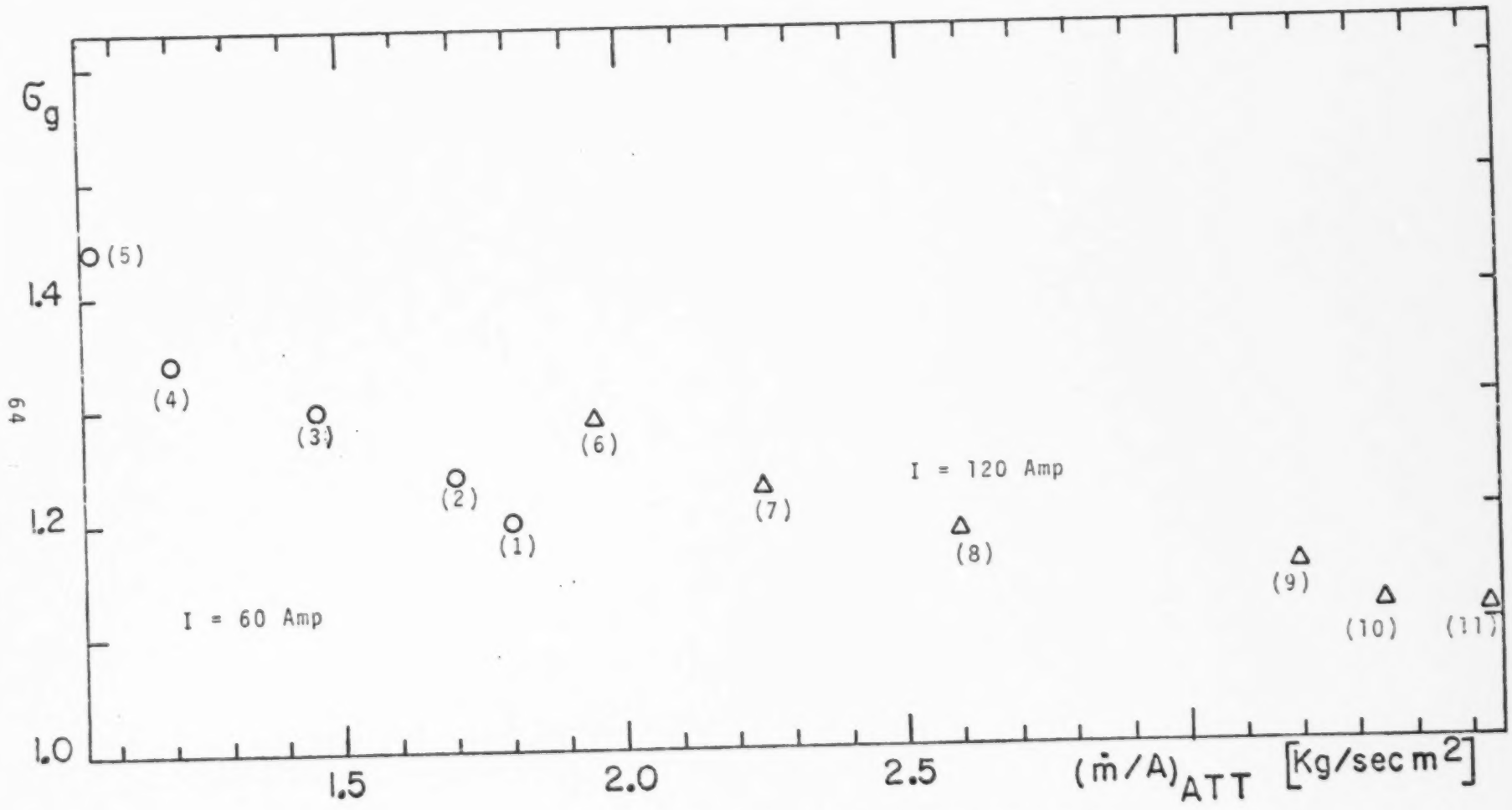

FIG. 29 LOGARITHMIC STANDARD DEVIATION VERSUS TRANSPIRING MASS FLOWRATE PER UNIT AREA

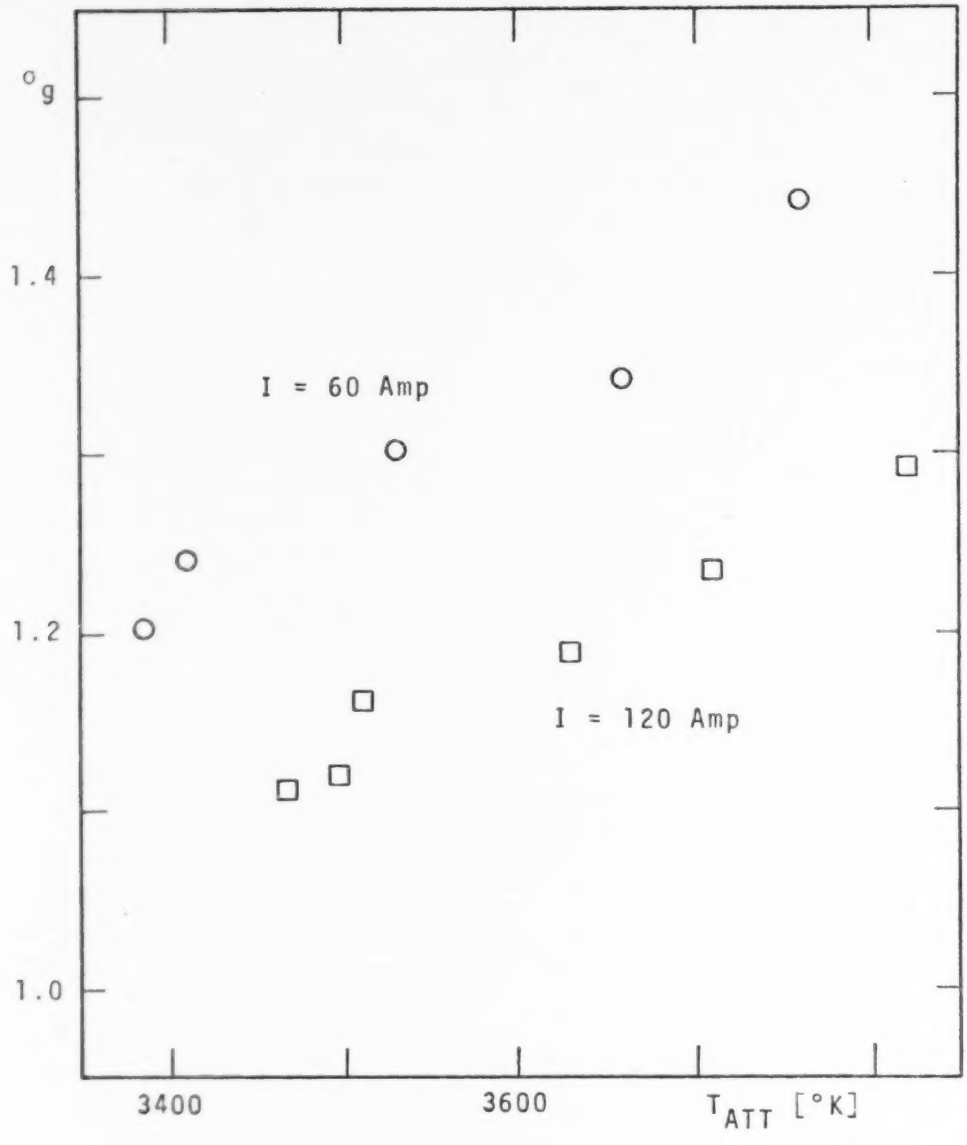

FIG. 30 LOGARITHMIC STANDARD DEVIATION VERSUS ABLATING SURFACE TEMPERATURE

region at constant temperature; but a fraction is also generated in the outer regions at lower temperature, yielding smaller particle diameters. When the arc current and, therefore, the size of the attachment decreases, the outer region with a nonuniform temperature distribution becomes a larger fraction of the total attachment area, generating a number of smaller particles and hence producing a wider spread of the standard deviation which characterizes the ablated aerosol size distribution.

In this way, it can also be explained why the data represented in Figure 28 seem to be inconsistent, because the average diameter plotted in Figure 28 is associated with the uniform temperature of the central region of the arc attachment area and not with an average temperature. For arc currents of 120 Amp, this temperature is representative for the entire surface; the area of the outer region with a lower temperature and a nonuniform temperature distribution is negligible with respect to the total arc attachment area. The number of particles generated in the outer colder region is accordingly small leading to the observed narrow standard deviation. On the other hand, for arc currents of 60 Amp, the outer colder region of the arc attachment spot is, as mentioned before, a substantial fraction of the total area. Therefore, a sizable fraction of the particles, with correspondingly smaller diameters, is generated from this colder portion

of the arc attachment area which is reflected by a relatively wide spread of the observed standard deviation. The temperature of the central region of the arc attachment spot, which is considered in Figure 28, is actually not representative for the true average temperature of the ablating surface; it is substantially higher than this average value. Hence, for an arc current of 60 Amp, the mean value of the particle diameter, plotted against the temperature of the central region of the arc attachment, appears lower than it should be if the true average temperature of the ablating surface would be applied. This discrepancy tends to decrease when the arc attachment temperature decreases because the conduction losses at the contours of the attachment area become less important, resulting in a more uniform temperature distribution over the entire ablating surface. This argument is consistent with the experimental finding that the standard deviation decreases with decreasing temperature of the ablating surface.

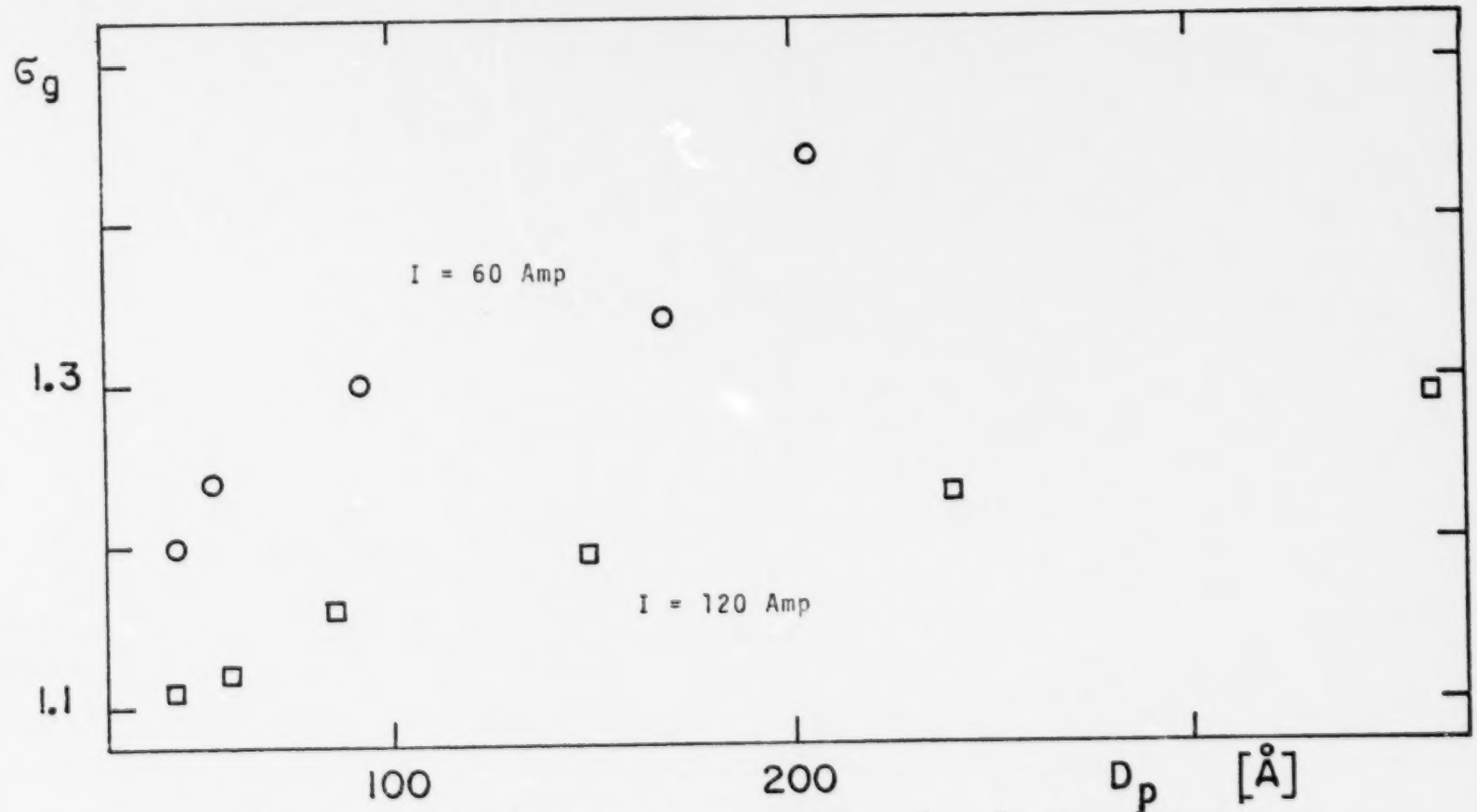

FIG. 31 LOGARITHMIC STANDARD DEVIATION VERSUS MEAN PARTICLE DIAMETER

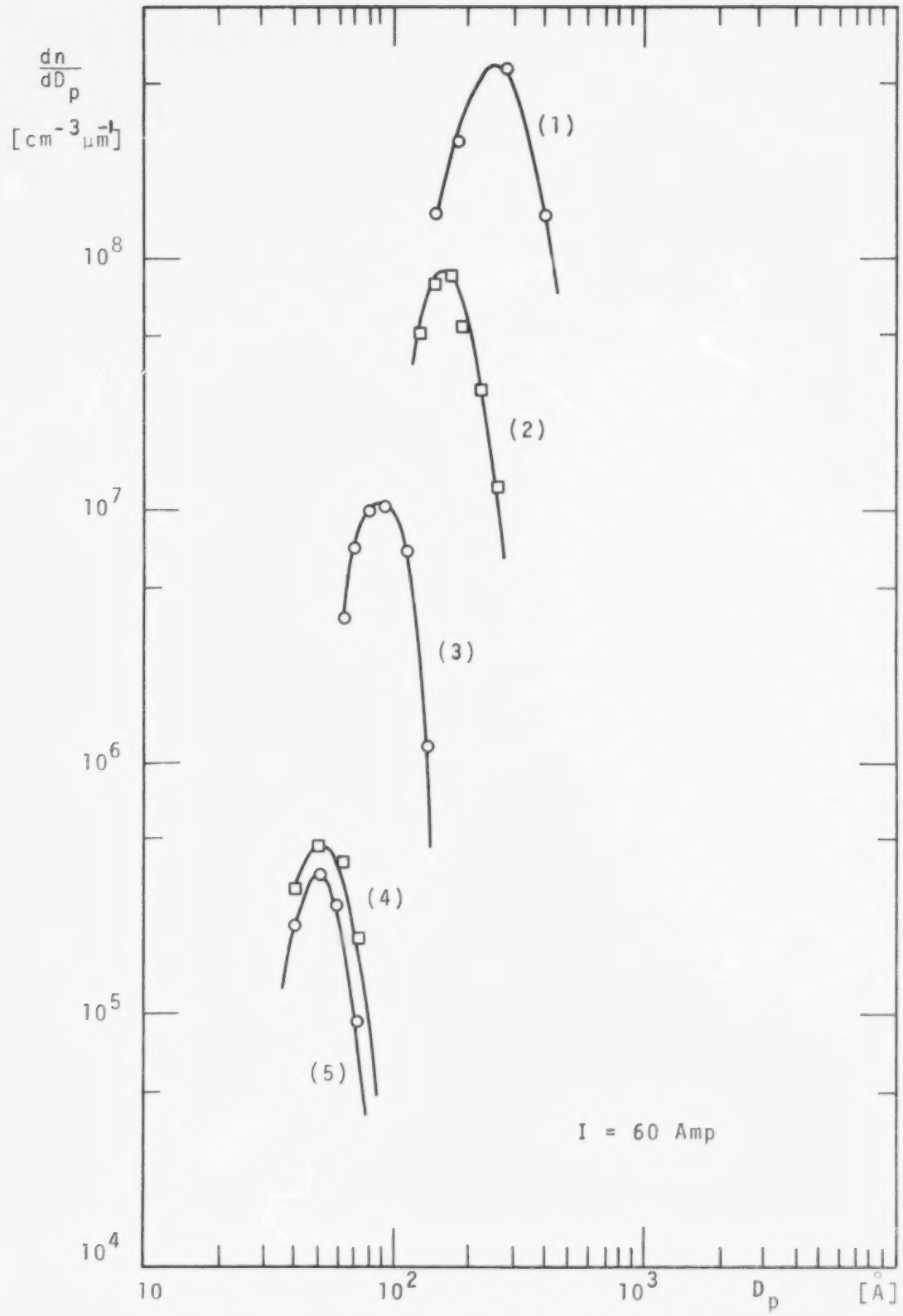

FIG. 32 ABLATED AEROSOL SIZE DISTRIBUTION

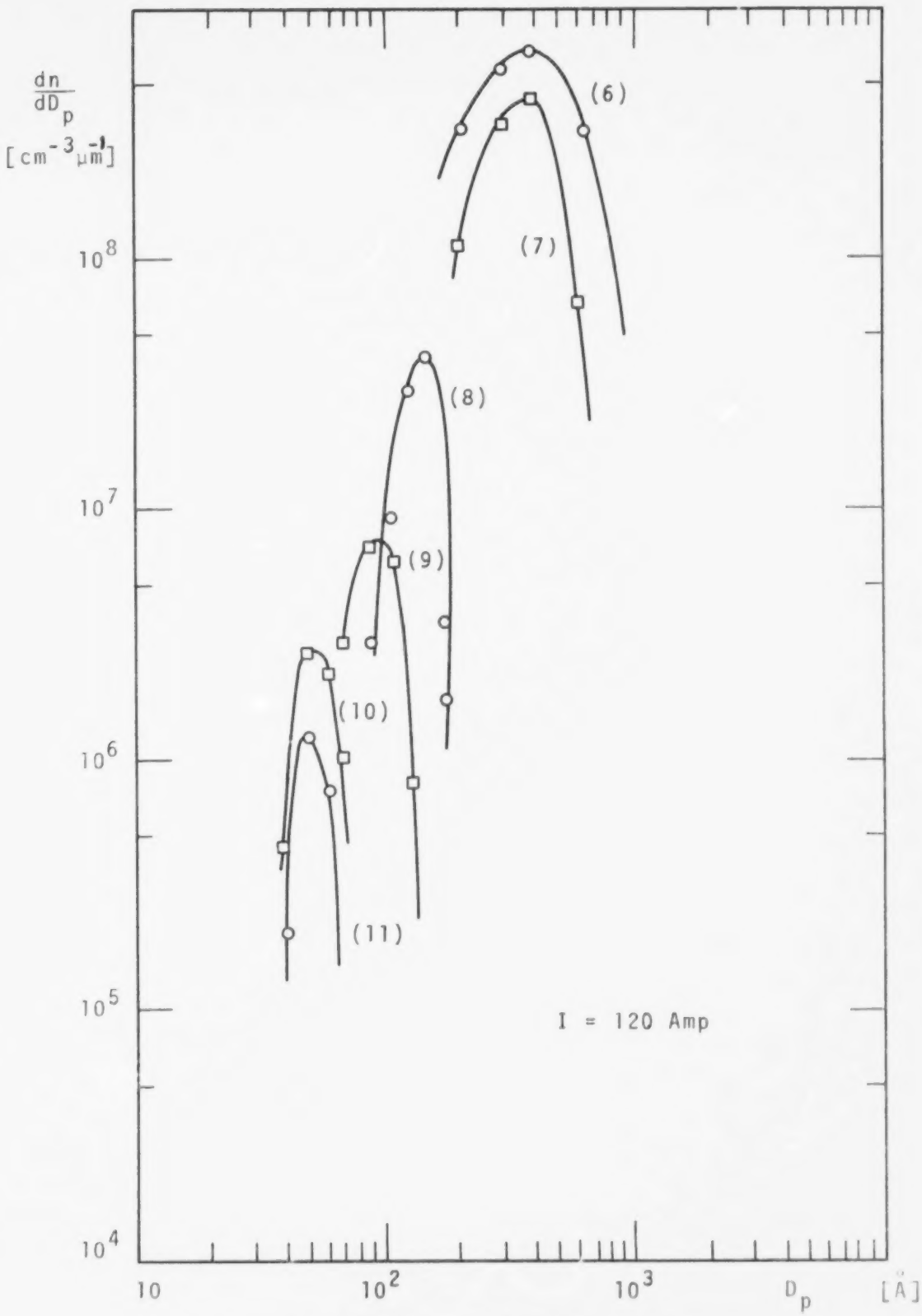

FIG. 33 ABLATED AEROSOL SIZE DISTRIBUTION

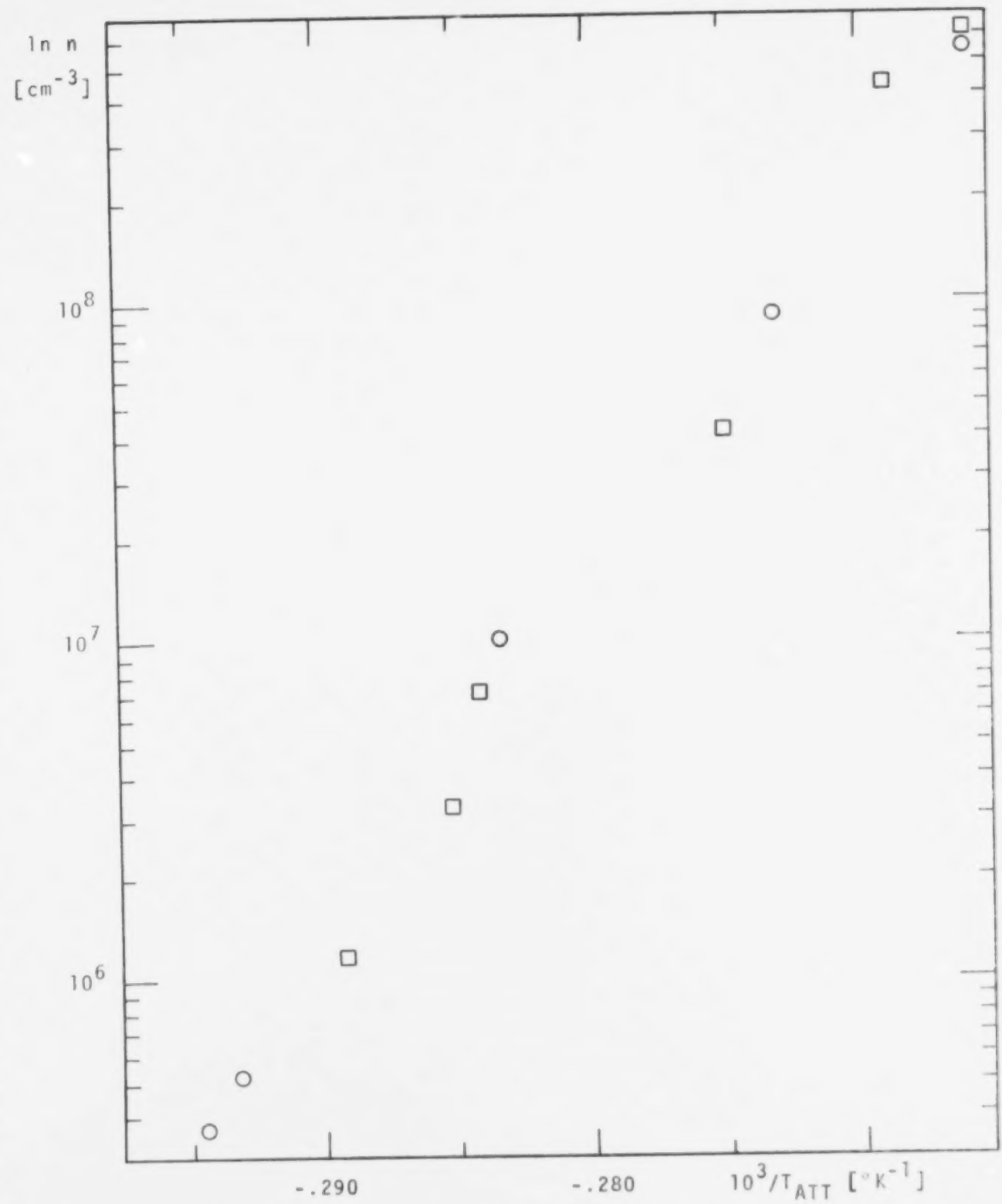

FIG. 34 PARTICLE NUMBER DENSITY AS A FUNCTION OF THE INVERSE OF THE ABLATING SURFACE TEMPERATURE

V. SUMMARY

Controlled transpiration cooling of the anode of a high intensity arc is employed in order to generate ultrafine aerosol particles of predetermined size which are of current interest for air pollution and medical research.

The particles are generated by ablation from the high temperature arc attachment area on the inside surface of a nozzle-shaped transpiration cooled porous anode.

The inherent instability of the transpiration cooling process is circumvented by a new design first employed in this work: the plenum chamber surrounding the anode is subdivided into several independent plenum chambers which allows individual control of the pressure in each of those chambers.

The characteristics of gas flow through high temperature porous carbon are experimentally determined, as reported in the Appendix, and a theoretical model is derived to correlate the experimental results. It is shown that for temperatures $\geq$ 1000 °K and mass flowrates per unit area in the range 1 to 5 Kg/m^2sec, the inertia effects become negligible and the pressure gradient becomes a linear function of the macroscopic velocity of the gas transpiring through the porous matrix.

A method to calculate the temperature distribution in the porous anode wall is derived which only requires the knowledge of transpiring flowrate per unit area and pressure

drop through the porous matrix. These parameters can be easily measured with an accuracy of a few percent.

The governing parameters which characterize the torch operation are evaluated. The arc voltage characteristics are measured, and the experimental results for a torch with a transpiration-cooled anode appear to be qualitatively similar to those pertaining to the traditional plasma torch with a water-cooled anode. The characteristics indicate that for an arc current range from 60 to 120 Amp, the arc operation is stable and reproducible.

The transpiring flow characteristics during arc operation are measured and the corresponding temperature distributions through the porous anode segment are evaluated. This temperature distribution is unequivocally determined by values of the arc current, the transpiring mass flowrate per unit area, and the pressure drop across the porous matrix. This distribution can be reproduced from run to run. The temperature distribution through the porous material at the location of arc attachment is derived and the arc attachment size is evaluated. It is shown that the arc attachment area increases with arc current and decreases when the transpiring mass flowrate per unit area increases.

The nozzle obstruction due to the plasma jet is determined, and the increase of arc diameter is derived as a function of the arc current.

The size distributions of the aerosol particles, ablated from the arc attachment spot on the porous anode surface, are measured; and the relations associating arc parameters, anode cooling gas flowrate, and aerosol size distribution are determined. The results indicate that

1) the mean particle diameter is a decreasing function of the transpiring mass flowrate per unit area;
2) the mean particle diameter is an increasing function of the temperature of the ablating surface;
3) the logarithmic standard deviation of the particle size distribution is a decreasing function of the transpiring mass flowrate per unit area and of the arc current;
4) the logarithmic standard deviation of the particle size distribution is an increasing function of the temperature of the ablating surface;
5) the logarithmic standard deviation is an increasing function of the particle diameter, the dependence on the particle diameter being stronger at lower arc currents;
6) the experimental values of the ablated particle number density and of the ablating surface temperature can be related by the Clausius Clapeyron equation;

7) a sensitive control of the ablated aerosol size distribution for particle diameters as small as 50 Å is possible by regulating the arc current and the mass flowrate passing through the anode segment at which the arc attaches.

APPENDIX: EXPERIMENTAL INVESTIGATION OF GAS FLOW CHARACTERISTICS IN TRANSPIRATION COOLED POROUS MATRICES

A.I. INTRODUCTION

The increasing interest in transpiration cooling arises from its recent engineering applications in space vehicle thermal protection, cooling of gas turbine blades, combustion chambers, rocket nozzles, etc. Such interest is reflected in the extensive research work which has been carried out on heat and mass transfer in the interior of porous matrices. Many papers on the subject can be found in the literature [31-63]. In recent years, the application of transpiration cooling has been extended to high intensity arc plasma generators [64-86].

High intensity arc plasma torches are widely used in modern technology by the chemical industry, in plasma wind tunnels, for cutting, welding, spherodizing, spraying of refractory materials, for space flight and reentry simulation, etc. High efficiency, simple design, and high enthalpy level in the emerging plasma jet are required characteristics for such plasma torches. They can be improved if conventional water cooling systems, applied at the present time to all commercial torches, are substituted by transpiration cooling systems. If a porous constrictor tube and a porous anode, both transpiration cooled, are incorporated in the design of

a plasma torch, the heat losses to the walls may be reduced which allows higher power input into the arc. This leads to higher enthalpy levels in the emerging plasma jet, to higher efficiencies, and to a simpler torch design since the cumbersome water cooling circuits are no longer required.

Recent investigations in connection with transpiration-cooled anodes in high intensity arcs revealed a new feature of such devices. They can be effectively used for generating monodisperse, ultrafine aerosols in a well-controlled size range, as illustrated in the main part of this report.

The study presented in this Appendix is directed toward a better understanding of the gas flow characteristics of porous materials which is essential for the interpretation and prediction of the performance of plasma torches with transpiration cooled anodes.

In the first part of the Appendix, the flow uniformity is investigated, at room temperature, in the vicinity of the porous slab surface where the transpiring gas leaves the matrix; and the influence of the distance from the surface and of the slab thickness on the flow uniformity is determined.

In the second part, the characteristics of the gas flow through porous carbon are experimentally determined, for temperatures in the range from 300 °K to 2000 °K; and a theoretical model is derived to correlate the experimental results.

A.II. INVESTIGATION OF THE UNIFORMITY OF THE GAS FLOW DOWNSTREAM OF THE POROUS SLAB

The transpiring gas passing through the anode of a plasma torch emerges from the porous anode surface which faces the arc. In this region fluidynamic interactions occur between the transpiring gas flow and the arc itself. In order to avoid undesirable asymmetries and erratic arc behavior in the anode attachment region, it is desirable that the flow pattern of the transpiring gas emerging from the porous matrix is as uniform as possible.

The gas passes through submicron capillary channels inside of the porous matrix and emerges at its surface in the form of tiny discrete jets. This generates an intrinsic non-uniformity in the transpiring gas flow adjacent to the surface because neither the size and strength of these individual jets nor their orientation is uniform. However, if the pore diameters are sufficiently small and regularly distributed over the surface, the submicron individual jets mix with each other yielding a sufficiently uniform gas flow a few pore diameters downstream from the surface. Therefore, this intrinsic non-uniformity should not produce any major asymmetries of the arc in the anode region, excluding the immediate vicinity of the anode surface from this consideration. Very little is known in this situation about the actual attachment of the arc on a microscopic scale. Undesirable asymmetries and

erratic arc behavior in the anode region are probably caused by macroscopic non-uniformities in the transpiring gas flow generated, for example, by a "non-uniform" pore size distribution of the porous matrix.

In the following, the experimental investigation of these flow non-uniformities will be described.

A.II.A. Experimental Procedure and Results

A schematic of the apparatus used for this investigation is shown in Fig. 35. Essentially, it consists of two cylindrical concentric plenum chambers, which feed gas to two concentric sectors of the porous sample. The inner plenum chamber walls consist of a brass tube: A sharp edge is machined on the upper end of the tube which is in contact with the upstream surface of the porous sample. A fine thread on the outer surface of the tube allows for vertical adjustment with respect to the sample. In this way, a good "contact" between plenum chamber upper edge and the porous matrix surface can be obtained for different sample thicknesses. On the other side of the specimen, a concentric brass tube of the same diameter can be vertically positioned to support the central portion of the sample against the pressure forces which become important at high values of the transpiring mass flow rate.

A 0.5 mm diameter impact pressure probe can be automatically traversed in various horizontal planes downstream of the

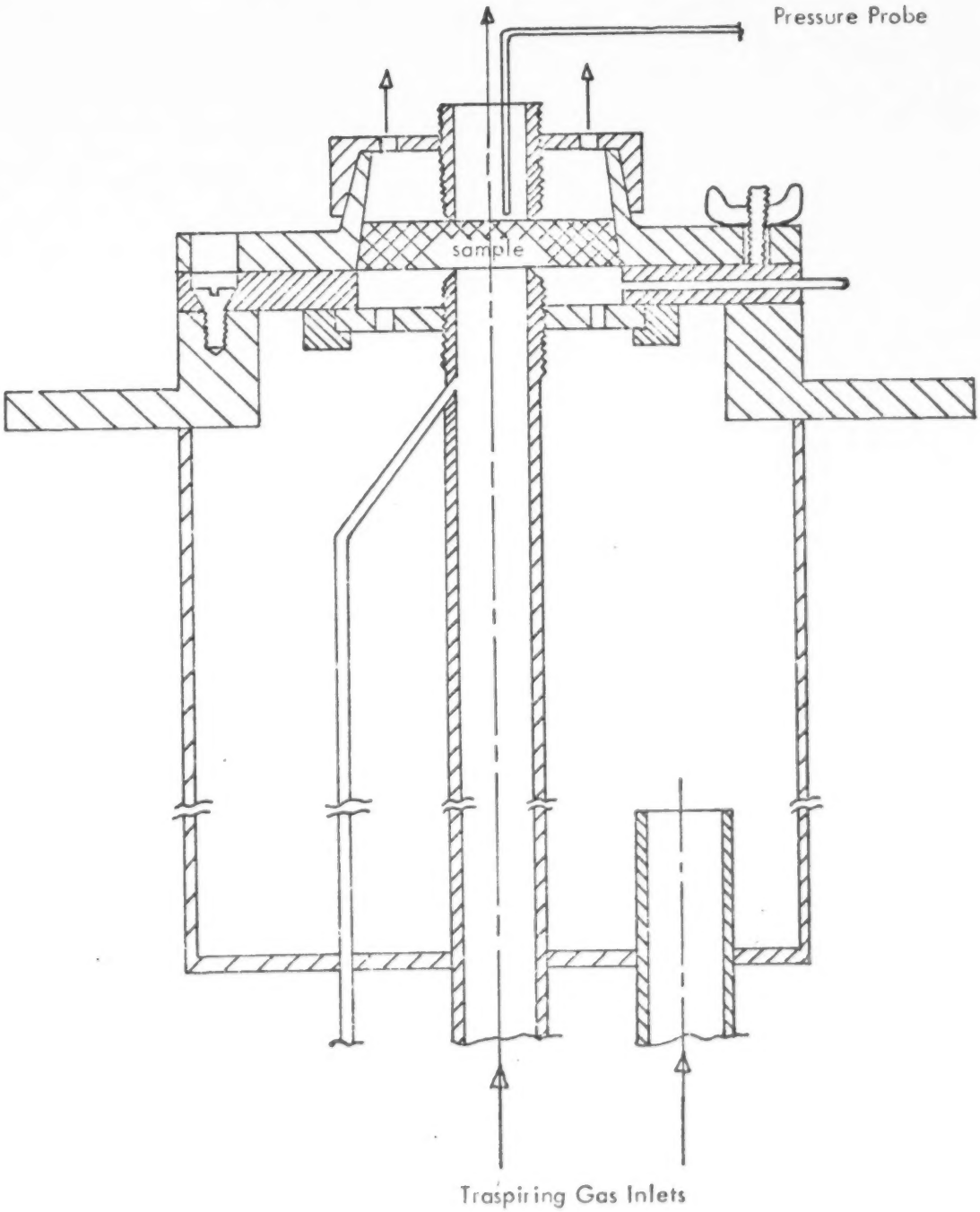

FIG. 35 SCHEMATIC OF THE APPARATUS FOR POROUS MATRICES COLD FLOW TESTS

surface. By means of a pressure transducer and a recorder, the impact pressure values pertaining to the transpiring gas flow can be determined as a function of the probe location with respect to the porous sample; in this way, the local velocity of the transpiring gas can be evaluated in the entire region downstream of the central portion of the porous sample.

A schematic of the control circuits is shown in Fig. 36. The operating procedure for the flow tests is the following: The pressure is adjusted to the desired value within the inner plenum chamber and then it is increased in the outer chamber until the same value is reached. When no pressure difference exists between the two chambers, the impact pressure measurements are taken; and at the same time, the mass flow rate is measured passing through the inner plenum chamber and through the central region of the sample. The same procedure is repeated for different pressure drops, i.e., for different mass flow rates of the transpiring gas and for different porous sample thicknesses.

The purpose of the outer plenum chamber is twofold. The seal between the edge of the inner plenum chamber and the porous surface is inherently imperfect, as any mechanical seal on porous surfaces. Therefore, leaks would develop in this region which would result in errors in the evaluation of the mass flow rate transpiring through the sample test section. With the two plenum chamber system described here, these leaks

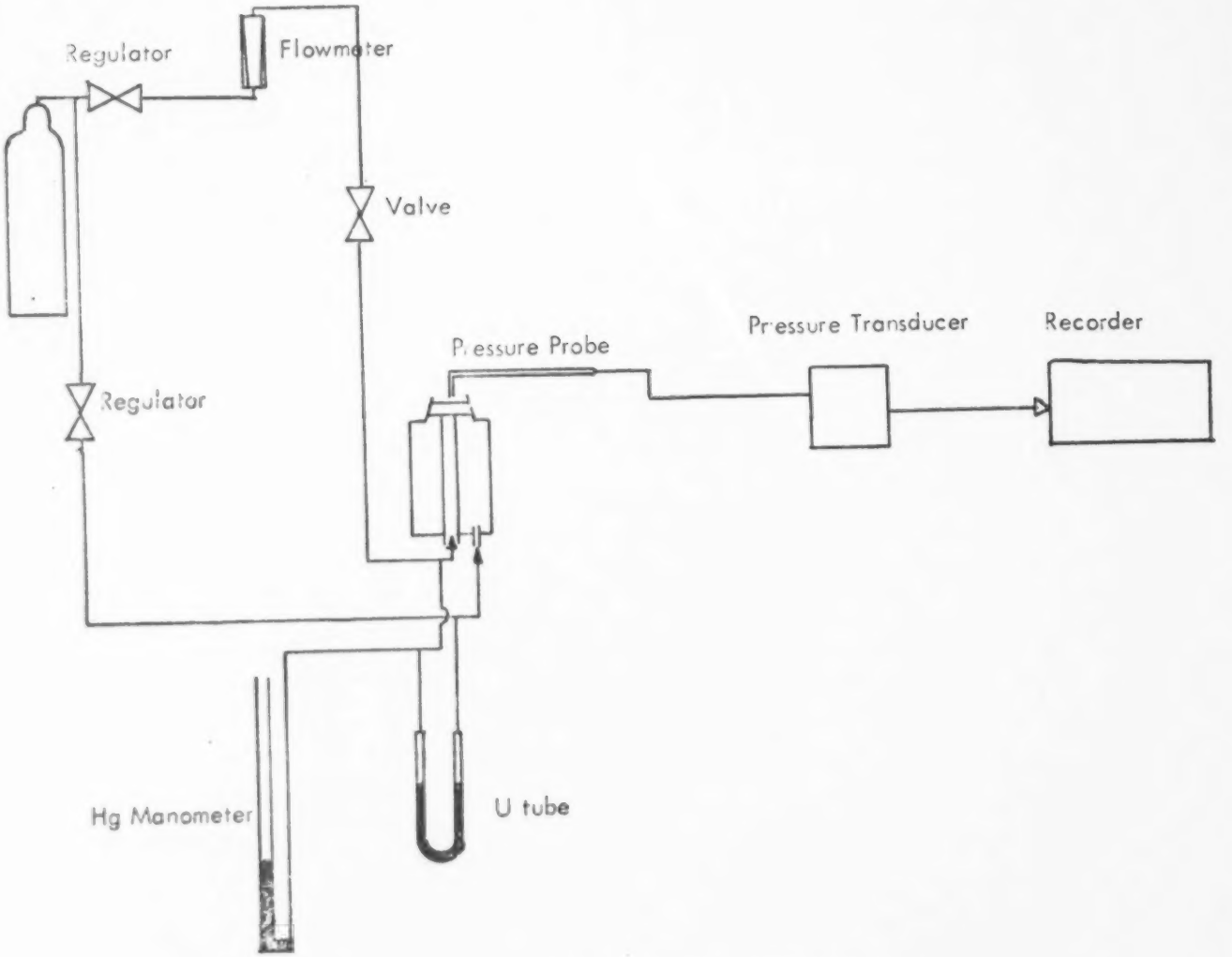

FIG. 36 SCHEMATIC OF THE CONTROL CIRCUITS

are entirely avoided since no pressure drop exists in the area where they would develop. In essence, the outer plenum chamber acts as a pressure-equilibrated guard ring around the central portion of the sample used as test section. In this way, the end effects at the contours of the test section are eliminated and a one-dimensional gas flow through the sample is insured.

Seven porous carbon samples are tested, having thicknesses ranging from 1.0 mm to 9.4 mm. For each sample and for different values of the mass flow rate transpiring through the test section, the impact pressure of the transpiring gas is determined in three different planes downstream of the sample, parallel to the sample surface, and at a distance of 1.5 mm, 3 mm, and 4.5 mm from the surface. Fig. 37 shows the coordinate system chosen for this analysis.

In each of the above-mentioned planes, the impact pressure values are determined according to the following procedure. By a micrometric drive, the probe is manually set at $x = -5.5$ mm and $y = -5.5$ mm. The probe is then automatically traversed in $+y$ direction at a speed of about 0.3 mm/sec, and the impact pressure signals from the pressure transducer are recorded by means of a Moseley Autograph Recorder, Model 7100 B. The same measurement is repeated driving the probe in the opposite direction. By means of the micrometric drive, the probe is then shifted in steps of 0.4 mm in $+x$ direction and the

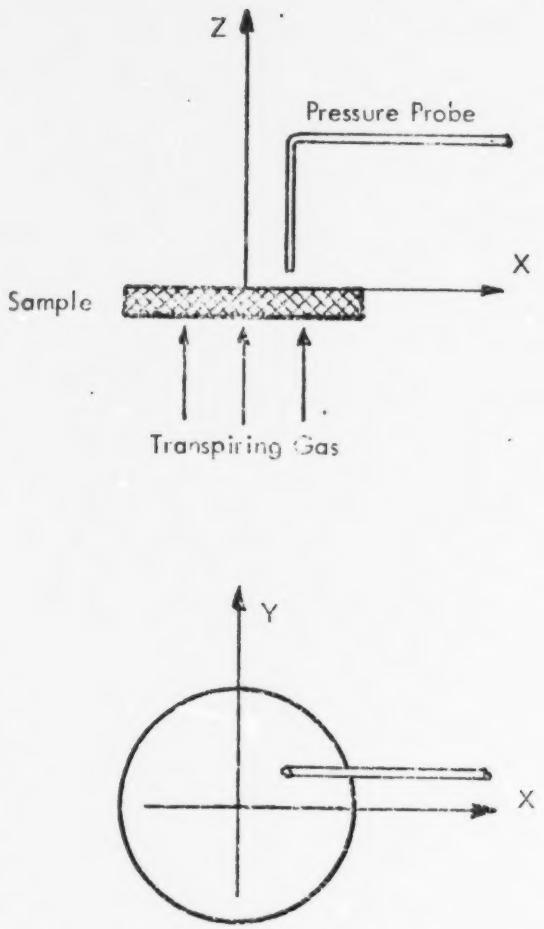

FIG. 37 COORDINATE SYSTEM

traversing in y direction occurs as described before. The procedure is repeated until a total area of about 11 x 11 mm is examined.

The results show that for any given x value, the impact pressure curves recorded in both directions are almost identical. Fig. 38 demonstrates this fact and provides at the same time an indication for the magnitude and frequency of the fluctuations recorded by the pressure probe.

In Fig. 39, typical recordings from an automatic traversing in +y direction are represented for a sample of 2.5 mm thickness. The curves refer to the same x location and to z values of 1.5, 3.0, and 4.5 mm. Three-dimensional plots derived from impact pressure curves covering the entire test area and taken at the previously-specified z values can be precisely constructed, proving that the data are consistent with each other. These findings prove that the data acquisition system is reliable, yields reproducible results, and has a sufficient spatial resolution.

For each porous sample, data are recorded for three z planes and for each value of the transpiring mass flow rate per unit area, resulting in 27 curves in +y direction and 27 corresponding curves in -y direction. By means of a digitizer system coupled to the Hybrid Computer of the University of Minnesota, these curves are digitized in a cartesian coordinate system. From each of the digitized impact pressure curves,

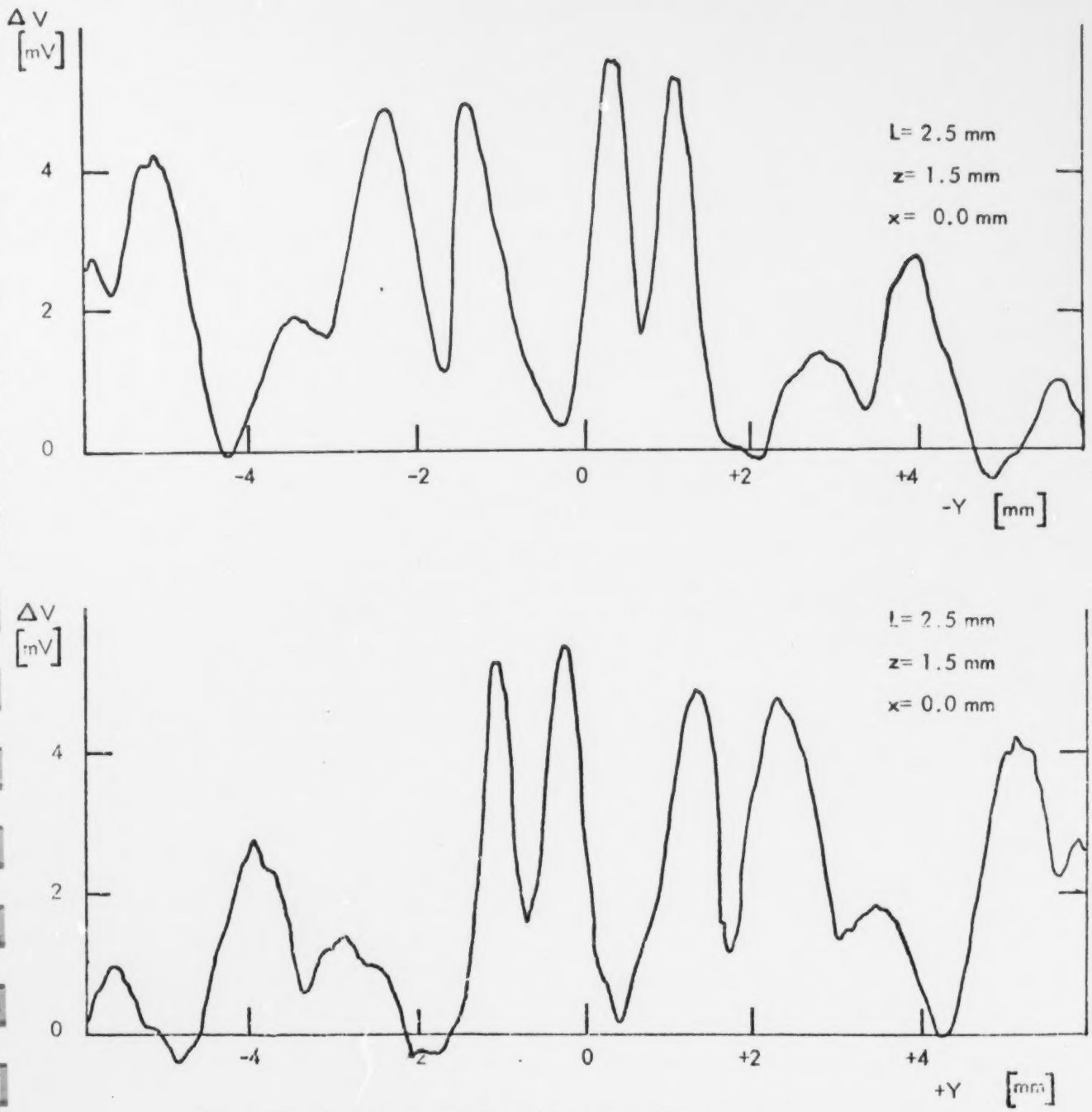

FIG. 38 TYPICAL IMPACT PRESSURE RECORDINGS IN ±y DIRECTION AT A GIVEN x AND z VALUE

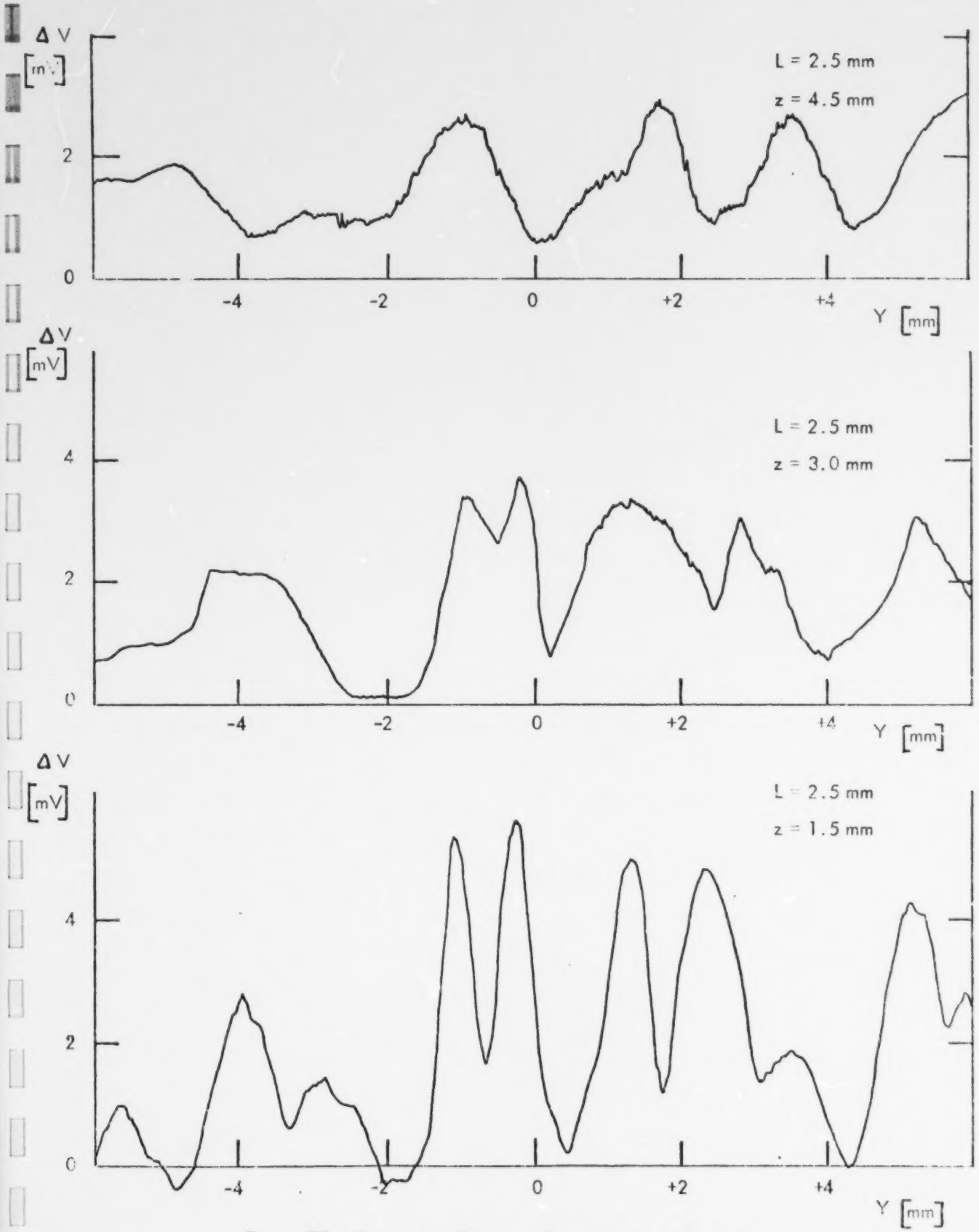

FIG. 39 TYPICAL IMPACT PRESSURE RECORDINGS IN y DIRECTION AT A GIVEN x VALUE

the corresponding velocity profile is derived. The velocity curves are then integrated and the average mass flow rate per unit area of the sample at each x location is evaluated. Typical results are shown in Fig. 40 referring to a 6.25 mm thick porous sample and to a total transpiring mass through the test section of 2 g/sec, corresponding to an average mass flow rate per unit area of 0.84 g/sec cm^2. The value of the mass flow rate per unit area evaluated at z = 3 mm from each impact pressure curve is plotted versus the x coordinate value pertaining to each curve. The dotted line represents the value of the mass flow rate per unit area evaluated from the total mass flow rate through the test section, given by the flowmeter, assuming that the flow is uniform over the test section. The results agree within ±9%, and this value is never exceeded by any of the results obtained in all the other runs. In Fig. 41, the average value of the mass flow rate through the entire test section calculated from the velocity curves is plotted versus z for sample thicknesses of 1.8, 6.25, and 9.4 mm and for a value of $\dot{m}/A$ = 8.4 Kg/sec m^2, derived from flowmeter readings. The agreement is in this case within ±5%.

The impact pressure readings shown in various figures may be correlated with the average impact pressure which is proportional to the square of the average velocity. Fig. 42 shows the average and the actual impact pressure. The size

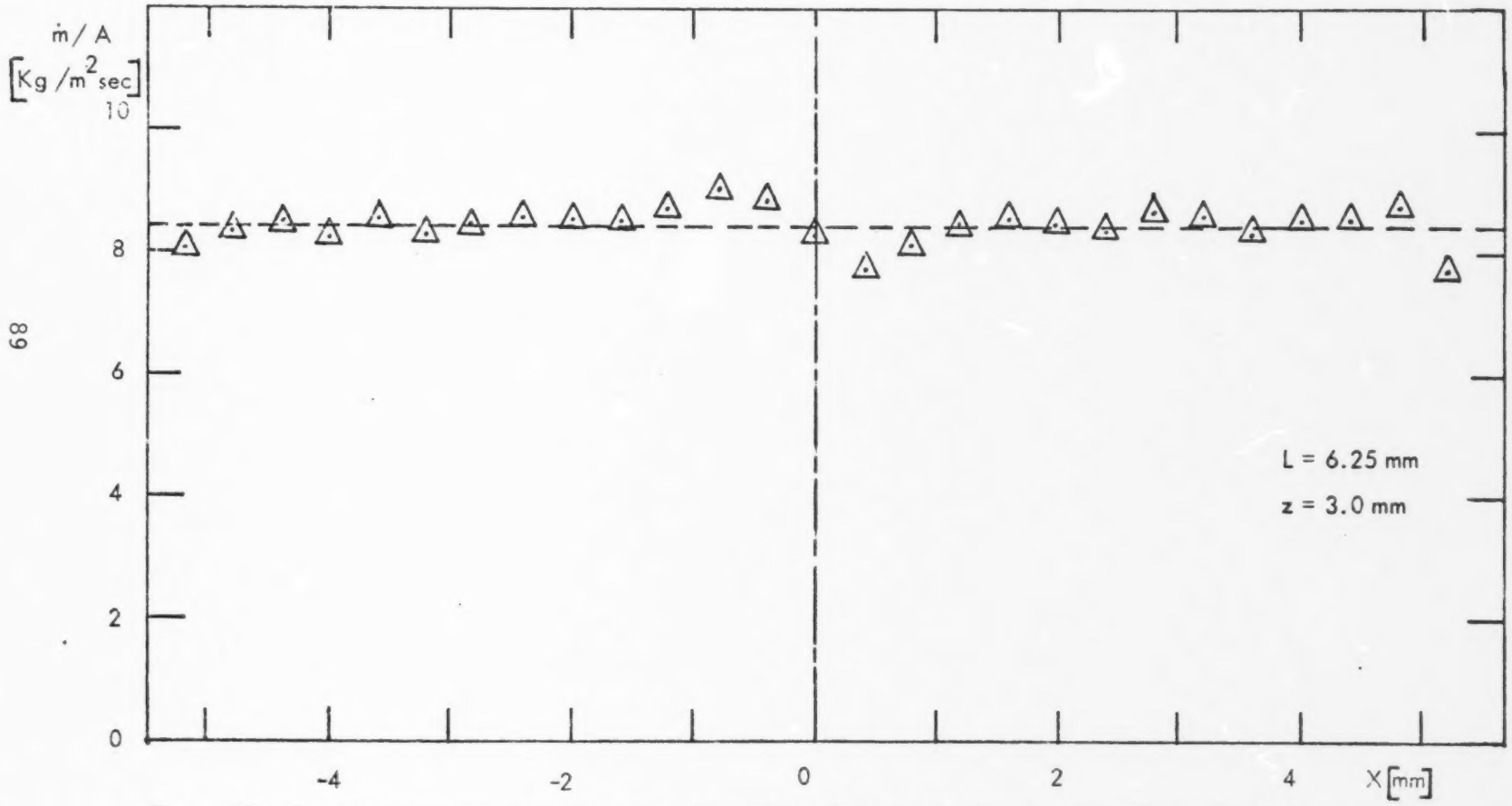

FIG. 40 COMPARISON OF TRANSPIRING GAS MASS FLOWRATE VALUES PER UNIT AREA OBTAINED BY INTEGRATION OF VELOCITY PROFILES AND FROM FLOWMETER READINGS AS A FUNCTION OF x FOR A GIVEN z VALUE

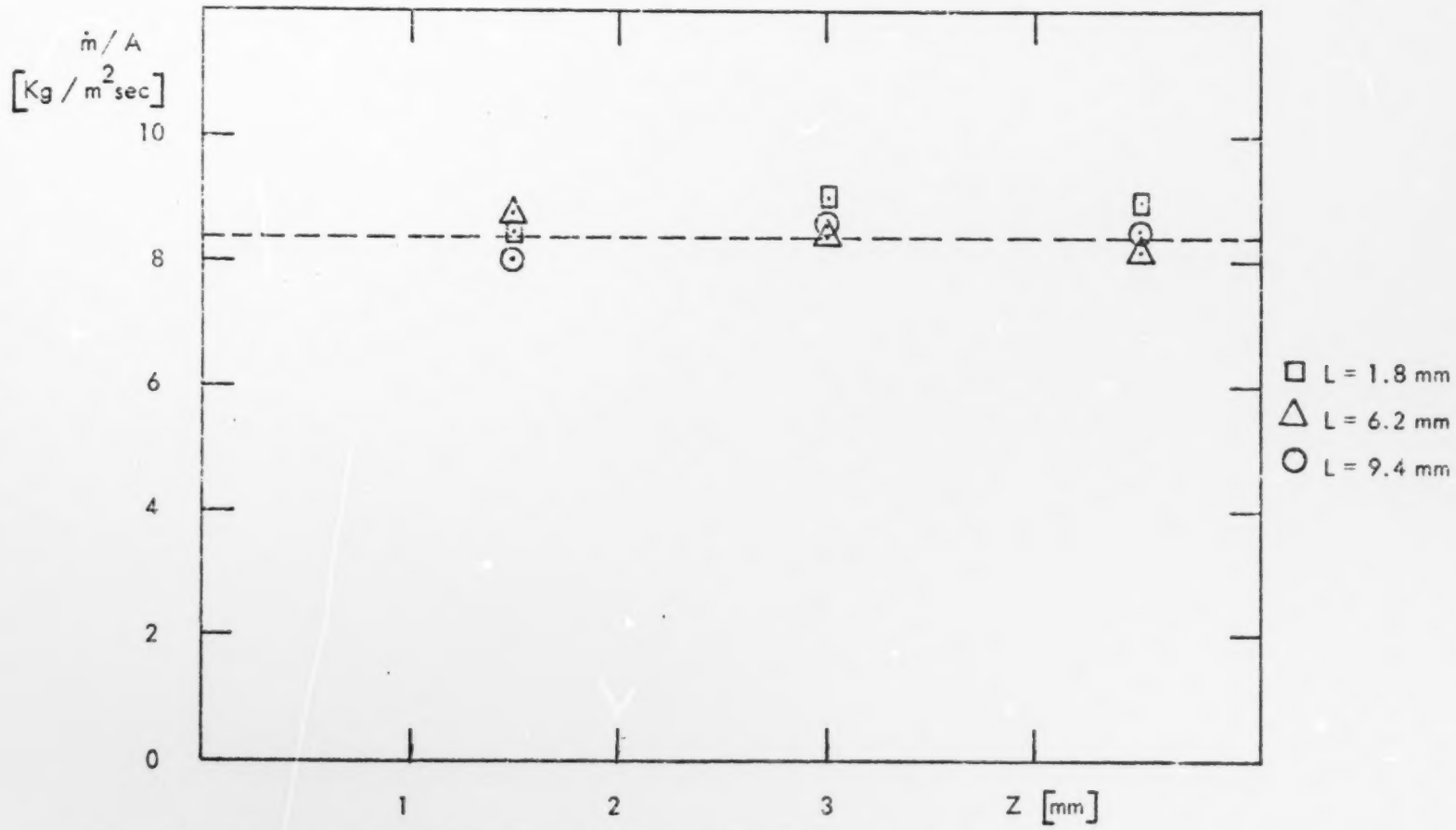

FIG. 41 COMPARISON OF TRANSPIRING GAS MASS FLOWRATE VALUES OBTAINED BY INTEGRATION OF VELOCITY PROFILES OVER THE ENTIRE TEST SECTION AND FROM FLOWMETER READINGS AS A FUNCTION OF z LOCATION

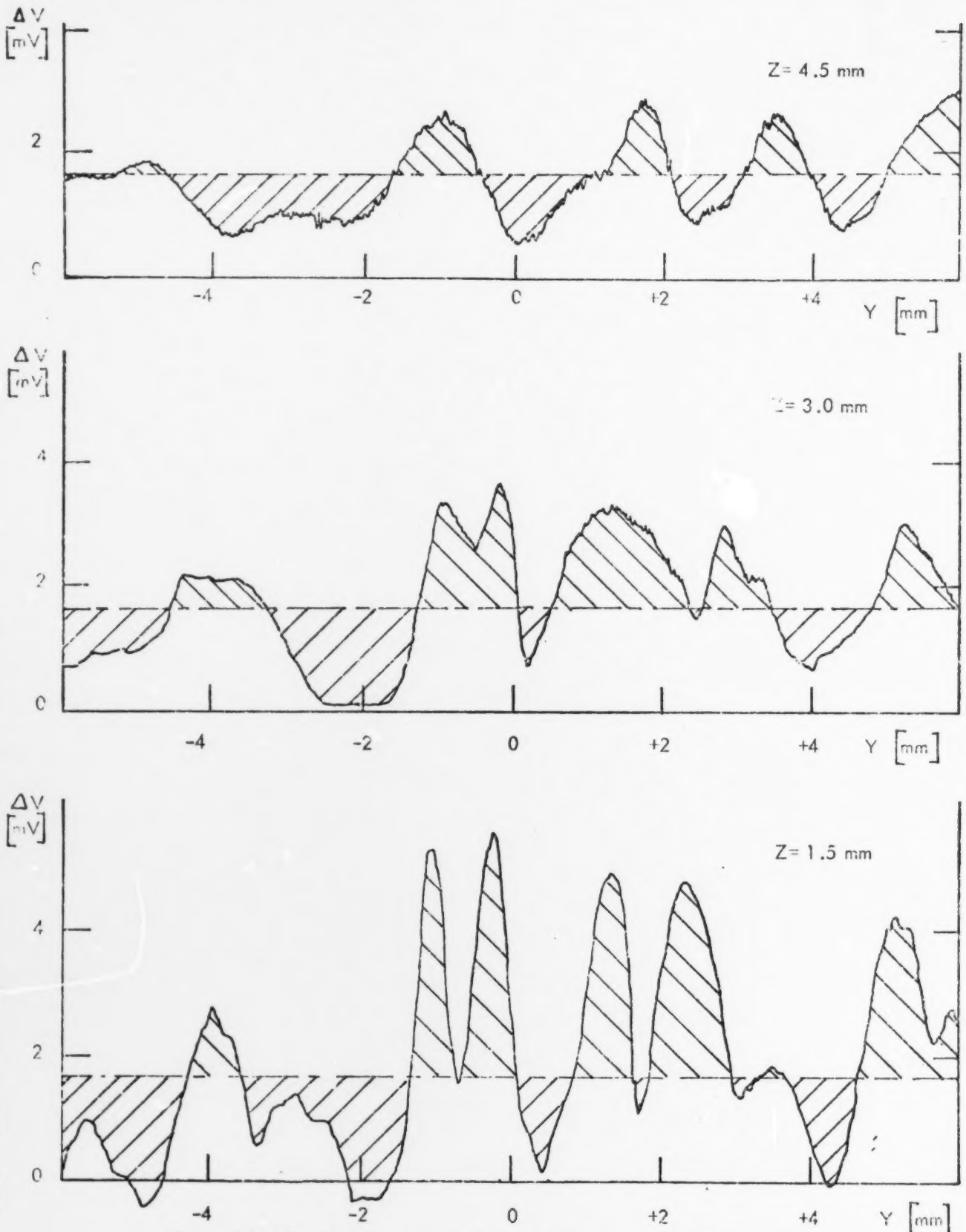

FIG. 42 EXAMPLE OF THE EVALUATION OF THE PARAMETER R

of the cross-hashed areas is a measure for the uniformity of the flow through the porous sample. The smaller this area is, the better is the uniformity of the flow. The ratio of this cross-hashed area to the total area under the impact pressure curve is defined as a parameter, R, which characterizes the uniformity of the gas flow downstream of the sample. Fig. 42 also reveals that the flow uniformity improves with increasing z. Since all the impact pressure diagrams show the same pattern, there is no need for another parameter to characterize the flow uniformity.

The average value of the parameter defined above is evaluated for the 27 curves pertaining to each z plane, to each sample, and to each value of the transpiring mass flow rate. Since the dependence of this parameter on the transpiring mass flow rate is negligible, only results referring to a mass flow rate of 8.4 Kg/sec m^2 are reported in the following. In Fig. 43, the average value of R is plotted versus the distance from the surface for each sample; and Fig. 44 shows the average value of R plotted versus the sample thickness for z values of 1.5, 3.0, and 4.5 mm.

A.II.B. Conclusions

The experimental data obtained for room temperature velocity measurements downstream of the porous carbon samples permit the following conclusions.

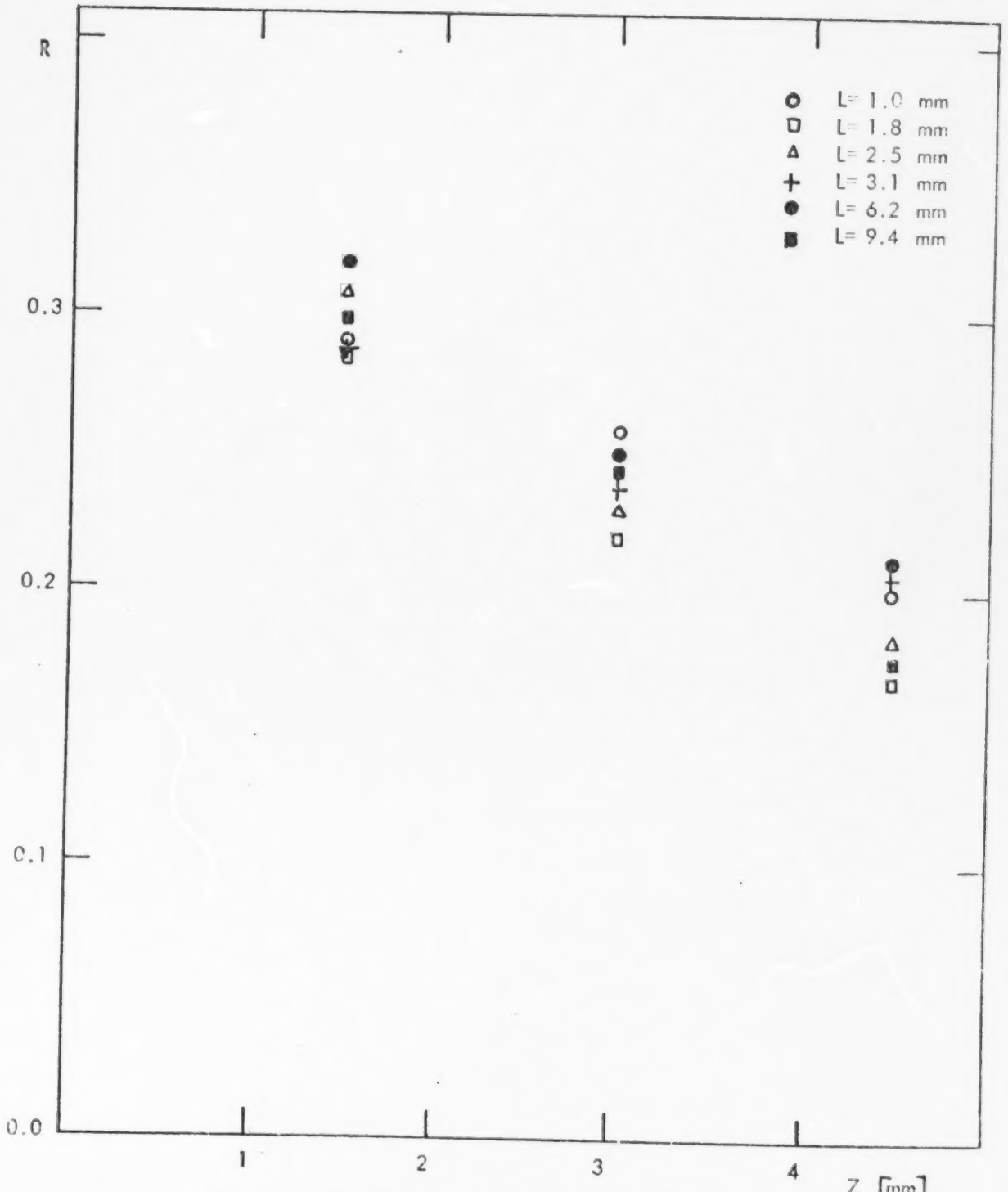

FIG. 43 AVERAGE VALUE OF R AS A FUNCTION OF THE DISTANCE FROM THE SAMPLE SURFACE

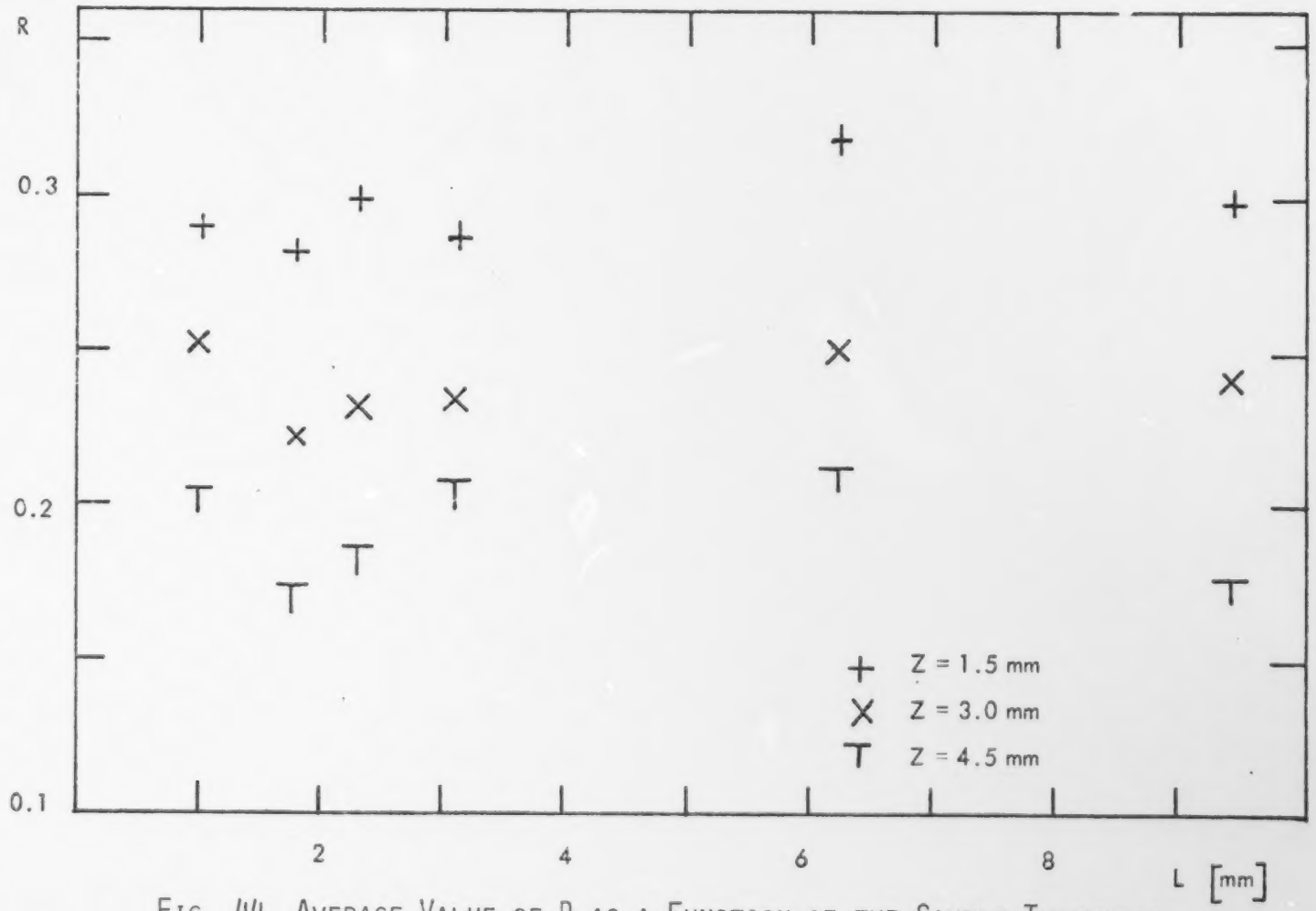

FIG. 44 AVERAGE VALUE OF R AS A FUNCTION OF THE SAMPLE THICKNESS

The data acquisition system is reliable and has sufficient spatial resolution, as borne out from the impact pressure curves as, for example, represented in Fig. 38 and from the three-dimensional diagrams which have been constructed from these curves. There is a fair agreement between the mass flow rate derived from the integration of the velocity curves over the test area and the readings of calibrated flowmeters as demonstrated in Fig. 41 which again testifies to the reliability of the data acquisition system.

The mass flow rate through the various sectors of the test section characterized by each x value is uniform as shown in Fig. 41 which means that the permeability of the porous carbon matrices is rather uniform throughout the sample.

The flow non-uniformity, described by the parameter R, decreases with increasing distance from the surface as shown in Fig. 43. This is due to the mixing of the small individual jets emerging from the capillary channels terminating at the matrix surface. The larger the distance from the surface, the more complete is the mixing among the individual jets which equalizes the originally existing non-uniformities of the transpired gas.

Data represented in Fig. 44 show that the flow uniformity is independent from the porous sample thickness for the material examined in the present work. This is probably due to the fact that in such porous matrices, having pore diameters

in the order of microns, the flow is fully randomized after a path length of a few hundredths of a millimeter within the matrix. Therefore, after such a distance, the flow "loses memory" of the upstream non-uniformities. A strong dependence on the sample thickness can be expected for very thin samples. Since all the samples investigated are much thicker than the critical thickness, no improvement in the flow uniformity can be expected by increasing the sample thickness.

A.III. DETERMINATION OF GAS FLOW CHARACTERISTICS IN HIGH TEMPERATURE POROUS CARBON

A.III.A. Background

The pressure gradient in one-dimensional fluid flow in porous media can generally be represented by a power series

$$\frac{dp}{dx} = au + bu^2 + cu^3 + \ldots \tag{A.1}$$

where a, b, etc., are coefficients depending on the properties of the fluid and the porous media, and u represents the macroscopic velocity. Assuming [40] that:

$$\frac{dp}{dx} = f\ (u,\ K,\ \rho,\ \eta) \tag{A.2}$$

where K represents the permeability of the porous medium, ρ the density of the transpiring fluid, and η its dynamic viscosity, we obtain the following dimensional equation:

$$\left[\frac{dp}{dx}\right] = [u^W K^X \rho^Y \eta^Z] \tag{A.3}$$

Introducing the fundamental units of mass, M; length L; and time, T*; of the various parameters into Eq. (A.3) yields:

$$[M\ L^{-2}\ T^{*-2}] = [M^{\ Y+Z}\ L^{\ W+2X-3Y-Z}\ T^{*\ -W-Z}] \tag{A.4}$$

and solving for X, Y, Z in terms of W we have:

$$\frac{dp}{dx} = f\ (u^W\ K^{\ (W-3)/2}\ \rho^{W-1}\ \eta^{2-W}) \tag{A.5}$$

Therefore, Eq. (A.1) becomes:

$$\frac{dp}{dx} = \sum_{W=1}^{n} C_W u^W K^{(W-3)/2} \rho^{W-1} \eta^{2-W} =$$

$$C_1 \frac{\eta u}{K} + C_2 \frac{\rho}{K^{1/2}} u^2 + \ldots \qquad (A.6)$$

in which C_W, C_1, C_2 are dimensionless constants of proportionality.

Most of the experimental results for one-dimensional flow through porous materials may be correlated by an equation of the type

$$\frac{dp}{dx} = A^* \eta u + B^* \rho u^{\xi} \qquad (A.7)$$

where A* and B* are so-called "constants", and ξ is a number between 1 and 2. The parameter A* is the inverse of the Darcy permeability constant K [87]. The first term on the right-hand side of Eq. (A.7) represents the portion of the pressure gradient due to viscous effects, while the second term represents the contribution due to inertial effects. The exact nature of the inertial contribution is not well understood. It is unlikely that turbulence exists in a fine-grained porous material. The majority of the inertial effects are probably due to expansion and contraction of the fluid, rapidly changing direction of the flow path, etc. If the experimental data on the flow of gases through fine-grained

porous carbon are correlated with Eq. (A.7), the results indicate a best fit for $\xi = 2$ for these types of materials.

Using the perfect gas law and integrating Eq. (A.7) to the thickness, l, of the porous matrix, we obtain

$$\frac{\Delta(p^2)}{2l\ R^*T\ \eta(\dot{m}/A)} = A^* + B^*\ \frac{1}{\eta}\ \left(\frac{\dot{m}}{A}\right) \tag{A.8}$$

If A* and B* can be considered constant, by plotting the left-hand side of Eq. (A.8) versus $\left(\frac{1}{\eta}\right)\ \left(\frac{\dot{m}}{A}\right)$, a straight line is obtained, the slope of which will yield B* while A* will be obtained from its intercept with the ordinate.

Since the ratio of the second to the first term in Eq. (A.7) represents the ratio of the inertial to the viscous forces, a modified Reynolds number for porous media may be defined as

$$N_{Re} = \left(\frac{B^*}{A^*}\right)\ \left(\frac{\dot{m}}{A}\ \frac{1}{\eta}\right) \tag{A.9}$$

and Eq. (A.8) becomes

$$\frac{\Delta(p^2)}{B^*l\ R^*T\ (\dot{m}/A)^2} = \frac{2}{N_{Re}} + 2 \tag{A.10}$$

Since the left-hand side of Eq. (A.10) is a ratio of friction forces to inertial forces, it represents a friction factor. It follows from Eq. (A.10) that the friction factor is represented by $2/N_{Re}$ in the Darcy region and by 2 in the inertial region. The above equations are valid for one-

dimensional, constant property fluid flow and when A* and B* can be considered constants.

The "constants" A* and B* are, of course, dependent on the geometry of the medium, which can be described only by macroscopic quantities, such as porosity, tortuosity, specific surface, and pore size distribution. The structure may change to a certain extent as the ambient conditions are varied. Thus, changes in pressure or temperature might be expected to affect the values of A* and B*. Little mention has been made in the literature of these effects.

The question is also open whether these "constants" themselves are dependent on the pressure and temperature when pressure and temperature variations over a wide range are considered.

It is one of the purposes of the following investigation to determine experimentally the dependence of A* and B* on pressure and temperature for a porous carbon matrix subject to temperatures in the range from 300 to 2000 °K and pressures from 10 to 25 $Kg/msec^2$. The type of porous carbon is the same as used for the investigation described in the first part of this Appendix, and the ranges chosen for T and p comprise the actual temperature and pressure values encountered by a transpiration-cooled anode of a plasma torch during the operation of the arc.

Experimental results, obtained with the apparatus represented in Fig. 35 and 36, referring to porous carbon samples at room temperature having thicknesses in the range from 1.8 to 9.4 mm, confirm that the parameters A* and B* are independent of the slab thickness. Therefore, in the following, only one sample thickness will be considered.

A.III.B. Experimental Apparatus

In the present experiment, the porous carbon sample is heated, by Joule heating, up to temperatures of 2000 °K. A variable argon mass flow rate is forced through the sample and the values of the pressure drop across the porous matrix are measured as a function of the mass flow rate for various matrix temperatures. The experimental apparatus is schematically represented in Fig. 45. The two ends of a 3 mm thick, 50 mm long, kidney-shaped porous carbon sample are pressed, in good electrical contact, on two water-cooled copper bars electrically connected to the output cables of a 50 Kw D.C. power supply. A current of 150 Amps passing through the sample is sufficient to increase the temperature of the central test area of the porous carbon, by Joule heating, up to 2000 °K. To stabilize the current, a water-cooled resistor, which is described elsewhere [88], is located in series with the porous sample. Cooling argon gas is forced through the sample by pressurizing the gas in a water-cooled copper tube, press-sealed to the porous carbon surface by means of screws located outside the

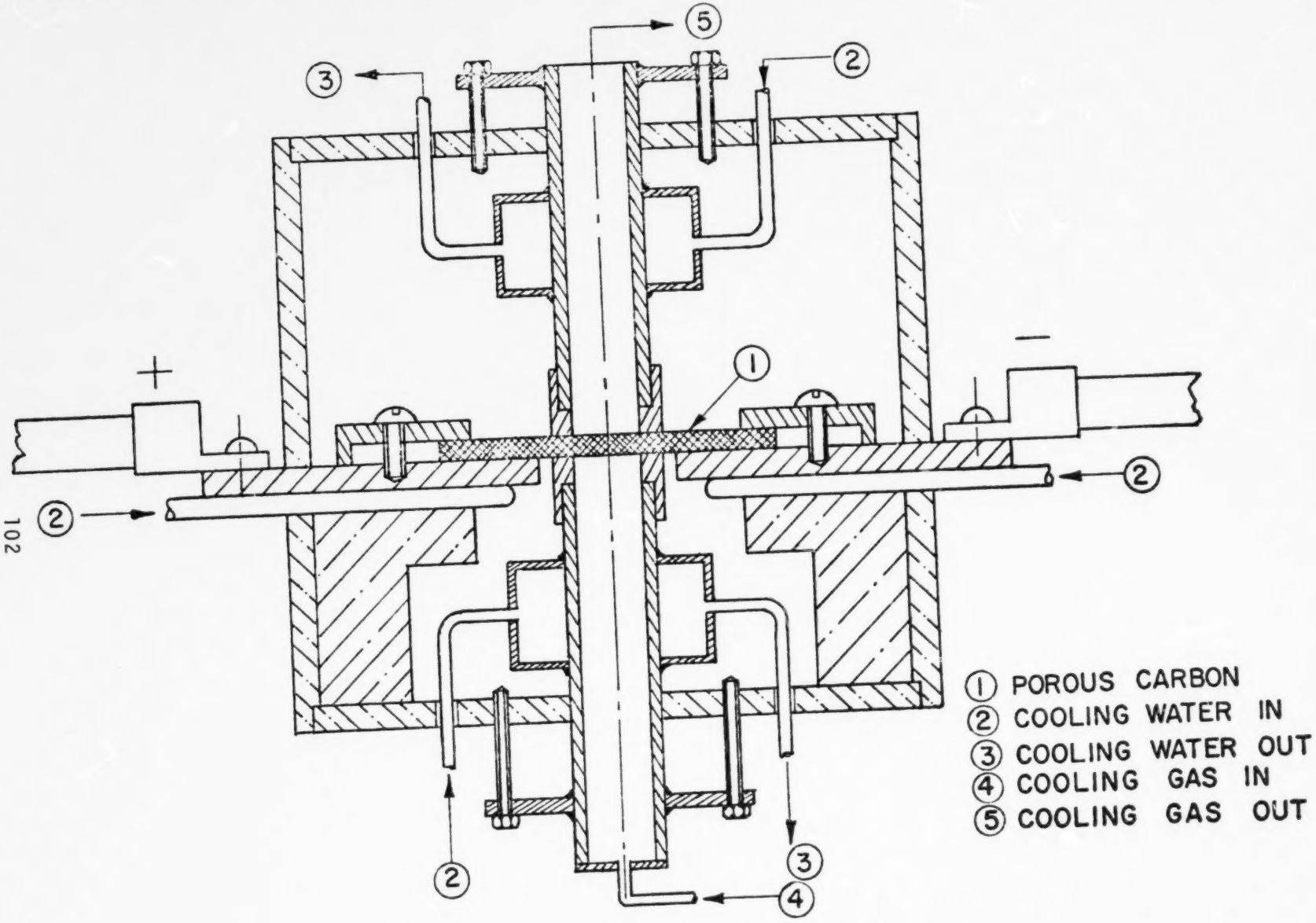

102

FIG. 45 SCHEMATIC OF THE APPARATUS FOR POROUS CARBON HIGH TEMPERATURE FLOW TESTS

plexiglas housing of the apparatus. A boron-nitride gasket, located between the copper tube and the sample, provides electrical insulation. An identical water-cooled adjustable copper tube with boron-nitride gasket is located downstream from the porous matrix and serves as argon exhaust pipe. The end of this tube is left open because it is used as a "window" for optical pyrometer readings of the porous sample test section temperature. The test area is represented by the circular part of the sample limited by the inner walls of the water-cooled copper tubes. In order to avoid reflections during the pyrometric readings, the inside wall surfaces of the tubes have been blackened.

The flow of argon cooling gas, stored in commercial bottles, is regulated by needle valves and pressure regulators; the argon flow rate is measured by calibrated Fisher and Porter flowrators and a U tube Hg manometer is used to determine the values of the pressure upstream from the porous matrix.

The temperature distribution of the outer surface of the porous test section is determined by means of a calibrated optical precision pyrometer for $T \gtrsim 850$ °K and for lower temperatures by chromel alumel thermocouples located immediately downstream from the porous surface in the exhaust tube. Thermocouples are also located on the inner edges of the boron-nitride gaskets facing the porous sample.

The entire apparatus is enclosed in a plexiglas cylindrical structure which provides a rigid support for the porous sample,

allows for a precise alignment of the copper tubes and, therefore, a leak-free seal at the sample surface. An inert argon atmosphere is maintained inside the plexiglas container to avoid oxidation of the porous carbon.

A.III.C. Experimental Procedure and Results

Initially cold flow tests have been performed at room temperature. The total pressure drop, Δp, across the porous sample is determined as a function of the argon cooling mass flow rate per unit area, $\frac{\dot{m}}{A}$.

The results are represented in Fig. 46 by the cross symbols. In order to check the accuracy of these results, a larger sample of the same porous carbon is tested in the more sophisticated apparatus developed for room temperature measurements and represented in Fig. 35 and 36. Details of this apparatus are described in the first part of the present work. As already mentioned, this apparatus, by providing a pressure-equilibrated guard ring chamber around the porous sample test area, eliminates any causes for gas leaks, ensures a one-dimensional gas flow through the sample, and eliminates end effects at the contours of the test section.

The results obtained with this apparatus are indicated by the empty-circle symbols in Fig. 46 and are in good agreement with the previously-mentioned data. This proves that the apparatus which has been used for the measurements on the heated porous carbon yields reasonably accurate results, in spite of its relatively simple design.

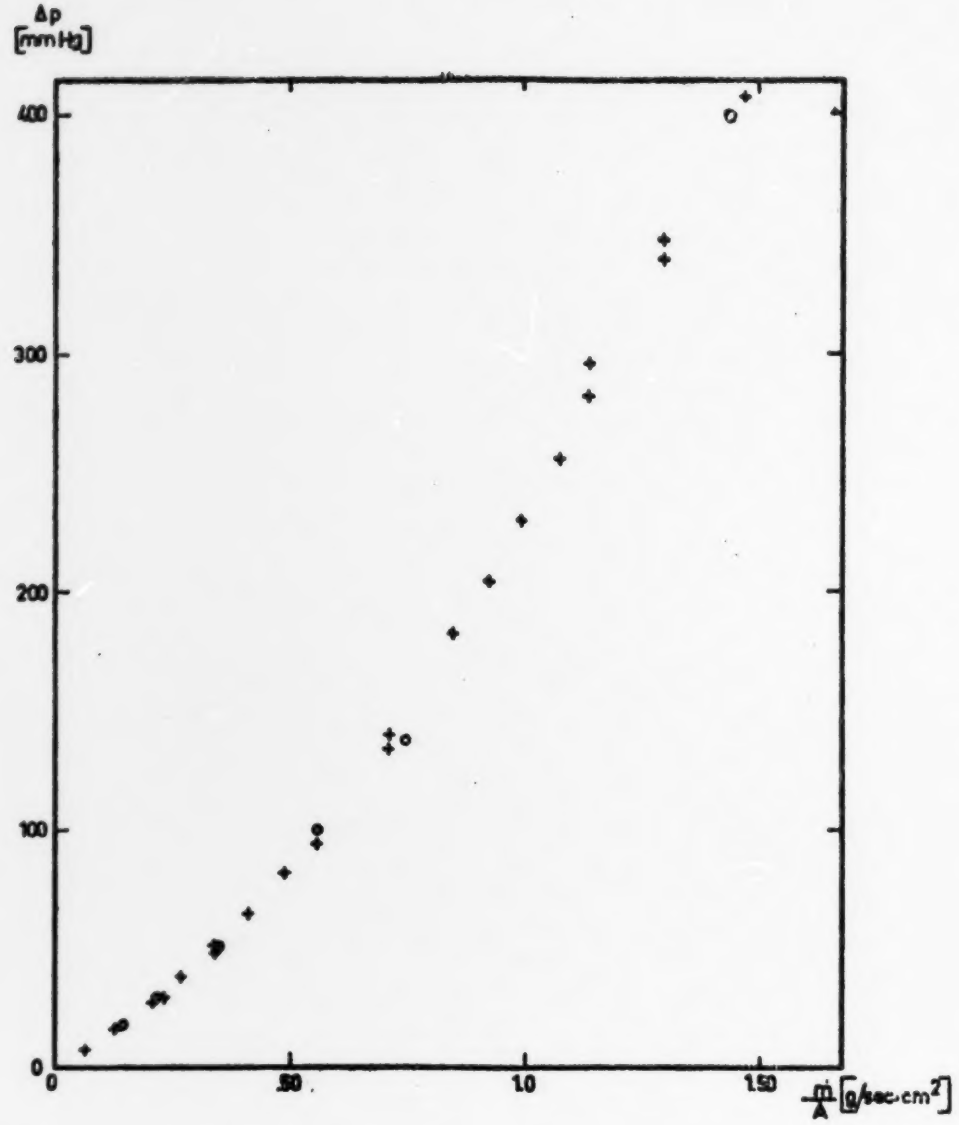

FIG. 46 POROUS CARBON COLD FLOW CHARACTERISTICS

With the assumption that the pressure gradient is constant within the sample, the room temperature values of the "constants" A* and B* of Eq. (A.7) can be determined directly from the data of Fig. 46 by numerical least square methods or by plotting the data according to Eq. (A.8) and proceeding graphically as previously described. Both methods yield for A* and B* the values $A^* = 2.1 \times 10^{10}$ $[m^{-2}]$ and $B^* = 1.16 \times 10^{5}$ $[m^{-1}]$ for room temperature conditions.

In the second part of this project, measurements of the flow characteristics at high temperature are performed following the procedure which will now be described. For each of three different argon cooling mass flow rates and for different current values in the range between 40 and 120 Amp, the total pressure drop across the sample and the temperature distribution on the surface of the sample within the test section are determined. It is assumed that the temperature profiles remain unaltered inside of the porous sample.

The results of these measurements are shown in Fig. 47, 48, and 49 where only one half of the radial temperature distribution is plotted because of the prevailing rotational symmetry of the temperature distribution. The horizontal segments in Fig. 47 and 48 indicate the temperature readings from the optical pyrometer, and their length represents the uncertainty in the determination of the radial location of the point associated with a particular temperature. For $T \lesssim 850$ °K,

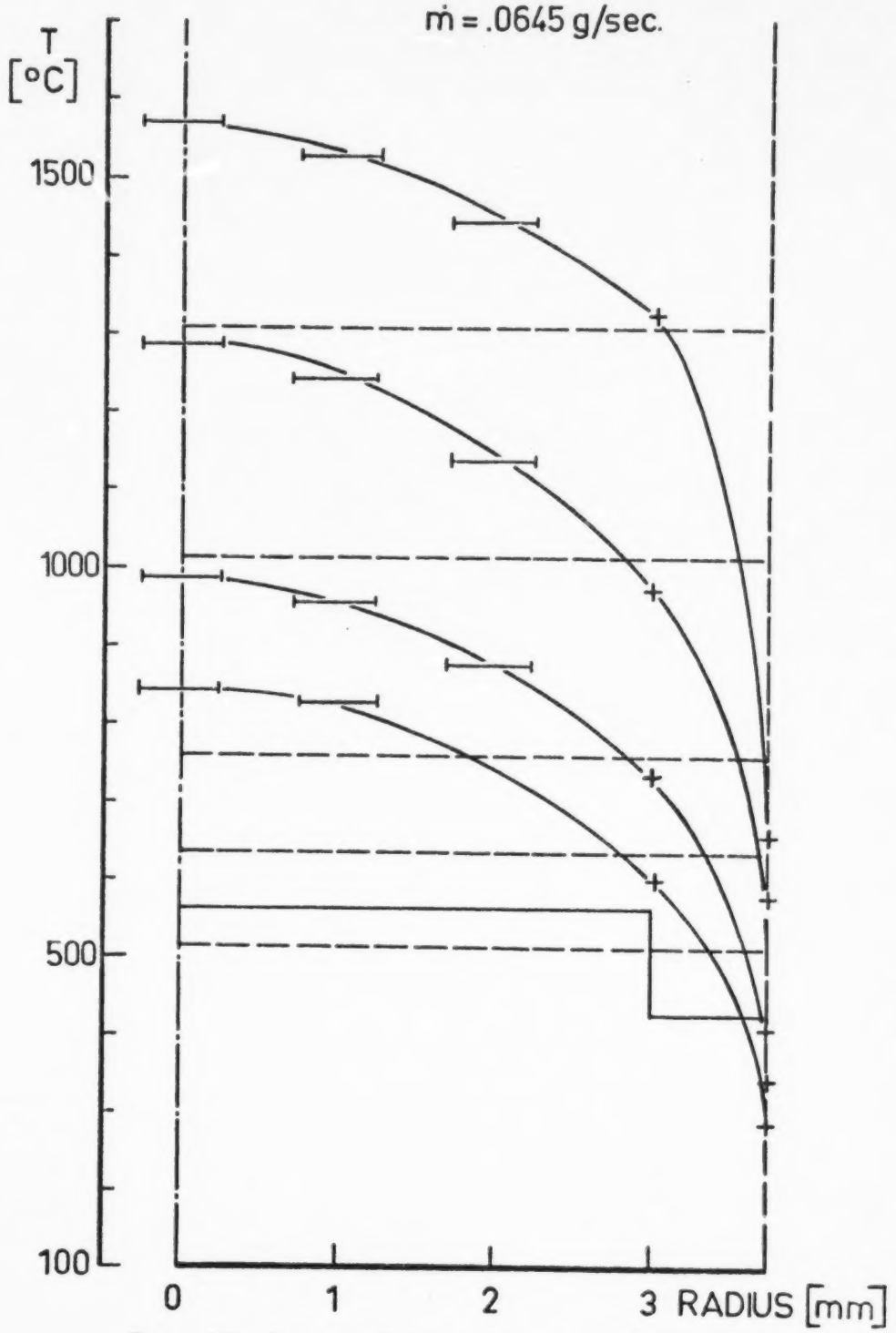

FIG. 47 POROUS CARBON SAMPLE: TEMPERATURE DISTRIBUTION

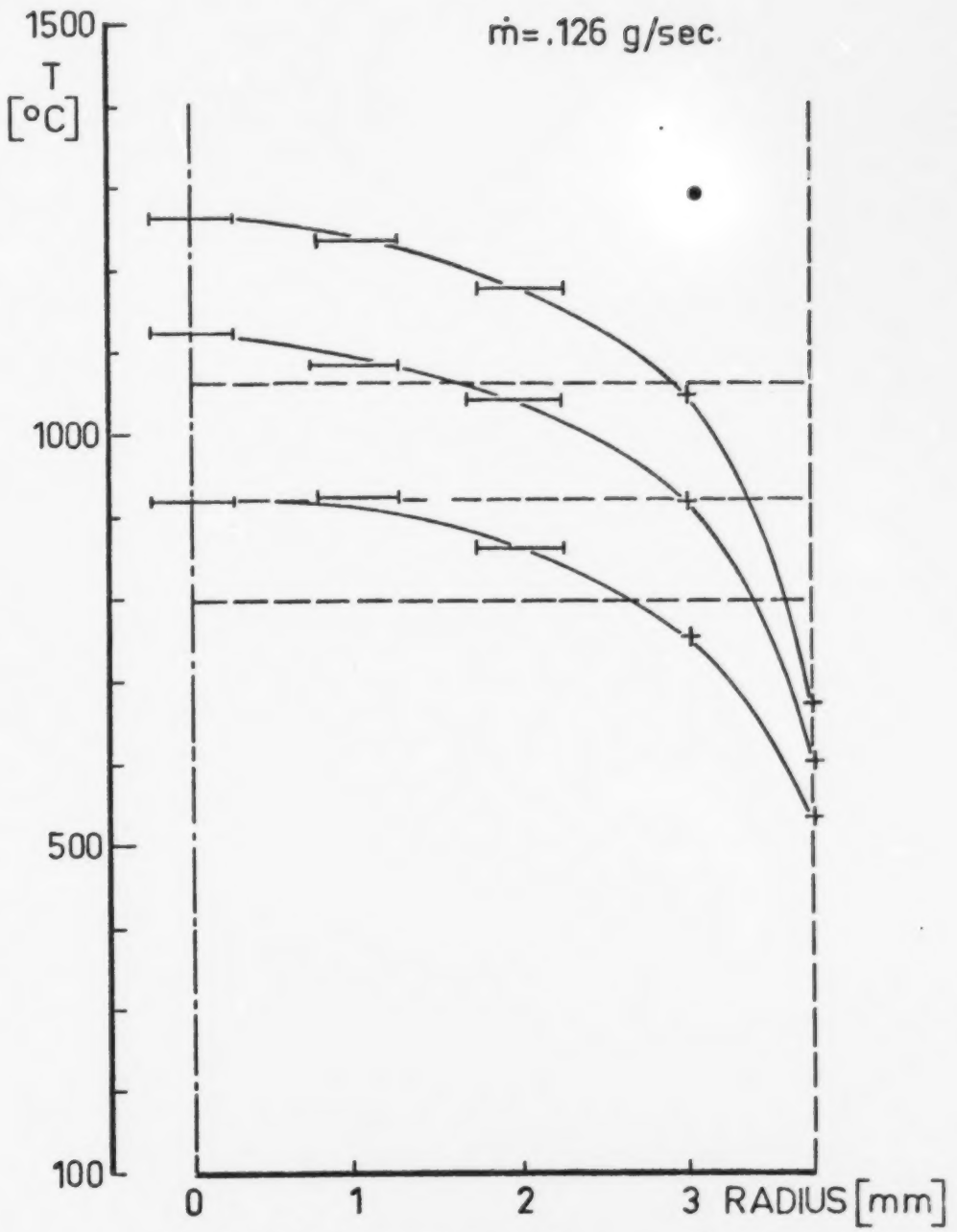

FIG. 42 POROUS CARBON SAMPLE: TEMPERATURE DISTRIBUTION

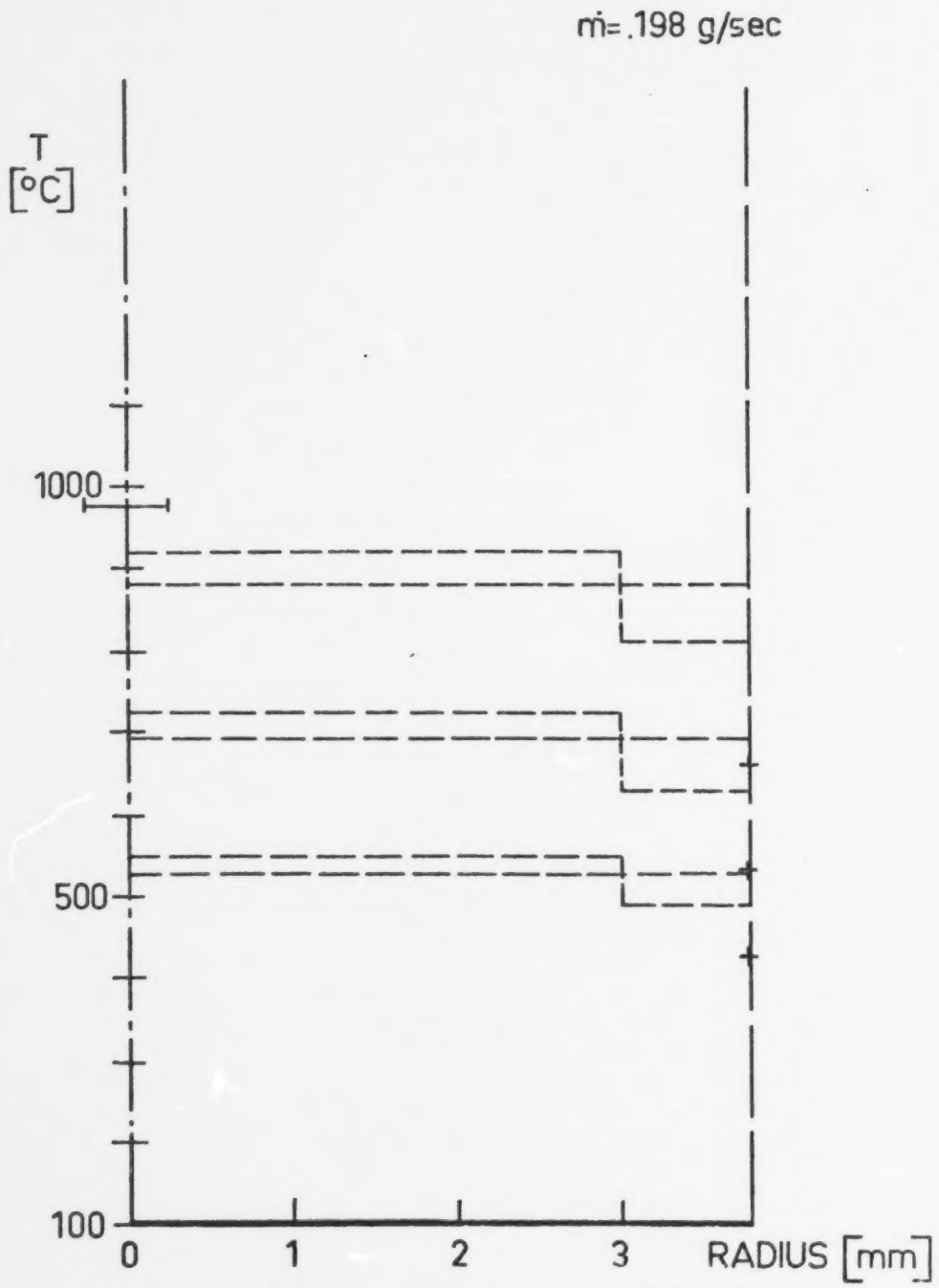

FIG. 49 POROUS CARBON SAMPLE: TEMPERATURE DISTRIBUTION

the porous sample average temperature is determined directly by thermocouples located immediately downstream from the porous surface.

Each temperature distribution of Fig. 47, 48, and 49 corresponds to a particular value of the argon transpiring mass flow rate and to a particular value of the current and a certain value of the total pressure drop through the sample is associated with each curve. A geometrical average temperature, indicated in Fig. 47, 48, and 49 by the dashed lines, is determined from each temperature distribution.

If the total pressure drop is plotted versus the average sample temperature, for the three values of the argon cooling mass flow rate, the curves of Fig. 50 are obtained where the triangular symbols represent experimental points derived from Fig. 47, 48, and 49. The meaning of the other symbols will be explained later.

A crossplot of Fig. 50 yields the curves of Fig. 51 in which the pressure drop is plotted versus the argon cooling mass flow rate per unit area for different temperature values.

A.III.D. Conclusions

From these curves, the values of the parameters A* and B* can be derived. If the pressure gradient is assumed to be constant across the sample thickness and if argon is considered as an ideal gas, Eq. (A.7) gives:

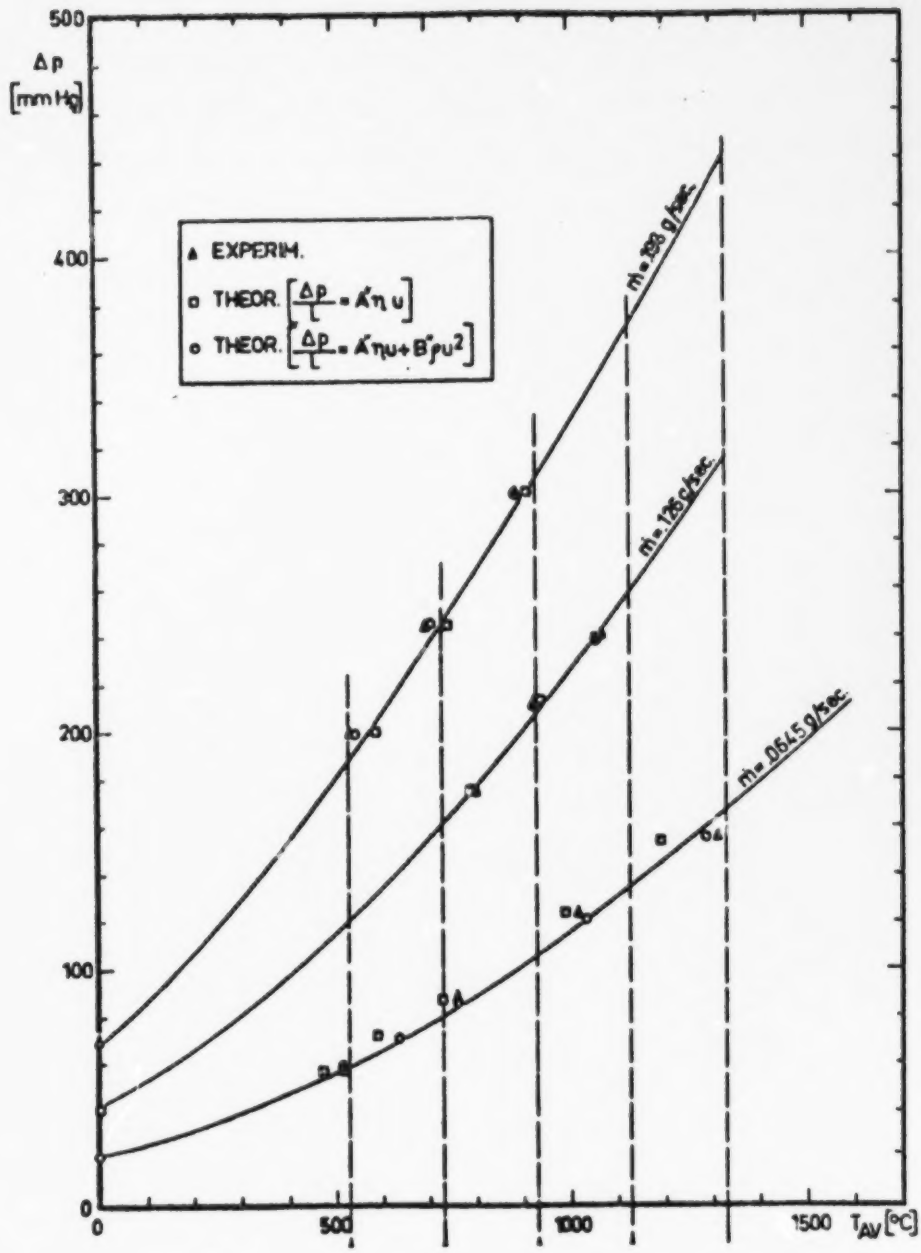

FIG. 50 PRESSURE DROP AS A FUNCTION OF AVERAGE TEMPERATURE THROUGH POROUS CARBON SAMPLE

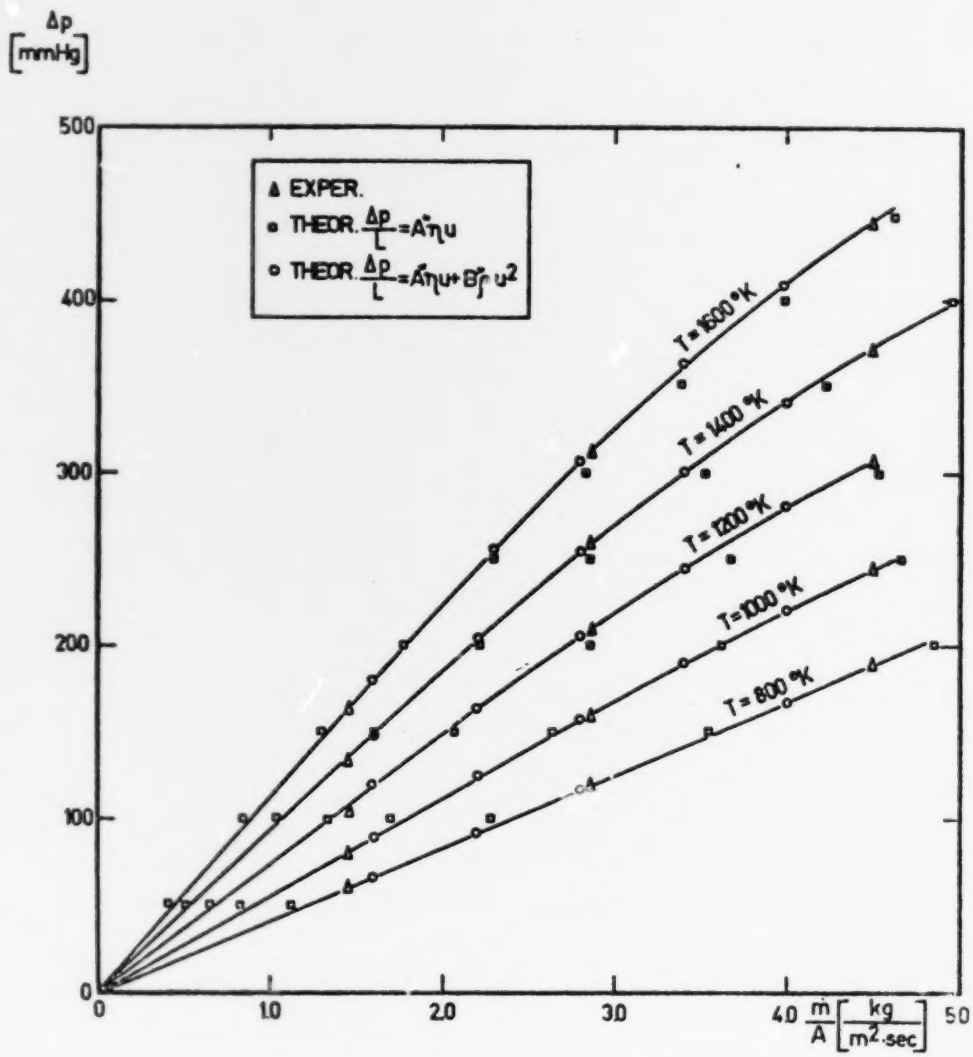

FIG. 51 POROUS CARBON HIGH TEMPERATURE FLOW CHARACTERISTICS

$$\frac{\Delta p}{l} = A^* \eta \left(\frac{\dot{m}}{A}\right) \frac{R^* T}{\bar{p}} + B^* \left(\frac{\dot{m}}{A}\right)^2 \frac{R^* T}{\bar{p}} \qquad (A.11)$$

where $\bar{p}$ is the average pressure across the sample.

By fitting the corresponding values of Δp and $\frac{\dot{m}}{A}$ from Fig. 51 into Eq. (A.11) using a least square numerical method, the values of A* and B* can be determined: The results are reported in Fig. 52. They show that the value of A* remains nearly constant with increasing temperature, whereas B* decreases sharply with temperature and becomes negligibly small for $T \gtrsim 1000$ °K. This fact can be explained in terms of the argon viscosity which increases with increasing temperature while its density decreases; and, therefore, for constant velocity, the Reynolds number decreases. For the examined sample, the room temperature value of the Reynolds number based on the average pore diameter is one order of magnitude larger than at T = 1400 °K for the argon mass flow rates used in the present experiment.

From the above consideration, we can conclude that the flow regime changes with increasing temperature from a regime governed by inertia forces at room temperature to a Darcy regime at $T \geq 1000$ °K. This result suggests to correlate the high temperature data of Fig. 53 with a linear equation of the type

$$\frac{\Delta p}{l} = A^* \eta u \qquad (A.12)$$

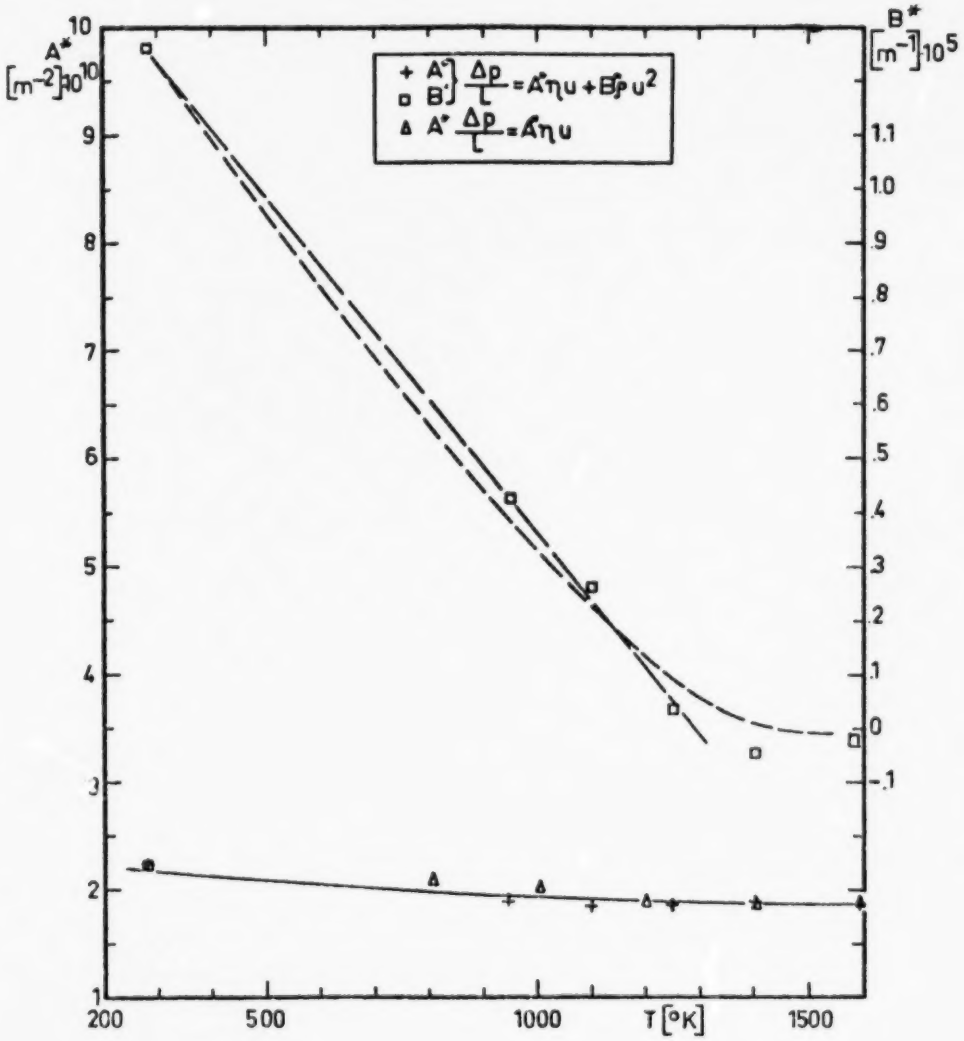

FIG. 52 POROUS CARBON FLOW PARAMETERS AS A FUNCTION OF TEMPERATURE

apt to describe the flow in Darcy's regime.

The values of A* determined in this way are indicated in Fig. 52 by the triangular symbols.

Using the A* and B* values of Fig. 52, the pressure drop has been calculated as a function of temperature and argon mass flow rate per unit area and the results are shown in Fig. 50 and 51. A good agreement exists with the experimental data in both cases whether the first order or second order equation for Δp is used. Obviously, for $T \lesssim \div$ 1000 °K, only the quadratic expression for Δp can be used.

A cross check for the validity of the above results for A* and B* has then been performed, based on the data of Fig. 47, 48, and 49.

From Eq. (A.11), one can derive:

$$u = \frac{- A^* \eta(T) \pm \sqrt{A^{*2} \eta^2(T) + 4 \frac{\Delta p}{l} B^*(T) \rho\ (p, T)}}{2\ B^*(T) \rho\ (p, T)} \qquad (A.13)$$

or, for Darcy's regime,

$$u = \frac{\Delta p}{l A \eta(T)} \qquad (A.14)$$

Since

$$\dot{m} = \iint_A \rho\ (p, T)\ u\ (p, T)\ dA \qquad (A.15)$$

it is possible to calculate the mass flow rate passing through a certain test area once the pressure drop across

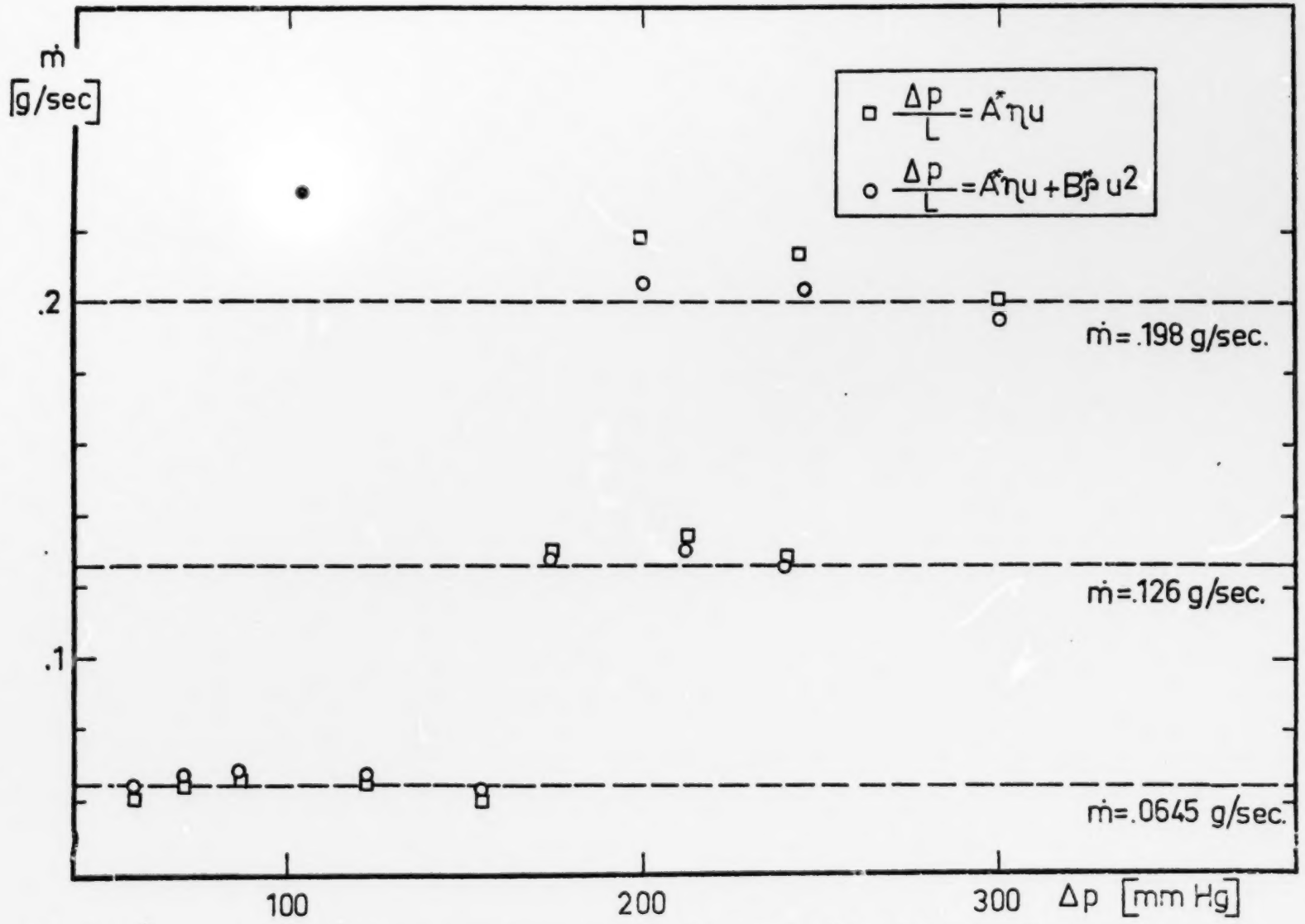

FIG. 53 COMPARISON OF THEORETICAL AND EXPERIMENTAL VALUES OF MASS FLOWRATE THROUGH POROUS CARBON SAMPLE

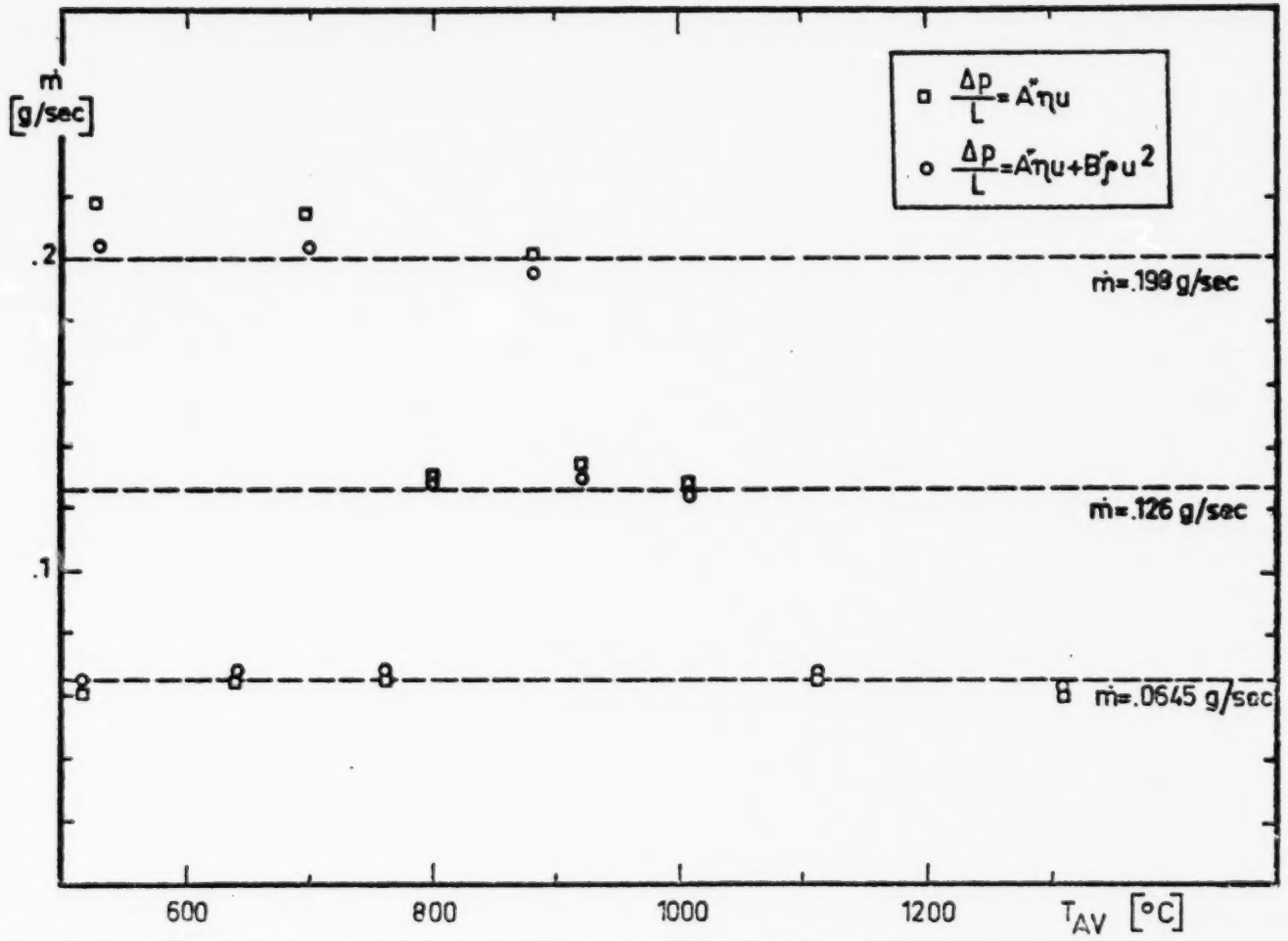

FIG. 54 COMPARISON OF THEORETICAL AND EXPERIMENTAL VALUES OF MASS FLOWRATE THROUGH POROUS CARBON SAMPLE

REFERENCES

[1] Glaubermann, H., Breslin, A. J., "The Generation of a Solid Sub-micron Test Aerosol", Am. Ind. Hyg. Assoc. Quart., Vol. 17, No. 1 (1956).

[2] Chace, W. G., Moore, H. K., Exploding Wires, Vol. 1, Plenum Press, New York (1959).

[3] Chace, W. G., Moore, H. K., Exploding Wires, Vol. 2, Plenum Press, New York (1962).

[4] Chace, W. G., Moore, H. K., Exploding Wires, Vol. 3, Plenum Press, New York (1964).

[5] Bennett, F. D., "Exploding Wires", Scientific American, Vol. 206, No. 5 (1962).

[6] Freundlich, H., Basu, S. K., "Uber den Einfluss des Rührens auf die Koagulation hydrophober Sole", Zeitschrift für Physikalische Chemie, Vol. 115 (1925).

[7] Heller, W., "Sur la coagulation des sols hydrophobes par congelation en relation avec la coagulation mechanique", Compt. Rend., Vol. 199 (1934).

[8] Karioris, F. G., Fish, B. R., "An Exploding Wire Aerosol Generator", J. Coll. Sci., Vol. 17, No. 2 (1962).

[9] Tomaides, M., "Characterization of Chain Agglomerated Aerosols", Section 3: "An Improved Exploding Wire Aerosol Generator", P.L.P. No. 130, Mech. Eng. Dept., U. of Minnesota (1968).

[10] Chace, W. G., "A Bibliography of Electrically Exploded Wire Phenomenon", AFCRC-TN-58-457 (1958).

[11] Karioris, F. G., Fish, B. R., "Uranium Oxide Smoke from Exploding Wire", Health Physics, Vol. 4, No. 2 (1960).

[12] Reichelt, H., On Aerosol Generated in Electric Arcs Between Metal Electrodes, Ph.D. Thesis, First Physics Institut, Wien (1968).

[13] Howden, D. G., "Mass Transfer of Metal Vapor and Anode Temperatures in Arc Melting", Welding Journal, No. 3 (1969).

[14] Pfender, E., Boffa, C., "Aerosol Generation with a Transpiration-Cooled Anode in a High Intensity Arc", University of Minnesota, HTLTR No. 90 (1969).

[15] Pfender, E., Boffa, C., "Generation of Ultrafine Aerosols with a Transpiration Cooled Anode in a High Intensity Arc", Rev. Sci. Instruments, Vol. 41, No. 5 (1970).

[16] Boffa, C., Pfender, E., "A New Method for the Generation of Ultrafine, Monodisperse Aerosols", University of Minnesota, HTLTR No. 98 (1971).

[17] Cremers, C. J., The Spectrometric Measurement of the Temperature Field in an Arc with a Transpiration Cooled Anode, ARL 65-117 (1965).

[18] Pfender, E., Wutzke, S. A., Eckert, E.R.G., "An Arc Tunnel Facility for Thermal Analysis of Anode and Cathode Regimes in an Electric Arc Column", NASA CR 54080 (1964).

[19] Pfender, E., Wutzke, S. A., Shih, K. T., Eddy, T., Eckert, E.R.G., "Thermal Analysis and Study of Arc Flow Interactions in the Anode Regime of an Electric Arc", NASA CR 54465 (1965).

[20] Pfender, E., Eckert, E.R.G., "Behavior of an Electric Arc with Superimposed Axial Flow", Proc. Heat Transfer and Fluid Mech. Inst., Berkeley, California (1965).

[21] Eckert, E.R.G., Pfender, E., Advances in Plasma Heat Transfer, Advances in Heat Transfer, Vol. 4, Academic Press, New York, New York (1967).

[22] Wutzke, S. A., Pfender, E., Eckert, E.R.G., "Symptomatic Behavior of an Electric Arc with a Superimposed Flow", AIAA Journal, Vol. 6, No. 8 (1968).

[23] Shih, K. T., Pfender, E., "Electrode Energy Transfer Mechanisms in an MPD Arc", AIAA Journal, Vol. 8, No. 2 (1970).

[24] Whitby, K. T., Clark, W. E., "Electric Aerosol Particle Counting and Size Distribution Measuring System for the 0.015 to 1 μ Size Range", Tellus, Vol. XVIII, No. 2 (1966).

[25] Liu, B.Y.H., Yeh, H. C., "On the Theory of Charging of Aerosol Particles in an Electric Field", J. Appl. Phys., Vol. 39, No. 3 (1968).

[26] Liu, B.Y.H., Whitby, K. T., "Experimental Study of Particle Charging at Low Pressures", Proceedings of the AEC Conference on Radioactive Fallout from Nuclear Weapons Tests, Germantown, Maryland (1964).

[27] Whitby, K. T., "Generator for Producing High Concentration of Small Ions", Rev. Sci. Instr., Vol. 32 (1961).

[28] Whitby, K. T., Liu, B.Y.H., Peterson, C. M., "Charging and Decay of Monodisperse Aerosols in the Presence of Unipolar Ion Sources", J. Coll. Sci., Vol. 29 (1965).

[29] Whitby, K. T., Clark, W. E., Generation and Decay of Small Ions, Part II, U. of Minnesota P.L.P. No. 95 (1966).

[30] Husar, B. H., Whitby, K. T., Aerosol Measurements in Los Angeles Smog, Section III, Part 5, U. of Minnesota P.L.P. No. 141 (1970).

[31] De Wiest, R.J.M., Flow Through Porous Materials, Academic Press, New York, New York (1969).

[32] Bond, R. L., Porous Carbon Solids, Academic Press, New York, New York (1967).

[33] Collins, R. E., Flow of Fluids Through Porous Matrices, Reinhold P. C., New York, New York (1961).

[34] Muskat, M., The Flow of Homogeneous Fluid Through Porous Media, Edwards, Ann Arbor, Michigan (1946).

[35] Scheidegger, A. E., The Physics of Flow Through Porous Media, Rev. Ed., Macmillan, New York, New York (1960).

[36] Carman, P. C., Flow of Gases Through Porous Media, B.S.P., London (1956).

[37] Martin, J. J., McCabe, W. L., and Monrad, C. C., "Pressure Drop Through Stacked Spheres: Effect of Orientation", Chem. Eng. Progress, Vol. 47, No. 2 (1954).

[38] Brownell, L. E., Dombrowski, H. S., and Dickey, C. A., "Pressure Drop Through Porous Media, Part IV: New Data and Revised Correlation", Chem. Eng. Progress, Vol. 46, No. 8 (1950).

[39] Stepochkin, B. F., "A Two Term Equation for the Resistance of Porous Media", Int. Chem. Eng., Vol. 3, No. 1 (1963).

[40] Ward, J. C., Asce, A. M., "Turbulent Flow in Porous Media", Journal of the Hydraulics Divisions, Proceedings of ASCE, Hy. 5 (1964).

[41] Brinkley, S. R., Jr., "Heat Transfer Between a Fluid and a Porous Solid Generating Heat", J. of Appl. Phys., Vol. 18, No. 6 (1947).

[42] Yang, J. W., "Analysis of Heat Transfer in Evaporative-Transpiration-Cooled Systems", J. Spacecraft, Vol. 6, No. 6 (1969).

[43] Saunders, O. A., Ford, H., "Heat Transfer in the Flow of Gas Through a Bed of Solid Particles", J. of Iron and Steel Inst., Vol. CXLI, No. 1 (1940).

[44] Hewitt, G. F., Sharratt, E. W., "Gaseous Diffusion in Porous Media with Particular Reference to Graphite", Nature, Vol. 198, No. 4884 (1963).

[45] Rosner, D. E., "Transpiration Cooling with Chemical Reactions", Pyrodynamics, Vol. 2, No. 4 (1965).

[46] Schneider, P. J., Brogan, J. J., "Temperature Response of a Transpiration-Cooled Plate", ARS J., Vol. 32, No. 2 (1962).

[47] Mendelsohn, A. R., "Transient Temperature of a Porous-Cooled Wall", AIAA J., Vol. 1, No. 6 (1963).

[48] Green, D. W., Perry, R. H., "Heat Transfer with a Flowing Fluid Through Porous Media", Chem. Eng. Progress Symposium Series, Vol. 57, No. 32 (1961).

[49] Grootenhuis, P., "The Mechanism and Application of Effusion Cooling", The Journal of the Royal Aeronautical Society, Vol. 63, No. 578 (1959).

[50] Green, L., Jr., "Gas Cooling of a Porous Heat Source", J. Appl. Mech., Vol. 74, No. 6 (1952).

[51] Hung, F. T., Nevins, R. G., "Unsteady-State Heat Transfer with a Flowing Fluid Through Porous Solids", ASME Paper 65-HT-10 (1965).

[52] Weinbaum, S., Wheeler, H. L., "Heat Transfer in Sweat-Cooled Porous Metals", J. Appl. Phys., Vol. 20, No. 1 (1949).

[53] Detkov, S. P., "Calculation of a Model of a Porous Body at High Temperatures", Z. Prike. Mekh. i Tekh. Fiz., No. 1 (1968).

[54] Voronin, V. J., Glushakov, A. N., "Temperature Drop Over the Cross Section of a Wall in the Case of Transpiration Cooling", Aviat. Tekh., Vol. 11, No. 4 (1968).

[55] Dul'nev. G. N., "Heat Transfer Through Solid Dispersed Systems", Inzh.-Fiz-Z., Vol. 9, No. 9 (1965).

[56] Kukota, I. P., Prshedromirskaia, E. M., Sleptsov, V. M., "Gas Permeability of Porous Materials from Refractory Compounds", Por. Metall., Vol. 5, No. 11 (1965).

[57] Koh, J.C.Y., del Casal, E. P., "Heat and Mass Transfer with Chemical Reactions for Fluid Flow Through a Porous Matrix in Re-entry Thermal Protection", AIAA Paper No. 66-423 (1966).

[58] Koh, J.C.Y., del Casal, E. P., "Temperature and Pressure Distribution for Fluid Flow Through Porous Walls of Cylindrical and Spherical Bodies and Sectors", AIAA Paper No. 66-433 (1966).

[59] Munser, H., "Problems of Simultaneous Mass and Heat Transport Through Porous Bodies", Wissenschaftliche Zeitschrift, Vol. 13, No. 4 (1964).

[60] Koh, J.C.Y., del Casal, E. P., "Heat and Mass Flow Through Porous Matrices for Transpiration Cooling", Proceedings of the 1965 Heat Transfer and Fluid Mechanics Institute, Stanford University Press (1965).

[61] Greenberg, D. B., Weger, E., "An Investigation of the Viscous and Inertial Coefficients for the Flow of Gases Through Porous Sintered Metals with High Pressure Gradients", Chem. Eng. Sci., Vol. 12, No. 1 (1960).

[62] Druzhinin, S. A., Leont'yev, A. I., "Contribution to the Calculation of Temperature Distribution on a Porous Plate", Inzh.-Fizich. Zhur., Vol. X, No. 4 (1966).

[63] Druzhinin, S. A., "On the Calculation of Internal Heat Exchange During Porous Cooling", DDC Paper AD 619-570, Translation from Teploenergetika, No. 9 (1961).

[64] Eckert, E.R.G., Schoeck, P. A., Winter, E.R.F., "Thermische Untersuchung eines Elektrischen Hochstromlichtbogens mit Poröser, Gasgekühlter Anode", Int. J. Heat Mass Transfer, Vol. 5, No. 2 (1962).

[65] Druxes, H., Schmitz, G., Patt, H. J., "Der Einfluss einer Radialen Masseneinströmung auf Elektriche Lichtbögen", Zeitschrift fur Physik, Vol. 203, No. 2 (1967).

[66] Marshall, E., Gauger, V., "Berechung des Temperaturverlaufes in einer Transpirationsgekühlten Rohrwand", Wärme- und Stoffübertragung, Vol. 2 (1968).

[67] Anderson, J. E., Transpiration Cooling of a Constricted Electric-Arc Heater, ARL 66-0517 (1966).

[68] Anderson, J. E., Eckert, E.R.G., "Transpiration Cooling of a Constricted Electric Arc Heater", AIAA J., Vol. 5, No. 4 (1967).

[69] Gruber, G. G., Pfender, E., Eckert, E.R.G., Experimental Study of a Transpiration-Cooled Constricted Arc, University of Minnesota HTLTR No. 72, ARL 68-0023 (1968).

[70] Cremers, C. J., Mahan, J. R., "Prediction of the Onset of Burnout in an Electric Arc with a Transpiration-Cooled Anode", AIAA Paper No. 69-696 (1969).

[71] Cremers, C. J., Eckert, E.R.G., "Temperature Field in an Arc with a Transpiration Cooled Anode", AIAA J., Vol. 3, No. 10 (1965).

[72] Cremers, C. J., Birkebak, R. C., "The Prediction of the Mode Transition in an Arc with a Transpiration-Cooled Anode", AIAA J., Vol. 9, No. 1 (1966).

[73] Schneider, P. J., Mauer, R. E., Strapp, M. G., "Two Dimensional Transpiration Cooling", AIAA Paper No. 69-96, AIAA 7th Aerospace Sciences Meeting, New York, New York (1969).

[74] Pfender, E., Gruber, G., Eckert, E.R.G., "Experimental Investigation of a Transpiration-Cooled Constricted Arc", High Temperature Technology, Proceedings of the Third International Symposium, Asilomar, California (1967).

[75] Pfender, E., Gruber, G., Eckert, E.R.G., "Experimental Investigation of a Transpiration-Cooled Constricted Arc", Proceedings of the Eighth International Conference on Phenomena in Ionized Gases, Vienna (1967).

[76] Pfender, E., Raithby, G. D., Eckert, E.R.G., "An Anode Comparison Study in a Wall Stabilized Argon Arc", ARL 65-239 (1965).

[77] Pfender, E., Eckert, E.R.G., Raithby, G. D., "Energy Transfer Studies in a Wall Stabilized, Cascaded Arc", Proceedings of the Seventh International Conference on Phenomena in Ionized Gases, Vol. I, Beograd (1966).

[78] Heberlein, J., Pfender, E., "Transpiration Cooling of the Constrictor Walls of an Electric High Intensity Arc", ASME Paper 70-HT-35 (1970).

[79] Pfender, E., Heberlein, J., Characteristics of a High Pressure Arc Confined in a Transpiration-Cooled Tube, ARL 70-0135 (1970).

[80] Heberlein, J., Pfender, E., Eckert, E.R.G., Study of a Transpiration-Cooled, Constricted Electric Arc, ARL 70-0007 (1970).

[81] Tannen, P. D., Experimental Study of a Transpiration-Cooled, Wall Stabilized DC Arc, Air Force Institute of Technology, Wright-Patterson Air Force Base, Ohio, GA/ME/62-6 (1962).

[82] Baran, M. F., An Experimental and Theoretical Study of the Wall-Stabilized, Transpiration Cooled DC Electric Arc, Air Force Institute of Technology, Wright-Patterson Air Force Base, Ohio, Phys/63-2 (1963).

[83] Jones, R. N., An Investigation of the Wall-Stabilized Transpiration-Cooled DC Electric Arc, Air Force Institute of Technology, Wright-Patterson Air Force Base, Ohio, GAW/Mech 64-11 (1964).

[84] Willgohs, R. H., The Temperature Distribution in the Porous Constrictor Wall of a Transpiration-Cooled Electric Arc, M. S. Thesis, University of Minnesota (1968).

[85] Schoeck, P. A., Eckert, E.R.G., Wutzke, S. A., An Investigation of the Anode Losses in Argon Arcs and their Reduction by Transpiration Cooling, ARL 62-341 (1962).

[86] Watson, V. R., "Comparison of Detailed Numerical Solutions with Simplified Theories for the Characteristics of the Constricted-Arc Plasma Generator", Proceedings of the 1965 Heat Transfer and Fluid Mechanics Institute, University of California, Los Angeles, California (1965).

[87] Darcy, H. P., Les Fontaines Publiques de la Ville de Dijon, V. Dalmont, Paris (1896).

[88] Boffa, C., Pfender, E., "Enthalpy Probe and Spectrometric Studies in an Argon Plasma Jet", University of Minnesota, HTLTR No. 70 (1967).